

**ACOUSTIC EMISSION SIGNAL CHARACTERIZATION AND
INFRARED THERMOGRAPHY STUDIES DURING
DRILLING OF METAL MATRIX COMPOSITES**

By

K. THIRUKKUMARAN

(Enrollment No: PHYS02201504015)

Indira Gandhi Centre for Atomic Research, Kalpakkam

*A thesis submitted to the
Board of Studies in Physical Sciences*

*In partial fulfillment of requirements
for the Degree of*

DOCTOR OF PHILOSOPHY

of

HOMI BHABHA NATIONAL INSTITUTE



JUNE, 2020

Homi Bhabha National Institute

Recommendations of the Viva Voce Committee

As members of the Viva Voce Committee, we certify that we have read the dissertation prepared by K. Thirukkumaran entitled "Acoustic emission signal characterization and infrared thermography studies during drilling of metal matrix composites" and recommend that it may be accepted as fulfilling the thesis requirement for the award of Degree of Doctor of Philosophy.

For. [Signature] Dean, PS Date: 26/04/2021
Chairman - Dr. K. Velusamy

[Signature] Date: 26/04/2021
Guide/Convenor - Dr. C. K. Mukhopadhyay

[Signature] Date: 28-04-2021
External Examiner- Dr. Andre DL Bataineh

N.V. Chandra Shekar Date: 26/4/2021
Member 1 - Dr. N. V. Chandra Shekar

For. [Signature] Dean PS Date: 26-04-2021
Member 2 - Dr. S. Murugan

[Signature]
Member 3 - Dr. Arup Dasgupta

Final approval and acceptance of this thesis is contingent upon the candidate's submission of the final copies of the thesis to HBNI.

I/We hereby certify that I/we have read this thesis prepared under my/our direction and recommend that it may be accepted as fulfilling the thesis requirement.

Date: 26/04/2021

Place: Kalpakkam

[Signature]
Dr. C. K. Mukhopadhyay
(Guide)

Homi Bhabha National Institute

Recommendations of the Viva Voce Committee

As members of the Viva Voce Committee, we certify that we have read the dissertation prepared by K. Thirukkumaran entitled "Acoustic emission signal characterization and infrared thermography studies during drilling of metal matrix composites" and recommend that it may be accepted as fulfilling the thesis requirement for the award of Degree of Doctor of Philosophy.

For. [Signature] Dean, PS Date: 26/04/2021
Chairman - Dr. K. Velusamy

[Signature] Date: 26/04/2021
Guide/Convenor - Dr. C. K. Mukhopadhyay

[Signature] Date: 28-04-2021
External Examiner- Dr. Andre DL Batalha

N.V. Chandra Shekar Date: 26/4/2021
Member 1 - Dr. N. V. Chandra Shekar

For. [Signature] Dean PS Date:
Member 2 - Dr. S. Murugan

[Signature] Date: 26-04-2021
Member 3 - Dr. Arup Dasgupta

Final approval and acceptance of this thesis is contingent upon the candidate's submission of the final copies of the thesis to HBNI.

I/We hereby certify that I/we have read this thesis prepared under my/our direction and recommend that it may be accepted as fulfilling the thesis requirement.

Date: 26/04/2021

Place: Kalpakkam

[Signature]
Dr. C. K. Mukhopadhyay
(Guide)

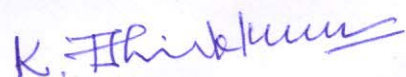
STATEMENT BY AUTHOR

This dissertation has been submitted in partial fulfillment of requirements for an advanced degree at Homi Bhabha National Institute (HBNI) and is deposited in the Library to be made available to borrowers under rules of the HBNI.

Brief quotations from this dissertation are allowable without special permission, provided that accurate acknowledgement of source is made. Requests for permission for extended quotation from or reproduction of this manuscript in whole or in part may be granted by the Competent Authority of HBNI when in his or her judgment the proposed use of the material is in the interests of scholarship. In all other instances, however, permission must be obtained from the author.

Date: 26.04.2021

Place: Kalpakkam



(K. THIRUKKUMARAN)

DECLARATION

I, hereby declare that the investigation presented in the thesis has been carried out by me. The work is original and has not been submitted earlier as a whole or in part for a degree/diploma at this or any other Institution/University.

Date: 26.04.2021

Place: Kalpakkam

K. Thirukkumar

(K. THIRUKKUMARAN)

LIST OF PUBLICATIONS ARISING FROM THE THESIS

JOURNALS

1. **K. Thirukkumaran**, C.K. Mukhopadhyay, T. K. Haneef and S. Bagavathiyappan
“Acoustic emission and infrared thermography studies during drilling of Al-5%SiC-5%B₄C hybrid metal matrix composite”. **Insight-Non-Destructive Testing and Condition monitoring**, Vol. 61, No.5, pp. 249–256, 2019.
2. **K. Thirukkumaran**, M. Menaka, C. K. Mukhopadhyay and B. Venkataraman, “A study on temperature rise, tool wear and surface roughness during drilling of Al-5%SiC composite”. **Arabian Journal of Science and Engineering**, Vol. 45, pp. 5407–5419, 2020.
3. **K. Thirukkumaran** and C. K. Mukhopadhyay, “Analysis of acoustic emission signal to characterization the damage mechanism during drilling of Al-5%SiC metal matrix composite”, **Silicon**, Vol. 13, pp.309–325, 2021.
4. **K. Thirukkumaran** and C. K. Mukhopadhyay, “Acoustic emission signal processing for tool wear analysis during drilling of Al-5%B₄C composite” (Under Review-Ultrasonics)
5. **K.Thirukkumaran**, M. Menaka, C. K. Mukhopadhyay and B. Venkataraman “Investigation of tool and workpiece temperature during drilling of Al-5%B₄C composite: experimental and simulation studies” (Under preparation)
6. **K. Thirukkumaran** and C.K. Mukhopadhyay, “Wavelet analysis for the characterization of damage mechanisms duringdrilling of Al-5%SiC-5%B₄C hybrid metal matrix composite” (Under preparation)

NATIONAL/INTERNATIONAL CONFERENCES

1. **K. Thirukkumaran**, T. K. Haneef, C.K. Mukhopadhyay and B.P.C Rao, "Vibrational and acoustic emission techniques for tool wear monitoring in metal matrix composites", International Conference on Condition Monitoring (ICCM-2016), 26-27 October 2016, GITAM university, Visakhapatnam, Andhra Pradesh.
2. **K. Thirukkumaran**, T. K. Haneef, C.K. Mukhopadhyay, "Acoustic emission technique for tool wear monitoring in metal matrix composite during drilling" National Conference on Condition Monitoring (NCCM-2017), 26-27 October 2017, jointly conducted by Condition Monitoring Society of India (CMSI) and IGCAR, Kalpakkam.
3. **K. Thirukkumaran** and C. K. Mukhopadhyay, "Study of cutting tool damage during drilling of Al-5%SiC metal matrix composite using acoustic emission technique", International conference on structural Integrity (ICONS-2018), 14-17 December 2018, jointly conducted by IGCAR and IIT Madras, Chennai. **(Best Paper award)**
4. **K. Thirukkumaran** and C. K. Mukhopadhyay, "Acoustic emission signal analysis to characterize the damage mechanism during drilling of metal matrix composite", Non destructive Evaluation for Roburst Indian Nuclear Programme (NDERNP-2020), 28-29 January 2020, IGCAR, Kalpakkam. **(Best Poster award)**

Date: 26.04.2021

Place: Kalpakkam

K. Thirukkumaran

(K. THIRUKKUMARAN)

Solely dedicated to my father

K. Kamalesan

ACKNOWLEDGEMENTS

I was able to complete this dissertation with the support of several people. First and foremost, I wish to thank my research supervisor, **Dr. C. K. Mukhopadhyay**, Professor, HBNI, and former Head NDED, IGCAR for his consistent guidance, suggestions and valuable comments. His effective planning and intellectual ideas helped me in my research work and writing this thesis. I am thankful to my doctoral committee members **Dr. K. Velusamy** (Chairman), **Dr. N. V. Chandra Shekar** (Member), **Dr. S. Murugan** (Member), and **Dr. Arup Dasgupta** (Member) for their regular evaluation of the research work and suggestions to improve the quality of this work. I thank all the Professors of HBNI who taught me various subjects during my course work.

I express my sincere gratitude to **Dr. A. K. Bhaduri**, Director, IGCAR and **Dr. Shaju K. Albert**, Director, MMG and MSG, IGCAR for inspiration and encouragement. I would like to express my gratitude to **Dr. B. Venkatraman**, Director, RSD and RMG, IGCAR for providing the instruments to carry out the experimental works. Furthermore, I sincerely thank the **Department of Atomic Energy (DAE)**, India, for providing the necessary financial support.

I would like to thank **Dr. Vidya Sundararajan** (Dean, Student Affairs) and authorities of GSO, Kalpakkam for providing a pleasant accommodation in the enclave. I would like express my sincere thanks to **Dr. Rajaraman** (Dean, Physical Sciences), HBNI for supporting academic procedure. I am thankful to **Dr. R. Divakar**, Associate Director, MEG, MMG and **Dr. Anish Kumar**, Head NDED, MMG for their support.

My heartfelt thanks to **Mr. T. K. Haneef**, NDED, IGCAR, **Mrs. M. Menaka**, **Mr. S. Bhagavathiyappan**, **Dr. G. K. Sharma**, **Dr. B. Sasi** and **Dr. W. Sharathchandra Singh** for their help and constant support to carry out the research work.

I am grateful to **Dr. S. Thirunavukkarasu, Dr. S. Mahadevan**, NDED, IGCAR, for their support. I would like thank to **Shri. B.S. Ramesh Babu**, Head MS section, central workshop division (CWD) for providing machining facility. I deeply appreciate the works of **Mr. R. Saxena**, RIRD and **Mr. Natarajan, Mr. P. Shanmugam, Mr. T. Saravanan, Mr. M. Dhamodaran, Mr. D. Dileep, C. Muthusamy** and **Mr. V. Rajendran**, CWD for helping to carry out the drilling tests.

I thank my lab colleagues **Ms. S. Lavanya, Ms. T. Vijayachadrika** and **Dr. Chandan kumar Bhagat, Dr. K. Prajna**, and **Mr. Arjun** and other NDED members and Research scholars for their suggestions and moral support.

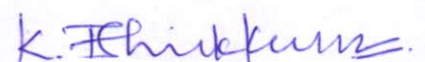
I would like to acknowledge my batch mate friends, **Mrs. Sumana, Mr. Pavan, Ms. Madhura, Mrs. Suma, Mr. Bijay kumar Das** and all the senior and junior friends for making my academic ambience comfortable and pleasant. Also, I thank **Mr. Suman Saurav** for helping COMSOL model and **Mr. Sarvajith** for help and support.

This dissertation would have never been possible without the love and patience of my family members: mother **Mrs. K. Rani**, father **Mr. K. Kamalesan**, brothers **Mr. K. Bhoopal**, and **Mr. K. Arumugam** and children's **B. Navenesh, B. Shelley** and **A. Rohit** who have supported me despite their unwillingness of my separation from them. My love and gratitude for them can hardly be expressed in words.

Finally, I would like to thank and share this achievement with my beloved wife **Mrs. T. Bruntha** and my lovable baby **T. Dhanushree**, who has always been with me creating a cheerful world filled with love, affection, and support.

Date: 26.04.2021

Place: Kalpakkam



(K. THIRUKKUMARAN)

TABLE OF CONTENTS

ABSTRACT	v
LIST OF FIGURES	vii
LIST OF TABLES	xiv
LIST OF ABBREVIATIONS	xv
NOMENCLATURE	xvii
CHAPTER-1	1
INTRODUCTION	1
1.1 Non-destructive evaluation techniques	1
1.2 Condition monitoring	2
1.2.1 Tool wear/damage	4
1.2.2 Tool condition monitoring (TCM) techniques	6
1.3 Direct methods for tool condition monitoring	8
1.3.1 Optical measurement	8
1.3.2 Wear particle and radioactivity analysis	9
1.3.3 Workpiece size changing	10
1.4 Indirect methods for tool wear condition monitoring	11
1.4.1 Cutting force measurement	11
1.4.2 Vibration analysis	11
1.5 Acoustic emission (AE) and infrared thermography (IRT) for tool wear monitoring	12
1.5.1 Acoustic emission testing (AET)	12
1.5.2 Acoustic emission source mechanism	14
1.5.3 AE signal and its parameters	16
1.5.4 Advantages and limitations of AET	19
1.5.5 Applications of AET	19
1.5.6 AE signal processing methods	20
1.6 Infrared thermography technique	21
1.6.1 Infrared thermal imaging	21
1.6.2 Infrared thermography system	22
1.6.3 Theory of IR imaging	23
1.6.4 Advantages and limitations of IRT	25
1.6.5 Applications of IRT	25

1.7 Application of AET and IRT for tool wear and workpiece damage monitoring	26
1.7.1 Acoustic emission	26
1.7.2 Infrared Thermography	28
1.8 Motivation for the study	31
1.9 Objective and scope of the work	31
1.10 Outline of the dissertation	32
CHAPTER– 2	35
MATERIALS AND EXPERIMENTAL TECHNIQUES	35
2.1 Fabrication of metal matrix composites	35
2.1.1 Stir casting method	35
2.2 Chemical analysis	37
2.3 Hardness measurement	37
2.4 Drilling experimental setup	38
2.5 Acoustic emission testing instrumental setup	39
2.5.1 Sensors	40
2.5.2 Amplification and filter	42
2.5.3 Signal processing approaches	43
2.5.4 Frequency domain analysis	43
2.5.5 Time-frequency domain analysis	44
2.5.6 Wavelet packet analysis	44
2.5.7 Selection of mother wavelet and levels	47
2.6 Infrared thermography experimental setup	47
2.6.1 Emissivity calculation	48
2.6.2 Detector	49
2.6.3 Cooling systems	50
2.7 Tool and workpiece damage analysis	51
2.7.1 Vision measuring microscope	51
2.7.2 Surface profilometer	52
2.7.3 Scanning electron microscope	53
2.8 Summary	54
CHAPTER– 3	55
ACOUSTIC EMISSION AND INFRARED THERMOGRAPHY STUDIES IN Al-5%SiC COMPOSITE	55

3.1 Experimental details	55
3.2 Acoustic emission signal analysis and discrimination of damage mechanisms	57
3.2.1 AE Time domain analysis	57
3.2.2 AE Frequency domain analysis	59
3.2.3 Continuous wavelet transform	61
3.2.4 Wavelet packet analysis	65
3.2.5 Tool wear detection and correlation with AE features	70
3.3 Temperature rise during drilling of Al-5%SiC composite	74
3.3.1 Tool and workpiece temperatures	76
3.3.2 Undeformed chip thickness calculation	78
3.3.3 Numerical simulation of workpiece temperature	79
3.3.4 Tool wear detection and corresponding tool temperature	81
3.4 Analysis of variance (ANOVA) for identification of significant cutting parameters	85
3.5 Surface quality characterization	86
3.6 Chip formation mechanism	88
3.7 Effect of cutting parameters on AE and IRT	90
3.7.1 Variation of AE time domain parameters with cutting conditions	90
3.7.2 Variation of tool temperature with cutting conditions	92
3.7.3 Correlation of AE_{RMS} and average tool temperature with tool wear	92
3.8 Summary	93
CHAPTER-4	95
ACOUSTIC EMISSION SIGNAL ANALYSIS AND INFRARED THERMOGRAPHY TECHNIQUE FOR THE DRILLING OF Al-5%B₄C COMPOSITE	95
4.1 Experimental details	95
4.2 AE signals analysis	96
4.2.1 Time domain analysis	96
4.2.2 Frequency domain analysis	99
4.2.3 Wavelet packet analysis of AE signals	103
4.3 Temperature analysis	108
4.3.1 Heat evaluation during drilling process	108
4.3.2 Tool temperature and its correlation with cutting parameters	110
4.3.3 Numerical model for the validation of workpiece temperature	111
4.4 Characterization of tool wear	113

4.4.1 Correlation of tool wear with AE features	115
4.4.2 SEM characterization of drilled workpiece surface	117
4.5 Summary	118
CHAPTER–5	121
ACOUSTIC EMISSION AND INFRARED THERMOGRAPHY STUDIES IN Al-5%SiC-5%B₄C COMPOSITE	121
5.1 Experimental details	121
5.2 Analysis of acoustic emission signals	122
5.2.1 Time domain analysis	122
5.2.2 Frequency domain analysis	126
5.2.3 Time-frequency domain analysis	128
5.2.4 AE signals and tool wear	130
5.3 Temperature analysis during drilling of Al-5%SiC-5%B ₄ C composite	131
5.3.1 Heat evolution during drilling of HMMC	131
5.3.2 Types of chips formation and heat evolution with feed rate	132
5.4 Detection of tool damage	133
5.5 Characterization of drilled surface	136
5.6 Comparison AE signal characteristics, tool temperature rise and tool wear for all three MMCs.	138
5.7 Summary	140
CHAPTER – 6	143
DISCUSSION, CONCLUSIONS, SCIENTIFIC CONTRIBUTIONS AND FUTURE DIRECTIONS	143
6.1 Discussion	143
6.2 Conclusions	144
6.3 Scientific contributions	145
6.4 Future directions	146
REFERENCES	148

LIST OF FIGURES

Figure 1. 1 Schematic of different forms of tool wear in the twist drill bit	5
Figure 1. 2 Flank wear vs time curve.....	6
Figure 1. 3 The frame work of tool wear condition monitoring methods.....	8
Figure 1. 4 The process of acoustic emission	13
Figure 1. 5 Acoustic emissions with respect to load.....	16
Figure 1. 6 Types of AE signals (a) continuous type and (b) burst type	17
Figure 1. 7 Representation of different parameters of the AE signal	18
Figure 1. 8 Atmospheric transmission spectrum of infrared radiation	23
Figure 1. 9 Spectral radiance of a black body.....	24
Figure 2. 1 The photographic images of the prepared samples: (a) Al-5%SiC (b) Al-5%B ₄ C (c) Al-5%SiC-5%B ₄ C.....	36
Figure 2. 2 Drilling experimental setup (a) IRT setup (b) AE sensors and thermocouple setup.	38
Figure 2. 3 AE Disp. system for recording of AE data.....	40
Figure 2. 4 Calibration chart of wide band sensor (WSa).	41
Figure 2. 5 Schematic of AE signal acquisition and processing.....	43
Figure 2. 6 WPT decomposition tree for AE signals.....	45
Figure 2. 7 Different forms of mother wavelets.	47
Figure 2. 8 (a) Schematic of thermocouple setup in the workpiece, and (b) thermal image. ...	48
Figure 2. 9 Vision measuring microscope setup.....	52
Figure 2. 10 Surface roughness instrumental setup.	53
Figure 2. 11 (a) The interaction of electron beam with sample and the signal emitted the specimen (b) schematic of SEM instrumental setup.....	54

Figure 3. 1 Most influential factors for tool wear.	56
Figure 3. 2 Variation of AE parameters with cutting time for 600 rpm spindle speed and 0.07 mm/rev feed rate for 90° point angle: (a) AE count and (b) amplitude.	58
Figure 3. 3 AE features with cutting parameters: (a) cumulative energy vs feed rate, and (b) average AE_{RMS} vs spindle speed.	59
Figure 3. 4 AE wave forms (a), (c) and (e), and FFT spectrum (b), (d), and (f) for constant feed rate (0.07 mm/rev) and different spindle speeds (600, 900 and 1200 rpm) for Al-5%SiC composite.	60
Figure 3. 5 Time-frequency spectrum of AE signals for 600 rpm spindle speed and point angle 90° (a) AE waveform and (b) CWT spectrum.	62
Figure 3. 6 Time-frequency spectrum of AE signals for 900 rpm spindle speed and point angle 118° (a) AE waveform and (b) CWT spectrum.	63
Figure 3. 7 Time-frequency spectrum of AE signals for 1200 rpm spindle speed and point angle 135° (a) AE waveform and (b) CWT spectrum.	64
Figure 3. 8 Time-frequency-normalized amplitude spectrum of AE signals for 600 rpm speed and 0.12 mm/rev feed rate.	65
Figure 3. 9 The three level WPT decomposition of AE signal (case1).	67
Figure 3. 10 The three level WPT decomposition of AE signal (case 2).	68
Figure 3. 11 Frequency domain analysis of AE signal for friction test.	70
Figure 3. 12 Frequency domain analysis of AE signal for matrix crack test.	70
Figure 3. 13 Optical images of the cutting tool: (a) build-up edge (BUE) on the flank face (point angle 90°), (b) tool damage and abrasive wear (point angle 90°), (c) blunted edge in point angle 118°, and (d) adhesion wear in point angle 135°.	71

Figure 3. 14 Correlation of AE signal parameters and tool wear for different point angle tools: 90°, 118° and 135°, (a) average cumulative energy and tool wear vs point angle (b) wavelet coefficient and tool wear vs point angle.	73
Figure 3. 15 The variation of frequency and amplitude with tool wear for 90° point angle tool.	74
Figure 3. 16 (a) Variation of temperature rise with time for drilling at 1200 rpm spindle speed and 0.12 mm/rev feed rate for point angle 90°, and (b) normalized temperature.	75
Figure 3. 17 Thermal images of the tool during drilling (a) stage I, (b) stage II, and (c) stage III.....	76
Figure 3. 18 Variation of tool temperature and workpiece temperature with spindle speed for different point angles (a) tool temperature vs spindle speed, and (b) workpiece temperature vs spindle speed.....	77
Figure3. 19 Schematic of undeformed chip thickness in the drilling process	78
Figure 3. 20 Mesh and boundary conditions for the model.	80
Figure 3. 21 Simulated temperature distribution in the workpiece at 2 mm distance from drilled hole.	81
Figure 3. 22 SEM images of 90° point angle tool (a) abrasive wear, (b) deformed tool surface, (c) build-up-edge (BUE), and (d) adhesion of matrix.....	82
Figure 3. 23 SEM images of 118° and 135° point angle tools (a) BUE, (b) adhesion of chips on flank space in 118° point angle drill bit, (c) BUE formation on chisel edge of 135° point angle tool, and (d) adhesion wear on 135° point angle tool.....	83
Figure 3. 24 Tool wear and tool temperature for three different point angle.	84
Figure 3. 25 Surface roughness vs feed rate at different speeds for Al-5%SiC composite.	87

Figure 3. 26 Surface morphology of the machined surface (a) scratches and particle pullout in point angle 90° drilled surface and (b) material flow and cracks at point angle 135° drilled surface.	88
Figure 3. 27 Variation of chip formation at different cutting conditions for constant 0.07mm/rev feed rate: (a) speed 600 rpm and point angle 90°, (b) speed 900 rpm and point angle 118°, and (c) speed 1200 rpm and point angle 135°.	89
Figure 3. 28 SEM images of chip formation: (a) conical chip, (b) zoomed version of conical chip, (c) folding and cracks in conical chips, and (d) cracks and saw-tooth edges in lengthy chips.	90
Figure 3. 29 Variation of AE features with cutting conditions (a) cumulative count vs feed rate (b) AE_{RMS} vs spindle speed.	91
Figure 3. 30 Variation of tool temperature with cutting conditions (a) tool temperature vs spindle speed and (b) average tool temperature vs feed rate.	92
Figure 3. 31 AE_{RMS} , tool temperature and tool wear correlated for different spindle speeds (600, 900, 1200 and 1500 rpm).	93
Figure 4. 1 Variation of AE time domain parameters with time for 600 rpm speed and 0.05 mm/rev feed rate (a) AE count, and (b) amplitude.	97
Figure 4. 2 (a) AE cumulative count and (b) AE cumulative energy as a function of feed rate for different speeds.	98
Figure 4. 3 Variation of AE_{RMS} with feed rate at different speeds.	99
Figure 4. 4 AE waveforms (a and c) and its frequency spectrum (b and d) for different speeds (600 rpm and 900 rpm) at constant feed rate (0.05 mm/rev).	100
Figure 4. 5 AE waveforms (a and c) and its frequency spectrum (b and d) for different speeds (1200 rpm and 1500 rpm) at constant feed rate (0.05 mm/rev).	101

Figure 4. 6 Frequency domain analysis of AE signal (a and b) AE waveform and FFT spectrum of friction test, (c and d) AE waveform and FFT spectrum of matrix crack.....	102
Figure 4. 7 Frequency domain analysis of AE signal: (a and b) AE waveform and FFT spectrum of chip breaking, (c and d) AE waveform and FFT spectrum of tool indentation.	103
Figure 4. 8 Decomposition of AE signals for different speeds (600-1500 rpm).	107
Figure 4. 9 Wavelet energy distribution of AE signals at different speeds (a) wavelet energy ratio for band (2-3), and (b) energy ratio for band (4-16).....	107
Figure 4. 10 Three stages of temperature rise for different cutting parameters (a) temperature rise with time for 600 rpm speed and 0.05 mm/rev feed rate (b) temperature rise with time for 1500 rpm speed and 0.25 mm/rev feed rate.	109
Figure 4. 11 Three stages of thermal images during drilling of Al-5%B ₄ C composite for 1500 rpm speed and 0.25 mm/rev feed rate: (a) stage I (b) stage II (c) stage III.....	110
Figure 4. 12 Temperature rises with cutting parameters: (a) tool temperature as a function of speed at different feed rates and (b) average tool temperature as a function of speed.	111
Figure 4. 13 Mesh and boundary conditions for the model.	112
Figure 4. 14 Thermal field distribution in workpiece at 2 mm distance from drilled hole....	113
Figure 4. 15 Optical images of the cutting tool for different drilling conditions (a) after five drill holes, (b) after ten drill holes, (c) after fifteen drill holes, and (d) after twenty drill holes.	114
Figure 4. 16 SEM images of worn-out tool (a) overall view after twenty drill tests, (b) BUE formation and tool wear, (c) tool chipping, and (d) adhesion wear.....	115
Figure 4. 17 Wavelet transformation of AE signals for two different speeds and 0.05 mm/rev feed rate (a) 600 rpm, and (b) 1500 rpm.	116
Figure 4. 18 Variation of tool wear and AE parameters with spindle speed: (a) tool wear and AE _{RMS} with spindle speed, and (b) tool wear and wavelet coefficient with spindle speed. ..	117

Figure 4. 19 SEM images of drilled workpiece (a) rough surface, chip adhesion and matrix crack for 600 rpm speed at 0.05mm/rev feed rate, and (b) crushed B ₄ C particle and matrix flow for 1500 rpm speed at 0.25 mm/rev feed rate.....	118
Figure 5. 1 (a) Variation of AE count with time and (b) AE cumulative count with time at constant speed (150 rpm) and feed rate (0.1 mm/rev).	123
Figure 5. 2 AE parameters with feed rate for different speeds (a) AE cumulative count vs feed rate and (b) cumulative energy vs feed rate.	124
Figure 5. 3 AE _{RMS} with spindle speed at different feed rate.	125
Figure 5. 4 Variation of AE parameters with cutting conditions: (a, b, c) AE amplitude vs time for 150, 300, and 600 rpm speeds and (d, e, f) AE amplitude vs time for 0.2, 0.3, and 0.4 mm/rev feed rates.....	126
Figure 5. 5 AE parameters with speed for different speeds (a, c, e) AE waveforms vs time and (b, d, f) FFT magnitude vs predominant frequency.	127
Figure 5. 6 Variation of predominant frequency with feed rate at different speeds.	128
Figure 5. 7 AE signal at 150 rpm speed and 0.4 mm/rev feed rate (a) AE waveform (b) FFT spectrum.	129
Figure 5. 8 Variation of (a) cumulative tool wear and average AE energy with spindle speed and (b) cumulative tool wear and cumulative AE _{RMS} with spindle speed.	131
Figure 5. 9 Maximum tool temperature rise with feed rate at different speeds.	132
Figure 5. 10 Formation of different types of chips at 150 rpm speed and different feed rates (0.10, 0.20, 0.30 and 0.40 mm/rev) along with IR images.	133
Figure 5. 11 Optical micrograph of tool wear for different feed rates at different speeds: (a) tool fracture, (b) adhesion wear, (c) grooves on chisel edge, and (d) flank wear.	134

Figure 5. 12 SEM images of the cutting tool (a) after completion of all the drilling tests, (b) build-up-edge formation on flank space, (c) cursed surface in chisel edge and (d) grooves on chisel edge.....	135
Figure 5. 13 EDX spectrum of cutting tool after all the drilling test (a) adhesion of Al particle on flank face (b) EDX spectrum of Al particle.....	136
Figure 5. 14 SEM images of workpiece surface for drilling at different feed rates (0.10, 0.20, 0.30, and 0.4 mm/rev) at constant speed 150 rpm: (a and b) plastic flow, (c and d) wear debris (e and f) plastic flow, and (g and h) crushed particles.	137

LIST OF TABLES

Table 1. 1 Principal causes behind major industrial accidents	3
Table 2. 1 Chemical composition (wt.%) of the fabricated MMCs specimens.	37
Table 2. 2 Hardness of the fabricated composite materials.	38
Table 2. 3 The drilling experimental conditions.	39
Table 2. 4 Characteristics of drill bit used for the drilling tests.....	39
Table 2. 5 AE sensor settings.....	41
Table 2. 6 AE software and its functions.	41
Table 3. 1 L ₉ orthogonal array of the drilling test.....	56
Table 3. 2 Experimental conditions in drilling test.	56
Table 3. 3 Wavelet energy and frequency components of decomposed signals.....	69
Table 3. 4 Material properties used for the numerical simulation.	81
Table 3. 5 Analysis of variance (ANOVA) for tool temperature.	86
Table 3. 6 Analysis of variance (ANOVA) for surface roughness.	86
Table 4. 1 Conditions for the drilling tests.	96
Table 4. 2 Wavelet energy percentages for three different stages at 600 rpm speed and 0.05 mm/rev feed rate.	105
Table 4. 3 AE source mechanisms in the three stages of drilling process.	106
Table 4. 4 Material properties used for the numerical simulation.	112
Table 5. 1 Conditions for the drilling tests.	121
Table 5. 2 Wavelet energy and frequency components of decomposed signals.....	130
Table 5. 3 Comparison of AE signal, temperature rise and tool wear characteristics during drilling of MMCs.	138

LIST OF ABBREVIATIONS

AE	Acoustic emission
AET	Acoustic emission testing
ANOVA	Analysis of variance
ANN	Artificial neural network
BUE	Build-up-edge
CM	Condition monitoring
CWT	Continuous wavelet transforms
DOF	Degrees of freedom
db-20	Daubechies 20
ECT	Eddy current testing
FFT	fast Fourier transform
IRT	Infrared thermography
kHz	Kilo hertz
LPT	Liquid penetrant testing
MMC	Metal matrix composite
MHz	Mega hertz
MPT	Magnetic particle testing
MSPS	Mega sample per second
MS	Mean square
NDE	Non-destructive evaluation
NDT	Non-destructive testing
NPP	Nuclear power plant
PAC	Physical acoustic corporation
PCR	Percent contribution ratio

RMS	Root mean square
RT	Radiography testing
SEM	Scanning electron microscope
SHM	Structural health monitoring
SNR	Signal to noise ratio
SS	Sum of square
TCM	Tool condition monitoring
UT	Ultrasonic testing
VT	Visual testing
VMM	Vision measuring microscope
WPT	Wavelet packet transform
WB	Wide bandwidth

NOMENCLATURE

LIST OF SYMBOLS

B	Wein bridge displacement constant
C_p	Specific heat capacity
c	Velocity of light
dB	decibel
f	frequency
fs	Sampling rate
g	Wavelet function
h	Plank's constant
Hz	Hertz
J	Joule
K	Kelvin
k	Thermal conductivity
kHz	kilo Hertz
MHz	Mega Hertz
m/s	meter per second
m	meter
mm	millimeter
mV	Milli Volt
N	Spectral radiance
n	Wavelet decomposition
P_{out}	Power output
P_{in}	Power input
s	second
sr	steradian
t	time
T	Time period
V	Volts
V_i	Instantaneous voltage
V_{max}	Maximum voltage
V_{ref}	Reference voltage
W	Watt
%	Percentage

$^{\circ}\text{C}$	Degree Celsius
∞	Infinite
τ	Time shift
k	Boltzmann constant
λ	Eigen value
λ	Wavelength
ν	Eigen vector
ρ	density
σ_B	Stefan-Boltzmann constant
Ψ	Wavelet filter
Ψ^*	Complex conjugate of wavelet filter
ρ_r	Density of fiber
$C_{p,r}$	Specific heat of reinforcement
V_f	Volume of fiber
V_r	Volume of reinforcement
k_p	Thermal conductivity
$k_{p,c}$	Thermal conductivity of composite
t_1	Undeformed chip thickness
f	Feed rate
ϕ_p	Point angle
z	Number of cutting teeth

CHAPTER – 6

DISCUSSION, CONCLUSIONS, SCIENTIFIC CONTRIBUTIONS AND FUTURE DIRECTIONS

6.1 Discussion

- The time-domain parameters, i.e., AE counts and amplitude has successfully distinguished the drilling process into three stages such as tool entry, cutting zone and tool exit for all the MMCs. AE_{RMS} non-linearly increases with spindle speed at feed rate due to increased strain rate. The results are concomitant with earlier reported work.
- The peak frequency shift increases with an increase in speed at different point angle tool for the drilling of Al-5%SiC composite due to effect of different point angle tools. However, the peak frequency shift for Al-5%B₄C and Al-5%SiC-5%B₄C decreases with an increase in speed due to an increase in friction between the tool and workpiece.
- Time-frequency domain analysis was carried to understand the predominant frequency component existent time. The normalized amplitude, frequency and time plot has been carried out to understand the predominant frequency components at different drilling time.
- The wavelet packet transform (WPT) approach has been proposed to differentiate the damage mechanisms involved in the drilling process by decomposing the AE signals into approximate and detail components. Also, the energy percentage of decomposed components and the range of frequency band represents various damage mechanisms present in the drilling process. The application of WPT for AE signals analysis during the drilling of MMCs is performed for the first time.

- Heat evolution during the drilling of MMCs has been studied, and different stages of the drilling process are differentiated with the temperature profile. The measured tool temperature increases with an increase in speed due to an increase in kinetic friction contact between the tool and workpiece.
- The SEM micrographs confirm the different forms of tool wear such as abrasive wear, adhesive wear, tool chipping and BUE formation in the cutting edges. The SEM image confirms the presence of scratches, particle pullout, plastic flow and cracks on the drilled surface. Further, SEM has been utilized to investigate the different types of chip formation mechanisms and their characteristics (cracks, folding, shear band and flanks) in the composite chips.

6.2 Conclusions

The significant conclusions drawn from the thesis are as follows:

- ✓ The AE time-domain parameters differentiate the drilling process into three stages. The AE parameters are correlated with the cutting conditions.
- ✓ The FFT has been implemented on the AE signals to determine the fundamental frequency components present in the AE signals and the variation of predominant frequency components with cutting conditions.
- ✓ The continuous wavelet transform (CWT) has employed to find the predominant frequency component and frequency distribution existent time in the AE signals. Also, the wavelet coefficient has been extracted from the CWT spectrum and correlated with the tool wear for Al-5%SiC and Al-5%B₄C composites.
- ✓ The various damage mechanisms involved in the drilling of MMCs have been characterized using the WPT approach.
- ✓ The temperature profile reveals three stages of the drilling process and its inherent heat evolution during the drilling operations. The maximum tool temperature rise (103 °C) is

observed for 1500 rpm speed in case of Al-5%B₄C composite. The obtained tool and workpiece temperature increase with an increase in speed due to an increase in plastic deformation, and kinetic frictional contact between the tool and workpiece.

- ✓ The heat distribution in the workpiece has been studied using COMSOL model, and the experimental value has been correlated with simulated temperature in the drilling of Al-5%SiC and Al-5%B₄C composites.
- ✓ The most influential factor for tool temperature and surface roughness has been determined using the ANOVA model for the drilling of Al-5%SiC composite. The results show that the drill bit point angle 90° and cutting speed are the more significant factors for tool temperature, whereas feed rate and point angle are the most influential factors for surface roughness.
- ✓ The amount of tool wear has been quantified and compared with AE signal features such as AE count, AERMS, cumulative energy and wavelet coefficient. It is understood that the AERMS and wavelet coefficient sensitive factors for the tool wear during drilling of MMCs.
- ✓ The different forms of tool wear and workpiece damage has been confirmed by SEM micrographs.

6.3 Scientific contributions

The major scientific contributions of the dissertation are given as follows:

- ❖ The tool wear mechanism during drilling of Al-5%SiC, Al-5%B₄C, and Al-5%SiC-5%B₄C composites has been identified through better correlation of AERMS, cumulative energy of AE time domain parameters.
- ❖ Implementation of Wavelet packet transform approach on AE signals has achieved better distinguishability between the various damage mechanism such as friction, matrix cracking, plastic deformation, chip breaking, and tool wear in MMCs.

- ❖ The proposed parameter wavelet energy ratio promises better characterization of AE source from various damage mechanisms in MMCs, as first of its kind. The evaluation of the proposed parameter for speed ranges from 600 rpm to 1500 rpm has successfully established a better understanding of the energy distribution of the mechanism and its dominance at each stage of drilling.
- ❖ The signal characterization of the WPT approach is well correlated with the micrographs of tool and workpieces.
- ❖ The identification of the dynamic damage mechanism of the WPT approach in MMCs has promised its sensitivity compared with the well-established measurement on tool temperature through IRT and AE count parameter.

6.4 Future directions

It is well known that systematic experimentation, calibration, modelling, and simulation are the keys factors to the successful development of science and technology. The present thesis has significantly contributed to gaining newer insights into AE source mechanisms and heat evolution during the drilling of MMCs. However, there is still scope for further research work. The possible future directions can be explored as follows:

- The WPT can be extended to investigate the tool wear and damage mechanisms in carbide coated and diamond coated tools using AE and IRT techniques.
- Implementing WPT in ANN approach enhances the prediction rate and provides more insight into the relationship between AE parameters and tool wear during drilling of various hardness MMCs.
- Automated self-learning of processing approach can be extended by the use of machine learning improves the evaluation of the damage mechanism of MMCs.

- Inclusion of shear force and friction force in FEM analysis enhances the accuracy in prediction of tool and workpiece interface temperature.
- Microstructural studies using back scattered electron diffraction (EBSD) and transmission electron microscope (TEM) can be used to study the machining induced adiabatic shear band formation in chips, plastic deformation, and plastic flow in the workpiece and damage in the cutting tool during the drilling of MMCs.

CHAPTER – 6

DISCUSSION, CONCLUSIONS, SCIENTIFIC CONTRIBUTIONS AND FUTURE DIRECTIONS

6.1 Discussion

- The time-domain parameters, i.e., AE counts and amplitude has successfully distinguished the drilling process into three stages such as tool entry, cutting zone and tool exit for all the MMCs. AE_{RMS} non-linearly increases with spindle speed at feed rate due to increased strain rate. The results are concomitant with earlier reported work.
- The peak frequency shift increases with an increase in speed at different point angle tool for the drilling of Al-5%SiC composite due to effect of different point angle tools. However, the peak frequency shift for Al-5%B₄C and Al-5%SiC-5%B₄C decreases with an increase in speed due to an increase in friction between the tool and workpiece.
- Time-frequency domain analysis was carried to understand the predominant frequency component existent time. The normalized amplitude, frequency and time plot has been carried out to understand the predominant frequency components at different drilling time.
- The wavelet packet transform (WPT) approach has been proposed to differentiate the damage mechanisms involved in the drilling process by decomposing the AE signals into approximate and detail components. Also, the energy percentage of decomposed components and the range of frequency band represents various damage mechanisms present in the drilling process. The application of WPT for AE signals analysis during the drilling of MMCs is performed for the first time.

- Heat evolution during the drilling of MMCs has been studied, and different stages of the drilling process are differentiated with the temperature profile. The measured tool temperature increases with an increase in speed due to an increase in kinetic friction contact between the tool and workpiece.
- The SEM micrographs confirm the different forms of tool wear such as abrasive wear, adhesive wear, tool chipping and BUE formation in the cutting edges. The SEM image confirms the presence of scratches, particle pullout, plastic flow and cracks on the drilled surface. Further, SEM has been utilized to investigate the different types of chip formation mechanisms and their characteristics (cracks, folding, shear band and flanks) in the composite chips.

6.2 Conclusions

The significant conclusions drawn from the thesis are as follows:

- ✓ The AE time-domain parameters differentiate the drilling process into three stages. The AE parameters are correlated with the cutting conditions.
- ✓ The FFT has been implemented on the AE signals to determine the fundamental frequency components present in the AE signals and the variation of predominant frequency components with cutting conditions.
- ✓ The continuous wavelet transform (CWT) has employed to find the predominant frequency component and frequency distribution existent time in the AE signals. Also, the wavelet coefficient has been extracted from the CWT spectrum and correlated with the tool wear for Al-5%SiC and Al-5%B₄C composites.
- ✓ The various damage mechanisms involved in the drilling of MMCs have been characterized using the WPT approach.
- ✓ The temperature profile reveals three stages of the drilling process and its inherent heat evolution during the drilling operations. The maximum tool temperature rise (103 °C) is

observed for 1500 rpm speed in case of Al-5%B₄C composite. The obtained tool and workpiece temperature increase with an increase in speed due to an increase in plastic deformation, and kinetic frictional contact between the tool and workpiece.

- ✓ The heat distribution in the workpiece has been studied using COMSOL model, and the experimental value has been correlated with simulated temperature in the drilling of Al-5%SiC and Al-5%B₄C composites.
- ✓ The most influential factor for tool temperature and surface roughness has been determined using the ANOVA model for the drilling of Al-5%SiC composite. The results show that the drill bit point angle 90° and cutting speed are the more significant factors for tool temperature, whereas feed rate and point angle are the most influential factors for surface roughness.
- ✓ The amount of tool wear has been quantified and compared with AE signal features such as AE count, AERMS, cumulative energy and wavelet coefficient. It is understood that the AERMS and wavelet coefficient sensitive factors for the tool wear during drilling of MMCs.
- ✓ The different forms of tool wear and workpiece damage has been confirmed by SEM micrographs.

6.3 Scientific contributions

The major scientific contributions of the dissertation are given as follows:

- ❖ The tool wear mechanism during drilling of Al-5%SiC, Al-5%B₄C, and Al-5%SiC-5%B₄C composites has been identified through better correlation of AERMS, cumulative energy of AE time domain parameters.
- ❖ Implementation of Wavelet packet transform approach on AE signals has achieved better distinguishability between the various damage mechanism such as friction, matrix cracking, plastic deformation, chip breaking, and tool wear in MMCs.

- ❖ The proposed parameter wavelet energy ratio promises better characterization of AE source from various damage mechanisms in MMCs, as first of its kind. The evaluation of the proposed parameter for speed ranges from 600 rpm to 1500 rpm has successfully established a better understanding of the energy distribution of the mechanism and its dominance at each stage of drilling.
- ❖ The signal characterization of the WPT approach is well correlated with the micrographs of tool and workpieces.
- ❖ The identification of the dynamic damage mechanism of the WPT approach in MMCs has promised its sensitivity compared with the well-established measurement on tool temperature through IRT and AE count parameter.

6.4 Future directions

It is well known that systematic experimentation, calibration, modelling, and simulation are the keys factors to the successful development of science and technology. The present thesis has significantly contributed to gaining newer insights into AE source mechanisms and heat evolution during the drilling of MMCs. However, there is still scope for further research work. The possible future directions can be explored as follows:

- The WPT can be extended to investigate the tool wear and damage mechanisms in carbide coated and diamond coated tools using AE and IRT techniques.
- Implementing WPT in ANN approach enhances the prediction rate and provides more insight into the relationship between AE parameters and tool wear during drilling of various hardness MMCs.
- Automated self-learning of processing approach can be extended by the use of machine learning improves the evaluation of the damage mechanism of MMCs.

- Inclusion of shear force and friction force in FEM analysis enhances the accuracy in prediction of tool and workpiece interface temperature.
- Microstructural studies using back scattered electron diffraction (EBSD) and transmission electron microscope (TEM) can be used to study the machining induced adiabatic shear band formation in chips, plastic deformation, and plastic flow in the workpiece and damage in the cutting tool during the drilling of MMCs.

CHAPTER–1

INTRODUCTION

This chapter briefly introduces non-destructive evaluation (NDE), condition monitoring (CM), and different tool condition monitoring techniques. It describes the principles of acoustic emission (AE) and infrared thermography (IRT) and their applications for online tool condition monitoring during the machining process. Subsequently, it reports the basics of signal processing methodologies that are employed to analyse AE signals.

1.1 Non-destructive evaluation techniques

Non-destructive Testing (NDT)/Non-destructive Evaluation (NDE) are the analysis techniques widely used in science and technology. It deals with assessing the quality and structural integrity of engineering components through inspection, detection and quantification of damage and defects without causing any harm to the components [1]. NDE is a terminology often used interchangeably with non-destructive testing. However, technically NDE indicates measurements which are more quantitative in nature than NDT. NDE is an essential technology used in nuclear, aerospace, petrochemical, military and other industries to ensure various engineering components safety and reliability. The critical components such as heat exchangers of boilers, steam generators and condensers, aircraft engines, gas pipelines, etc., are subjected to NDE, essentially because their failures will affect the plant availability, production and profitability [2]. Early detection and damage assessment are necessary to confirm the safety and reliability of components. Several NDE methods are available such as visual testing (VT), liquid penetrant testing (LPT), magnetic particle testing (MPT), eddy current testing (ECT), radiography testing (RT), ultrasonic testing (UT), acoustic emission testing (AET), infrared thermography testing (IRT), and vibration analysis.

Therefore, these methods and techniques are well accommodated to particular industrial applications such as structural integrity assessment, structural health monitoring, condition monitoring, etc. through detection and characterization of damage and defects [3-4].

NDE methods can be classified into offline and online. The offline methods are VT, LPT, MPT, ECT, RT and UT, while vibration analysis, AET and IRT are online. In general, NDE methods use some form of energy, such as ultrasonic waves, X-ray radiation or electromagnetic waves, to examine a material/structure. The interaction of this energy with the material/structure is used to detect the presence of defects. NDE techniques work in three units, i.e., excitation, reception and processing [5]. In the excitation unit, a particular form of energy, e.g., electromagnetic waves, is used as input to an exciter to send energy into an object under test. The energy transformation occurs depending on the material properties and defects present in the object. A sensor picks up the transformed energy. The received energy is processed and displayed in the form of a signal to extract information about the defects [6]. AET and IRT are online techniques widely used for structural integrity and condition monitoring of components in various industries, including manufacturing industries. Mainly, tool wear is a primary issue in the manufacturing processes, which causes tool life [7-9]. The sudden tool failure in the machining process makes unexpected machine shutdown and economic loss. Thus, the online monitoring of cutting tool by using suitable NDE techniques is indispensable during machining processes. The condition monitoring methods and the use of different techniques for tool condition monitoring applications is discussed in the subsequent section.

1.2 Condition monitoring

Condition monitoring (CM) is a procedure of continuously monitoring machinery components operational characteristics to predict the necessity for maintenance before any deterioration or failure occurs. The condition monitoring process is a key strategy for

assuring plant productivity, reliability, and integrity [10]. The need for condition monitoring arises from the fact that in a power plant or machinery industry, the occurrence of any sudden fault or unplanned shutdown may result in fatal accidents or substantial economic losses. Apart from financial losses, poor maintenance machinery also leads to major accidents, which may cause environmental pollution and damage to human lives. Table 1.1 shows the principle causes behind the major industrial accidents [11].

Table 1. 1 Principal causes behind major industrial accidents[11].

Causes	Frequency (%)
Mechanical failure	38
Operational errors	26
Unknown/miscellaneous	12
Process upset	10
Natural hazards	7
Design errors	4
Arson/sabotage	3

It is evident from Table 1.1 that mechanical failure causes 38% of all major accidents, which stress the importance of efficient condition monitoring practices of machinery. In large scale industries, the maintenance cost can be as high as 40% of the total budget [12]. Bragatto et al. [13] reported that risk-based monitoring is essential for the sustained operation of critical industrial components. Therefore, condition monitoring techniques resolve these problems by providing useful information for optimally utilizing the machines.

The implementation of condition monitoring methods for damage identification in components in civil, aerospace, and mechanical industries is known as structural health monitoring (SHM), where damages are defined as the changes in material and geometric properties [14]. On the other hand, CM techniques extensively used for the metal cutting process is known as online tool condition monitoring (TCM) [15]. Tool wear is the most

undesirable characteristic of machining processes as it adversely affects the tool life, which is of primary concern in metal cutting due to its direct effect on the surface integrity and its dimensional accuracy of the machined workpiece. The cutting tool failure contributes upto 6.8% of the machining process shutdown in machining centers [16]. Hence, the tool condition monitoring (TCM) system is essential to manufacturing industries to reduce machine downtime and to enhance the productivity of manufactured components [17-18].

1.2.1 Tool wear/damage

The sharp edges of a cutting tool undergo deformation or damage during the machining process due to the interaction between the tool and workpiece known as tool wear/damage. The different forms of tool wear in the twist drill bit, as shown in Fig.1.1 [20]. Most of the cutting tools fail by catastrophic fracture or by gradual failure. When subjected to the machining process, a given tool undergoes progressive wear by friction or abrasion after a certain amount of time. This is called gradual wear, while sudden tool fracture is known as catastrophic tool fracture. There are two types of wear that any cutting tool experiences while reaching its maximum life, such as flank wear and crater wear. Flank wear occurs on the tools primary cutting edge, and it is associated with the notch and nose, while crater wear forms on the tool face that contact by chips. Flank wear directly affects workpiece dimensions and quality of the workpiece. Therefore, information about the variation of flank wear with time is necessary to replace the cutting tool and avoid scraps during machining [19]. The flank wear versus time curve is given in Fig. 1. 2 [20]. The cutting tool wears rapidly at the initial phase and then fall to a steady rate during the constant phase. From the economic point of view, the machining people would always be ready to use a tool until the tool enters into the accelerated wear region following the cutting tool ultimately fails. The other types of tool wear are classified as irregular tool wear phenomena and can generally be avoided by proper selection of tool material and cutting conditions. Breakage, fracture, and chipping fall under

this category [20]. There are three major types of tool wear mechanisms involved in the machining process, and these are (1) abrasion, (2) adhesion, and (3) diffusion. The abrasion wear occurs when a cutting tool is in contact with the workpiece, and this is always present in the machining process. The adhesion of chips or workpiece material on the cutting tool takes place during machining, which removes the cutting tool material. The adhesion wear increases with an increase in cutting temperature, resulting in diffusion of cutting tool atoms into the tool and workpiece, which accelerate the tool wear towards catastrophic failure [21-22].

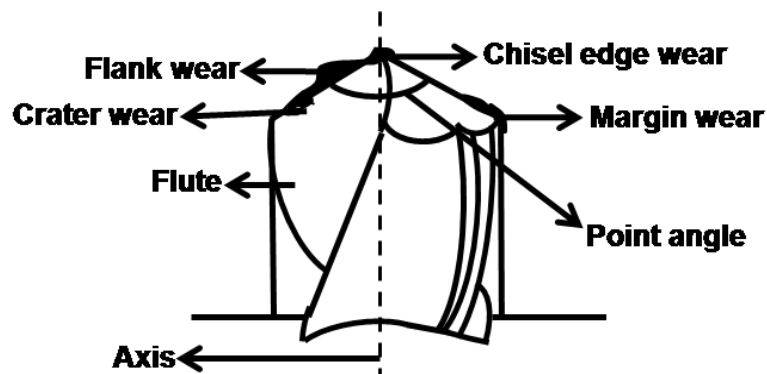


Figure 1. 1 Schematic of different forms of tool wear in the twist drill bit [20].

Fracture or failure occurs more readily in brittle tools under interrupted cutting conditions, causing complete tool failure but sometimes minor chipping of the cutting edge. The tool failure due to wear can be prevented by changing the tool periodically. However, fracturing or chipping of the cutting edge cannot be treated in the same way because it generally occurs as a catastrophic process. In order to control unexpected tool failure, followed by shortening tool life and workpiece quality, TCM plays a vital role in manufacturing industries.

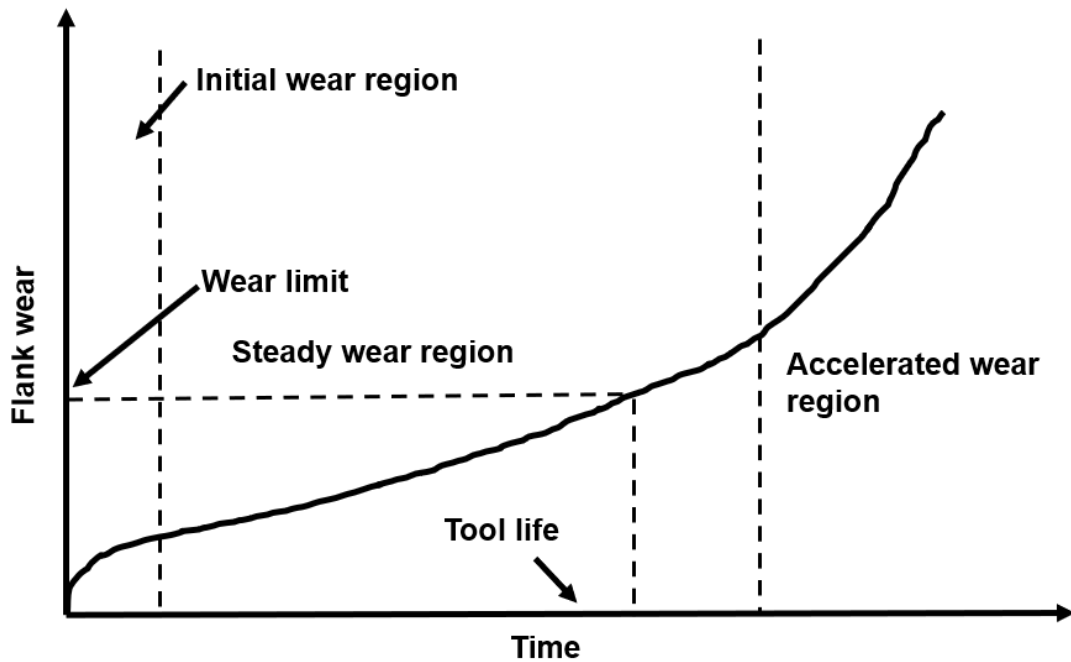


Figure 1. 2 Flank wear vs time curve [20].

1.2.2 Tool condition monitoring (TCM) techniques

Tool condition monitoring (TCM) is defined as a process of continuous monitoring the performance of a cutting tool during the material removal process. The damage or failure of cutting tools during machining operations may result in poor surface quality and dimensional error of the workpiece, and consequently, scrapping of components. In modern machining systems, cutting tools play a vital role. The catastrophic tool failure leads to the sudden halt of the whole production system, resulting in tremendous financial losses. With the application of an effective tool condition monitoring technique to the machine tool, unplanned downtime of machinery and scrapped components can be avoided [23]. Conventionally, the cutting tool during a machining operation is replaced based on the conservative estimation of past tool wear. Advances in manufacturing industries enable the use of computer numerical control (CNC) machines with automatic tool changer. On the other hand, tool wear sensing methods are developed to replace the cutting tool in machining industries. In order to replace a cutting tool during machining when the tool becomes dull, online monitoring of tool wear is essential.

The task for monitoring a manufacturing process includes monitoring the machine and dynamics of the machining process, workpiece and machine tools to assure optimal performance. Hence, the objectives of TCM can be considered as follows [24-26]:

1. Detection of tool wear in the initial stage
2. Maintaining machining accuracy by providing an accurate value of tool wear
3. Prevention of machine tool from breakage

TCM classification is mainly carried out with time domain analysis in the earlier days [27]. With these methods, a threshold value needs to set between the normal and abnormal tool states. However, the threshold value varies with cutting conditions and is difficult to determine. To improve the performance of TCM, more advanced techniques have been developed. Neural networks (NNs) are most studied and successful in practical applications due to their capability in learning and non-linear mapping of features and tool state. Besides, other pattern recognition methods i.e., as fuzzy clustering approaches, linear discriminant analysis (LDA), Gaussian mixture models (GMMs), combination of regression and neuro-fuzzy techniques, hidden Markov models (HMMs), self-organizing feature maps (SOM), support vector machine (SVM), and rough set have also been studied and applied to TCM by many researchers [28-30] as shown in Fig. 1.3.

In general, tool condition monitoring methods are classified into two categories, namely, direct and indirect methods. The direct methods include optical measurement, wear particle and radioactivity analysis, and workpiece size measurement, while indirect methods are cutting force measurement and vibration analysis. The indirect methods also include online NDE techniques such as acoustic emission and infrared thermography. These methods are briefly explained in the subsequent sections.

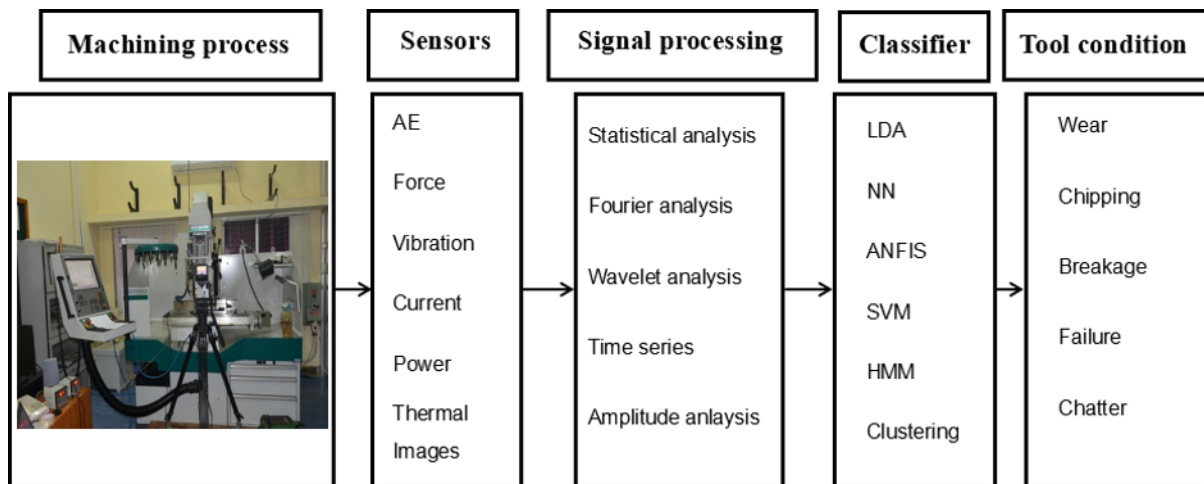


Figure 1. 3 The frame work of tool wear condition monitoring methods [31].

1.3 Direct methods for tool condition monitoring

Tool wear can be directly measured using different methods i.e., optical measurement, wear particles analysis, and workpiece size changing. These are described below:

1.3.1 Optical measurement

Optical measurement is an offline process monitoring method, and it can be employed to measure tool wear by examining the reflection of light from the cutting edges of the tool. It can be used for each cutting cycle after the removal of the cutting tool from the workpiece. The estimation of tool wear by optical measurement is known to be accurate and reliable, particularly when a vision measuring microscope is used. The wear in a single-point cutting tool appears distinctly because of the higher reflectivity as compared to the surface of an unworn tool. Optical techniques can be employed to study wear zone when the cutting tool is not in contact with the workpiece [32].

A charge-coupled-device (CCD) camera attached system is used for tool wear detection and tool life assessment in the manufacturing industries. It is a non-contact method, and thus interference with machining hardware is minimum compared to other techniques [33]. Thakre et al. [34] used a vision measuring system to study the tool wear during the turning process. The investigation reveals that the machine vision system can measure all tool wear

parameters, and it provides a precise and comprehensive picture of the tool wear [30]. Xiong et al. [35] established an image processing algorithm using MATLAB to estimate the tool wear area. The image acquisition system consists of a high-resolution CCD camera, fluorescent high-frequency linear lights, and a data acquisition module.

Fiber optic sensors are also available for online measurement of tool flank wear. In this method, the fiber optic sensor was used to measure the quantified value of flank wear (VB) not only in the central zone but over the whole wear area. This method is comparatively inexpensive to implement in the conventional production lathes or numerical controlled (NC) lathes [36]. Prasad et al. [37] used a CCD camera system for tool wear monitoring by capturing the cutting tool image during the turning process. The width and depth of the tool wear was measured from the deflection between cutting tool and the camera for each band. The Artificial Neural Network (ANN) was performed to calculate and predict the tool wear. They reported that the method was capable of capturing the three-dimensional tool wear.

1.3.2 Wear particle and radioactivity analysis

Most of the wear particles are deposited on two side surfaces of chips produced in a machining process. Thus, chemical analysis can be used to determine the amount of wear in the cutting tool. The wear particle analysis method consists of detaching the particles from the chips by pickling and filtering these particles by dissolving them in a solution. This method has the capability to separate upto 0.1 μm wear particles [38]. A scanning electron microscope (SEM) can also measure tool wear by scanning chips generated during the machining process. SEM characterization is similar to X-ray fluorescence (XRF), where electron beams are utilized to excite a sample of wear and cutting debris so that X-rays are emitted. However, the analysis of wear particle by SEM cannot differentiate between flank wear and crater wear. Nevertheless, it can provide a qualitative assessment about tool wear [39]. Bahrudin et al. [40] investigated the flank wear behaviour of micro-milling tools of 0.5-

1.5 mm for machining with titanium and H13 tool steel using an SEM. Although they were able to produce wear curves for some of the tools investigated, this was not consistent across the entire range of tools and wear was only measured for one tooth of each tool.

The radioactive sensor is another method to measure quantitative loss in the tool material. The technique primarily consists of irradiating the cutting tools wear zone by neutron particles emitted from a collimator. There are two ways to measure tool wear in this method, i.e., the analysis of abraded radioactive wear particles and the radioactive decay of the cutting tool. The cutting tool was monitored for each cycle to determine whether the radioactive material was still there. If the radioactive material had disappeared, the tool is considered to be worn out [41-42].

1.3.3 Workpiece size changing

The dimension of the workpiece will vary when the cutting tool undergoes damage, especially where tool edges contact the final machined surface. Tool wear can be measured by mapping the variation in the dimension of the machined workpiece. Different types of contact and non-contact sensors have been developed for measuring the diameter of workpieces [43]. One of the research articles reported that an electromagnetic sensing probe could be used to measure tool wear by monitoring the change in workpiece diameter during turning operations. The electromagnetic sensor measures the change in workpiece dimension. The electromagnetic sensors output voltage is directly related to the gap between the sensor and the workpiece. The sensing device can detect minute wear. However, these techniques are used to measure tool wear by detecting the variation of dimension, but they cannot diagnose the tool failure [44]. It is impossible to discriminate the different forms of wear, i.e., nose wear and flank wear. Moreover, the possibility of error exists in diameter measurement by thermal expansion of the workpiece or the inaccurate movement of machine tools during the machining process.

1.4 Indirect methods for tool wear condition monitoring

1.4.1 Cutting force measurement

Cutting force is one of the important parameters used to measure tool wear in the machining laboratory. Cutting force during a machining process is measured by an instrument called dynamometer and it consists of a sensor made up of piezoelectric element. The piezoelectric material works when compressed dynamically, and produces an electrical output. The output voltage is proportional to the dynamic force transmitted through the piezoelectric element. It is more sensitive compared to vibration and power measurement techniques. The dynamic forces from the chip formation process are measured using a force transducer. Some experimental results showed that the feed and thrust forces are influenced much more by tool wear than the main cutting force [45-46]. Choudhry and Kishore [47] proposed a relationship between flank wear and force ratio (F_f/F_c) based on the data obtained from the experiments where F_f is the feed force and F_c is the cutting force. Measurement of the ratio between the feed force and cutting force components has been found to provide a practical approach to the quantification of tool wear. Brinksmeier et al. [48] summarized that high-speed diamond tool in turning and milling processes offers a couple of advantages compared to ordinary diamond machining. It reduces machining time, cutting forces, tool wear and an improved surface finish of the workpiece during turning and milling of copper, brass, and aluminum. Other experimental work [49] has confirmed that the force components increases suddenly when a broken tool nose gets jammed between the tool and workpiece. The change in the cutting force could be used to identify tool damage or failure. It can be commented that measuring cutting forces is one of the most commonly used techniques for detecting tool failure.

1.4.2 Vibration analysis

Vibration analysis is one of the indirect methods for tool condition monitoring. During the machining process, the workpiece and chips rub against the tool and generate vibrations that

can be measured, and the information can be used for tool failure monitoring [50]. Bhuyan et al. [51] investigated different vibration signatures and associated tool wear values during turning of ASSAB-705 steel. The different vibration components can effectively describe the intensity of various occurrences during the turning process. These were able to represent the rate of flank wear progression and surface roughness of the workpiece material [51]. Data Dependent System (DDS) discrete modelling methods are used for tool wear measurement. It was also found that the DDS methodology gives the variation of friction coefficient with tool wear. A worn tool detector was constructed using a vibration transducer mounted on the tool block of the machine tool. It was found that the total amount of vibration energy in the frequency range of 4-8 kHz increases as the length of the cutting-edge wear-land increases [52]. Dimla et al. [53] used a vibration technique to investigate the tool wear during turning of EN24 steel with the coated cutting tool. The time domain and frequency domain features of the vibration signals are correlated tool wear value. The predominant frequency and tool wear values are compared. Also, they reported that the different characteristics of vibration signals are observed for the new tool and the worn-out tools.

1.5 Acoustic emission (AE) and infrared thermography (IRT) for tool wear monitoring

1.5.1 Acoustic emission testing (AET)

Acoustic emission is a phenomenon wherein transient elastic waves are generated by the rapid release of energy from localized sources in a material [54]. Acoustic emission is a dynamic technique to detect defects/flaws in materials during deformation, metal forming processes, structural integrity testing and machining processes. AET is regarded as a potential and reliable NDT method that can estimate the location, severity, and type of defect or damage in structures. When a load is applied to a material, it results in the release of transient energy/stress waves from the material. The transient energy released travels in the form of spherical wavefronts in the material. Once these stress waves reach the surface of the material,

are captured by placing a suitable piezoelectric transducer or a sensor attached to the material surface [55-56]. The sensor is mounted on the material surface using a couplant, and the stress waves are converted into electrical signals. These stress waves experience distortion and attenuation when they travel through the material. The stress waves again undergo distortion when they reach the couplant and sensor depending upon their transfer function characteristics. The AE signals captured by the sensor are amplified by using a preamplifier. A filter is used to eliminate the ambient noise and unwanted frequency components from the signals. Finally, AE signals are transmitted to the signal processor by fixing the threshold level, and the signal above the threshold are processed. The frequency range of interest in AET is from 20 kHz to 1 MHz. The process involved during acoustic emission testing is shown in Fig. 1.4.

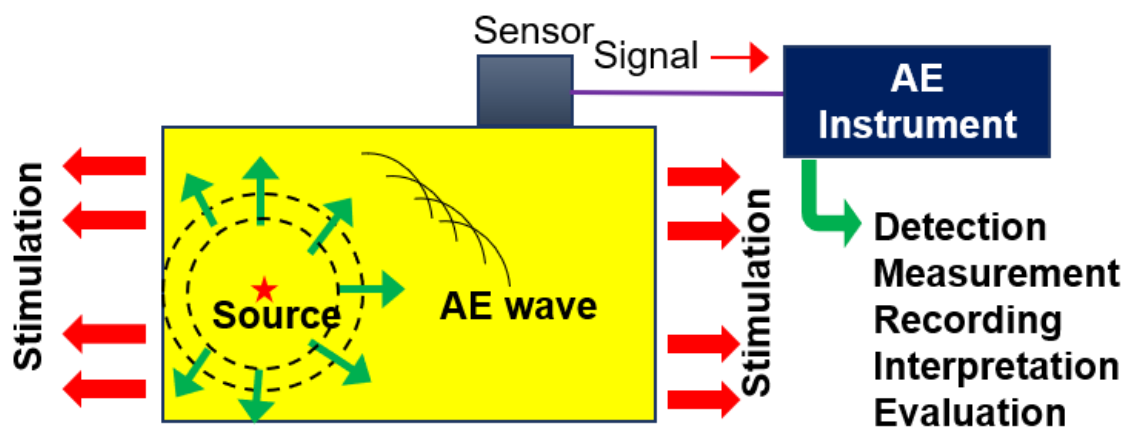


Figure 1. 4 The process of acoustic emission [54].

A few examples of dynamic AE sources in materials are dislocation movement, the occurrence of slip and twinning, phase transformation, initiation and propagation of cracks, tool wear (machining process) and fusion (welding) [57-58]. The magnitude and characteristics of the AE signal generated from the material are dependent on the type of AE source and metallurgical properties of the material under investigation. AET is used to investigate the micro-mechanisms of deformation, damage and fracture processes in materials.

The sources of AE are related to the damage and growth of defects which can be used to predict the failure of materials or structures. Acoustic emission technique is widely used for structural integrity assessment of composites, pressure vessels, pipelines, reactor vessels [59-60]. AET also plays a pivotal role in real-time condition monitoring of machinery and online monitoring of machining processes and tool wear assessment [61-63]. However, fundamental studies on AE are directed at interpreting the source mechanisms, correlation of AE signals to some physical or mechanical processes, and evaluation of the interaction of stress waves with the material/structure. Since practical applications of AE have become more demanding in recent years, more understanding of the AE phenomena is required. Understanding the AE signal generation during various material testing (plastic deformation), fracture processes, forming, joining, and machining processes is essential for the successful application of AET in condition monitoring and structural integrity assessment. The mechanisms responsible for the generation of AE signals are discussed subsequently.

1.5.2 Acoustic emission source mechanism

The common sources of acoustic emission [64] are given below: 1. Naturally occurring sources, i.e., Earthquake and Rock bursts in mines; 2. Sources in metals and composites: plastic deformation and movement of dislocations, the formation of slip and twins, crack propagation, delamination, fiber, and matrix cracking, etc. and 3. Secondary sources: Leaks, cavitation, mechanical sources of friction, etc. When a load is applied to a material, it undergoes elongation and reduction in area. Depending upon the magnitude of the applied load, the material may return to its original shape and dimension once the load is removed and this is called elastic deformation. On the other hand, if the applied load changes the original shape and dimension of the material, is called plastic deformation [65]. The generation of AE signal is very high when a material or object undergoes plastic deformation or when the object is loaded near the yield stress [66]. The atomic-scale deformation releases

a quantum of mechanical energy in the form of elastic waves (AE signal) travelling through the object. In the case of an object with the presence of a crack, the stress level at the crack tip can be several times higher than the stresses in the surrounding area. Hence, AE activity will also be observed when the material or object with crack undergoes plastic deformation. The amount of energy released by acoustic emission and amplitude of the waveform is related to the crack propagation and the amount of surface area created by the crack. Large and discrete crack jumps in the material will produce larger AE signals than cracks that propagate slowly over the same distance. Detection and conversion of elastic waves generated by mechanical deformation of a material to electrical signals is the basis of AE testing. The analysis of these signals with the appropriate domain (time, frequency, and time-frequency) yields valuable information with respect to the origin of AE signals and the severity of flaws/cracks in the material [67].

During the loading of a material, the generation of AE is governed by two different principles, such as Kaiser effect and Felicity effect. The Kaiser effect is applicable to metallic materials. If the material is unloaded after a certain amount of loading, then the absence of acoustic emission until that load is exceeded known as the Kaiser effect [68]. The cumulative emission versus load plot (Fig. 1.5) represents the Kaiser Effect (BCB), Felicity effect (DEF), and acoustic emission during hold (GH). At the initial load condition, acoustic emission events accumulate along with section AB. When the load is removed and reapplied (section BCB), AE events do not occur again until the load is exceeded beyond point B following the Kaiser effect. As the load employed on the material is increased (BD), AE signals are generated and stopped when the load is removed. However, at F, the applied load is sufficiently high to cause significant emissions, even though the previous maximum load (D) is not achieved. This phenomenon is known as the Felicity effect. This felicity effect applies

to composite materials. This Felicity effect is measured using the Felicity ratio, which is the load at which significant AE resumes, divided by the maximum applied load (F/D) [69]

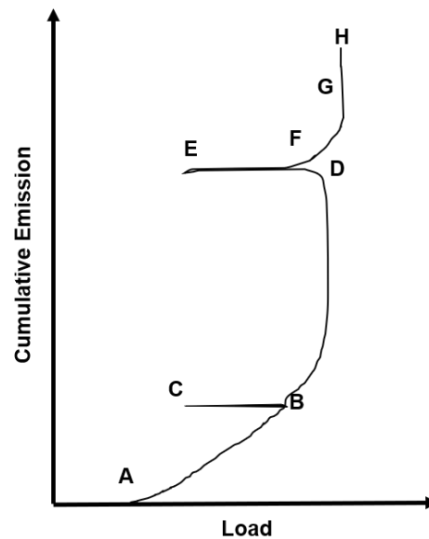


Figure 1. 5 Acoustic emissions with respect to load [69].

1.5.3 AE signal and its parameters

In general, acoustic emission signals are classified into the continuous type and burst type, as shown in Fig.1.6 (a) and Fig. 1.6 (b), respectively. The qualitative description of the sustained and time overlapping signals are called continuous type signals while discrete signals related to individual AE events occurring within the material is known as burst type signals. The amplitude and frequency content of the continuous type signal can vary over time. Plastic deformation, friction and slip are the sources of continuous signals, while crack growth, fracture and chip breakage during machining are the sources behind the burst signals [70].

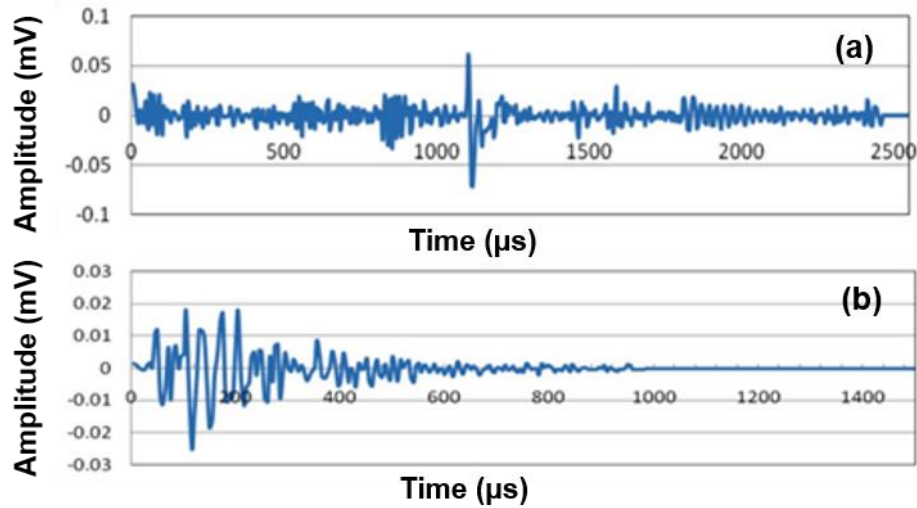


Figure 1. 6 Types of AE signals (a) continuous type and (b) burst type [70].

AE threshold setting is most important in the recording of acoustic emission signals. Only the emission events that cross a pre-defined threshold level are recorded by the AE system. During the recording of AE signals, the threshold is set to capture the only relevant signals and also to avoid the external noise. If threshold level set is below the emission event, more noise or unwanted signals will be recorded. At the same time, setting the threshold too high will put off potentially important signals from being captured. Therefore, the setting of proper threshold level is important in the AE measurement.

Peak amplitude, AE root mean square voltage (AE_{RMS}), count, energy, peak frequency, duration and rise time are the time domain parameters which are considered for the AE signal analysis. Figure 1.7 represents the different parameters of the AE signal. Amplitude is the measure of peak voltage in AE hits and is calculated using the following equation (1.1) [71].

$$A = 20 \log \left(\frac{U_{max}}{U_{ref}} \right) \quad (1.1)$$

Where, U_{max} and U_{ref} is the peak and reference voltage of the AE signal, respectively. The AE_{RMS} is another time domain AE parameter and is described in equation (1.2). It is a measure of the magnitude of signals, in spite of the shape of the waveform.

The RMS value of AE signals is considered one of the significant features for tool wear monitoring [72].

$$V_{RMS} = \sqrt{\frac{1}{T} \int_0^T V_i^2 dt} \quad (1.2)$$

Where ‘ T ’ represents the time period of the waveform, and ‘ V_i ’ is the instantaneous voltage. The peak frequency is the frequency with the maximum power of AE hit. AE counts refer to the number of pulses crossing the threshold. Depending on the magnitude of the AE event and characteristics of the material, one hit may produce one or many counts. Marse (E) sometimes referred to as energy, is the measure of the area under the envelope of a rectified linear voltage time signal from the transducer. This can be thought of as the relative signal amplitude and is useful because the energy of emission can be determined. Duration is the time difference between the first and last threshold crossings. The duration can be used to identify different types of sources and to filter out noise. Rise time is the time interval between the first threshold crossing and the signal peak. This parameter is related to the propagation of the wave between the source of acoustic emission event and the sensor. Therefore, the rise time is used for qualification of signals and as a criterion for noise filter.

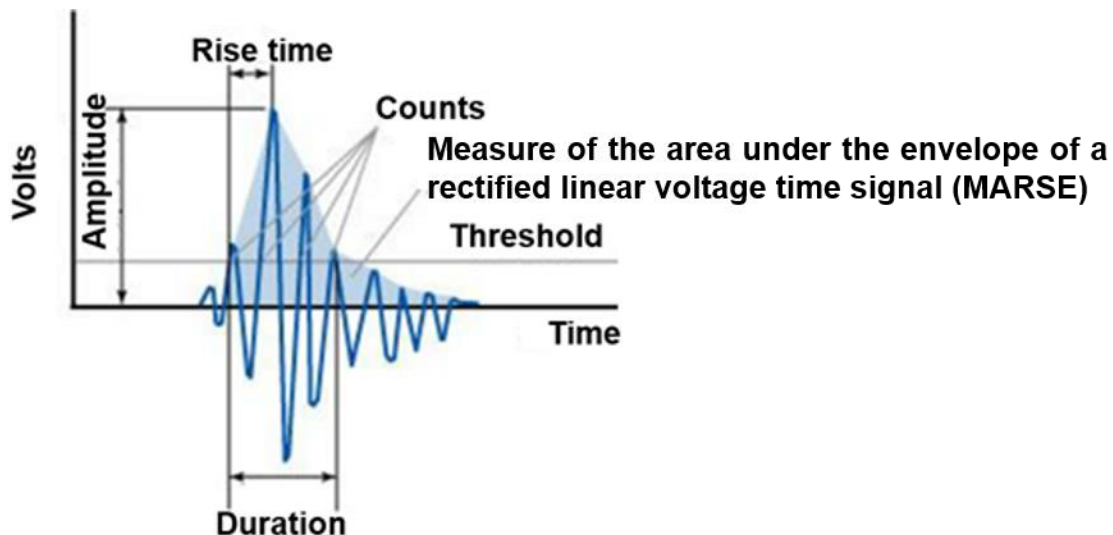


Figure 1. 7 Representation of different parameters of the AE signal [69].

1.5.4 Advantages and limitations of AET

AET is most advantageous in comparison to other non-destructive testing techniques in that AET can be used to locate and evaluate dynamic discontinuities in an entire structure at one time rather than selectively testing localized areas [71].

The advantages of AET are listed as follows:

- (1) AET gives dynamic characteristics of active defects.
- (2) It is a global volume technique, i.e., structures such as bridges, pressure vessels, storage tanks etc., can be monitored in one stroke by placing a number of sensors on them from where the source of acoustic event can be realized.
- (3) AE data gives a real-time record of progressing damage in materials.
- (4) AET can be used for location of active flaws in large components.
- (5) It can distinguish different types of active defects, i.e., characterization of different sources is possible.

The limitations of AET are as follows:

- (1) The accuracy of source localization by AET is limited.
- (2) AE signals are generated from a material only when it is stimulated.
- (3) AE gives very limited information about the size of a defect/flaw.
- (4) In AE testing, the transducer needs to be placed on the structure under test.
- (5) Test object has to be stimulated to make the defects active.

1.5.5 Applications of AET

The applications of AET [72-74] are described as follows:

- (1) Material testing: AET is widely used in tensile testing, fatigue testing of metals and alloys, corrosion detection of metal, integrity testing of composite materials, reinforced plastics testing, ceramic material testing, and tribology testing of materials.

- (2) Chemical and petroleum industries: structural integrity testing of pressure vessels and leak detection in the pipe lines.
- (3) Electric and power plant industries: Continuous power plant monitoring and diagnostics, steam line testing and continuous monitoring, partial discharge testing of transformers, quantitative steam loss evaluation of valves, continuous monitoring of furnace.
- (4) Aircraft and aerospace industries: aircraft proof testing, ageing aircraft testing, in-situ monitoring of landing gears, fatigue testing of complete structures/aircrafts, wind turbine blade and helicopter blade testing.
- (5) Manufacturing industries: tool wear and breakage detection, quality control of metal working processes, and tool condition monitoring during the manufacturing process.
- (6) Civil engineering: Testing of concrete buildings and bridges, tunnel and dam testing, etc.
- (7) Transportation application: Crack detection in railway materials and structures, condition monitoring of ball bearing of trucks and trains, crack detection of wheels and shafts of trains.

1.5.6 AE signal processing methods

The selection of proper signal processing methods of AE signals is an essential factor to explain the characteristics of acquired signals. The signal processing methods can describe the state of the cutting tool and workpiece during the machining process by analyzing the AE signals in time-frequency domain. Various techniques of signal processing are available, i.e., time domain analysis, frequency domain analysis using fast Fourier transform (FFT), and wavelet transform (WT) analysis which describes the signal in the time-frequency domain [75]. The time-domain signals are converted to the frequency domain to determine the fundamental frequency component present in the signal. The frequency-domain signals are more useful than the time domain because the time domain signals provide limited information about the AE source details.

Wavelet transform is employed in various fields such as applied physics, mathematics and engineering applications and works in the time-frequency domain. Mainly, it is utilized for tool wear monitoring and faults diagnosis of machinery components in manufacturing industries. The following advantages are the potential reason for using WT in manufacturing industries: (1) Local time dependent features can be extracted using WT, (2) More fine-tuning of the features is possible, and (3) Source mechanism can be characterized from overlapping signals using WT. The continuous wavelet transform (CWT) has the potential to analyze the stationary and non-stationary AE signals for tool wear monitoring [76].

1.6 Infrared thermography technique

1.6.1 Infrared thermal imaging

Infrared thermal imaging is also often called Infrared thermography (IRT). It is a non-contact and invasive method in which the surface temperature distribution of an object is captured based on IR radiations by using a suitable IR camera. Any object above zero Kelvin (absolute zero) emits IR radiations (associated with molecular motion). The captured radiations from the object can be converted into suitable electrical signals, processed and displayed on a monitor as a grey level. IRT quantitatively measures the surface temperatures of objects. Nondestructive testing, condition monitoring [77], predictive maintenance, gas detection, medical diagnostics and security are the major fields of applying this technique [78]. Temperature is one of the most common indicators of the structural and functional health of equipment and components. Faulty machinery, corroded electrical connections, damaged material components, etc., can cause abnormal temperature distribution [79]. Infrared thermography (IRT) is used to capture infrared radiation emitted by an object to locate any abnormal heat pattern or thermal anomaly that indicates possible fault, defects, or inefficiencies within a system or machine asset.

1.6.2 Infrared thermography system

The Infrared thermography (IRT) system consists of three major elements, i.e., optical system, detector and cooling system. The optical system consists of lenses which focus the infrared radiations reaching the camera onto the detector. The detector converts IR radiations into electrical signal, which is proportional to the intensity of the radiation. Since certain materials are opaque or partially transparent to infrared rays, lens materials commonly used for converging light cannot be used for IR radiations. Therefore, materials such as quartz, CaF_2 , Ge, and Si, which are infrared transparent, are generally used in IR camera according to the wavelength. Since the object under investigation is placed at a distance from the infrared camera, infrared radiations are likely to be absorbed by atmospheric constituents such as water vapour and natural gases (e.g., CO, CO_2 , NO and CH_4 etc.) in the intervening medium [80]. While this is not of concern in laboratory experiments where distances are small, this factor needs to be accounted in field applications such as monitoring of electrical transmission lines and mechanical installations. Figure 1.8 depicts the IR transmittance of the atmosphere [81]. It can be observed that there are strong absorptions in the wavelength range of 5.5-7.5 μm because the corresponding frequency range matches with the natural vibrating frequencies of gas molecules in the atmosphere. It is for this reason; infrared detectors are designed to work typically in the wavelength range of 3-5 μm (mid-wave infrared) and 8-14 μm (long wave infrared), where the infrared transmittance is maximum.

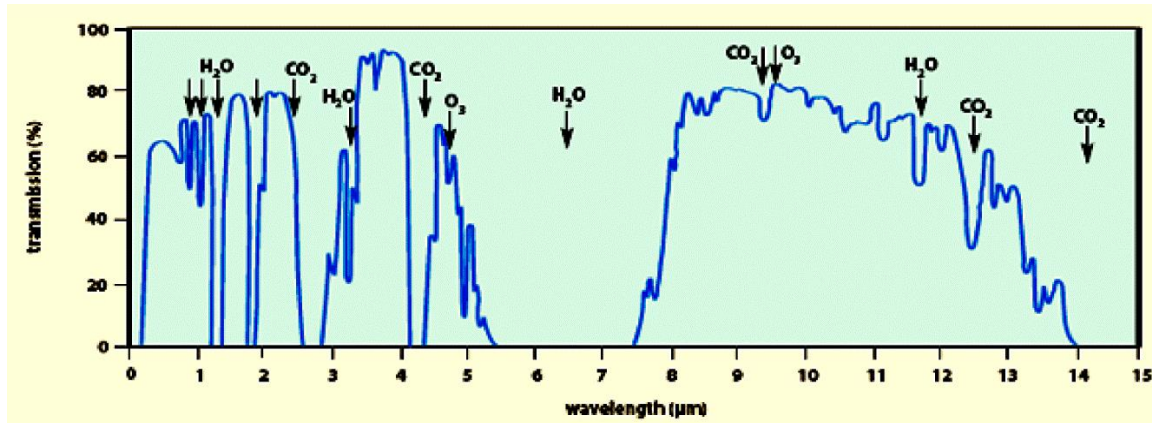


Figure 1. 8 Atmospheric transmission spectrum of infrared radiation [81].

1.6.3 Theory of IR imaging

The basic laws of radiation which govern the relationship between the spectral radiance and temperature are explained as follows. The spectral radiance (power radiated) of a black body in thermal equilibrium at a temperature T per unit surface area per unit of solid angle is defined by Planck's law as

$$N_{\lambda}(T) = \frac{2hc^2}{\lambda^5 [\exp(\frac{hc}{\lambda kt}) - 1]} \text{ W m}^2 \mu\text{m}^{-1} \text{ sr}^{-1} \quad (1.3)$$

where, ' N ' is spectral radiance of the black body, ' h ' is Planck's constant ($h = 6.626 \times 10^{-34} \text{ J s}$), ' c ' represents the velocity of light ($c = 3 \times 10^8 \text{ m/s}$), ' k ' is the Boltzmann constant ($k = 1.381 \times 10^{-23} \text{ J/K}$), and ' λ ' is the wavelength of the emitted IR radiation.

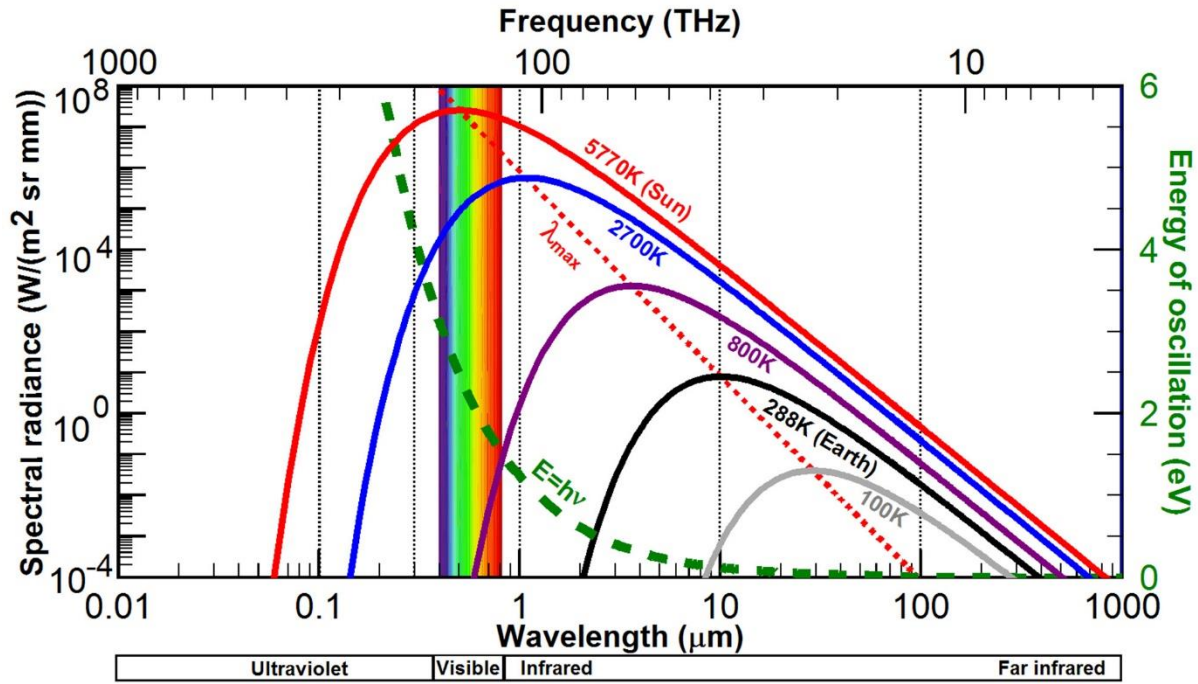


Figure 1. 9 Spectral radiance of a black body [82].

Figure 1.9 shows the variation of the spectral radiance of a black body at various temperatures. Planck's law implies that the peak emission compares to a particular wavelength. It can also be noticed that with the increase in temperature, the peak emission changes towards lower wavelength. Wien's displacement law (Eqn. 1.4) decreases the inverse relationship between wavelength and peak emission as

$$\lambda_{max} = \frac{B}{T} \quad (1.4)$$

where, ' λ_{max} ' is the peak wavelength, and B is the Wien's displacement constant ($B = 2897.7 \mu\text{m K}$).

The total radiant power (radiant power for all wavelengths) from the surface of a black body at any given temperature is defined by Stefan-Boltzmann law through the integration of Planck's law for the complete range of wavelengths ($0 \leq \lambda \leq \infty$) as

$$M = \sigma_B T^4 \quad (1.5)$$

Where σ_B is the Stefan-Boltzmann constant ($= 5.67 \times 10^{-8} \text{ W m}^{-2} \text{ K}^{-4}$) Eq. (1.5) indicates that hotter is the object, more infrared radiation is emitted by it.

1.6.4 Advantages and limitations of IRT

The advantages of IR imaging are as follows:

- (1) Non-contact, fast and reliable
- (2) Full field vision of temperature profiles
- (3) Dynamic thermal transients over a wide range of temperatures can be measured
- (4) Can be employed to measure/observe areas inaccessible for other techniques

Following are the limitations of IR imaging

- (1) Thermal losses (due to conduction, convection and radiation) can induce false thermal contrast, thereby affecting the reliability of the interpretation of thermogram.
- (2) Only sub surface defects can be studied for materials characterization
- (3) Variable emissivity

1.6.5 Applications of IRT

The common applications of IRT as follows:

- (1) Buildings: Moisture evaluation and detection of liquid level in tanks, wall assembly.
- (2) Components: Aircraft structural component and welding process inspection.
- (3) Defect detection and characterization: debonding in composites, fatigue test.
- (4) Machinery condition monitoring application and tool wear monitoring in manufacturing industries.
- (5) Medical applications: Thermal coronary angiography, soft-tissue injuries.
- (6) Materials properties: Thermophysical property studies, thermal conductivity measurement in composites.

1.7 Application of AET and IRT for tool wear and workpiece damage monitoring

1.7.1 Acoustic emission

AET is an online NDE technique and can provide useful information about the state of the cutting tool, matrix cracking, and chip formation during machining operations of composites. Drilling is one of the metal cutting processes widely used in manufacturing industries. The transient AE signals are generated when a drill bit starts indentation, followed by cutting, and the signals can be captured by a suitable piezoelectric sensor coupled with the workpiece material. The sources of AE during machining processes include tool wear, plastic deformation of the workpiece material, friction between the tool and the workpiece, chip formation, chip breaking, and fracture. Among the various sources of AE, plastic deformation and friction generate low frequency and low amplitude continuous type signals while chip breakage and tool fracture produce burst type AE signals [83]. Characterization and discrimination of a particular AE source mechanism by a single time and frequency domain parameter are difficult. Therefore, the application of suitable signal processing methods is required to extract valuable information about the AE source mechanism involved in the drilling process. Kang et al. [84] used FFT technique to monitor the spindle vibration during the machining process. The FFT analysis finds the tooth and rotation frequencies from the acquired acceleration signals. Another study by Liu et al. [85] has demonstrated that the FFT can filter and remove the unwanted frequency components and background noise from vibration signals acquired during machining process. Rubio et al. [86] applied signal processing methodologies such as continuous and discrete wavelet transform on AE signals for tool condition monitoring during the machining process. AE signal analysis could produce excellent results for identifying and evaluating the patterns with well-defined frequency and non-overlapping events. Grzesik et al. [87] executed CWT to investigate the status of the cutting tool during the turning process. It was concluded that CWT could be

suitable for the analysis of the surface roughness profiles generated during turning processes. Erkki Jantunen [88] reviewed the FFT and WT analysis methods of AE signals to extract information related to tool wear and breakage in various materials during the machining process. Lisheng Zuo et al. [89] carried out time domain, frequency domain, and time-frequency domain analysis of AE signals for tool wear detection during friction stir welding in Al-65%SiC composite. They reported that increasing tool wear increases root mean square voltage (AE_{RMS}) of AE signal, and AE energy gradually moves to the low-frequency region. Also, the wavelet packet decomposition results showed that wavelet energy increases with tool wear. Kakade et al. [90] investigated that the AE generation varies with chip formation and tool wear during the milling process in mild steel. Prakash et al. [91] conducted AE studies on aluminum alloy during the micro-milling experiment, and their results showed that the AE-specific energy and AE_{RMS} are sensitive to the formation of build-up-edge (BUE). Olufayo et al. [92] estimated tool life during end milling of H13 mould steel using acoustic emission. Time-domain and frequency-domain AE parameters such as AE_{RMS} , wavelet coefficient, AE specific energy, and wavelet sum were extracted from the signals, and it could be related to the state of the cutting tool. They concluded that cutting speed influences tool wear more adversely as compared to the feed rate. Mukhopadhyay et al. [93] reported that the statistical parameters such as kurtosis, and skewness, and b-parameter of AE signal could explain the progress of tool wear during turning of Al-SiC composite. Zarif Karimi et al. [94] applied WPT and K- means clustering to AE signals generated during drilling of glass fiber reinforced plastic (GFRP) laminates and the results can be used to identify and distinguish the sources of AE and the corresponding damage mechanisms in the GFRP laminates. The clustering of AE signals was used to classify the drilling process into three stages, i.e., tool entry, cutting, and tool exit. Karakus and Perez [95] used the AE technique to monitor the diamond drill bit during drilling of rock samples. Two different AE sensors (rock

and rig) were used, and the AE time-domain results were correlated with cutting factors. It was also reported that a change in AE signal frequency from 20 kHz to 50 kHz is associated with accelerated damage in the diamond tool. Ravishankar and Murthy [96] used the AE technique for monitoring of drilling process in glass fiber reinforced plastic (GFRP). AE_{RMS} voltage results revealed the presence of various stages in the drilling process. Also, AE_{RMS} voltage varies with the damage mechanisms in GFRP such as friction, delamination, and fiber breakage. They concluded that the AE_{RMS} voltage during drilling increases with increasing thrust force. De Rosa et al. [97] employed the AE technique to evaluate the effect of damage dissipation of jute/glass hybrid composite laminates. The AE signal processing methods such as FFT, STFT, and time-frequency analysis implemented to discriminate the various damage mechanisms.

1.7.2 Infrared Thermography

Infrared thermography is another online NDE method for condition monitoring of damage mechanism and capturing thermal images emitted by an object to extract any anomalies and defects in the objects. Drilling is one of the primary metal cutting processes that are extensively used in manufacturing industries. Excess heat generation is the major issue in drilling operations, and it affects the tool life. In the drilling process, heat energy is generated at three different zones, (1) primary plastic deformation zone, (2) secondary tool-chip interface, and (3) the tertiary zone due to friction between flank faces of the cutting tool and the workpiece [98]. The heat generation increases in the tool contact edge due to high cutting force and contact pressure build up in this region. The maximum power is converted into heat energy, and that energy gets distributed at chisel edge and tool cutting face during the drilling operation. The converted heat energy produces a high temperature in the primary and secondary deformation zones. The temperature rises in the drilling process is transferred to surrounding regions of the tool, chip and workpiece [99]. The higher cutting tool temperature

softens the cutting edge and leads to tool damage resulting in poor surface quality and dimensional inaccuracy of the drilled surface. In general, two techniques are available to measure the heat generation and distribution during drilling. In addition to IRT, contact types of thermocouples embedded in the drill bit as well as in workpiece are used to obtain continuous temperature rise in the drilling process.

In-process monitoring of cutting tool temperature and heat distribution in the workpiece is indispensable to understand the state of the cutting tool and quality of the workpiece during the drilling operation. The measurement of cutting tool temperature and associated tool wear could be useful to control the sudden tool failure and improve the quality of manufacturing products. In general, there are few techniques (i.e., direct and indirect) are available to measure the cutting tool temperature and near the tool surface of the workpiece [100-101]. Among the techniques mentioned above, direct methods such as thermocouple and infrared thermography (IRT) are widely used in drilling operations [102]. The indirect method is thermal paint and has its limitation that provides only post-process information about the maximum temperature rise. Generally, a researcher adopts direct techniques because it has many advantages compared to that of indirect method to obtain the tool and workpiece temperatures [103]. The heat distribution in the workpiece and cutting tool during dry drilling of glass fiber reinforced plastic (GFRP) and carbon fiber reinforced plastic (CFRP) has been studied using direct methods and finite element model (FEM) by Sorrentino et al. [104]. They concluded that the workpiece temperature is increased with an increase in cutting speed and feed rate and the obtained results are validated with FEM. Khaled Giasin et al. [105] reported the effect of cutting parameters (spindle speed and feed rate) on tool temperature by fixing the thermal camera under the Glass laminate aluminum reinforced epoxy (GLARE) metal laminate workpiece during drilling. Brandao et al. [106] used a thermocouple to measure the temperature of the fresh tool and worn-out tool during drilling of hardened AISI H3 steel

under minimum quantity liquid (MQL) cooling system. Their results illustrate that the worn-out tool generates higher temperature than a fresh tool. In addition to this, the effect of cutting parameters on tool and near to the cutting zone temperature was also studied. Venkatesh et al. [107] studied the influence of cutting parameters on the machinability of Inconel 718 superalloy. The workpiece temperature increases with an increase in microhardness and also reported that abrasive wear, adhesive wear, and microchipping increase with an increase in cutting speed. Using the analysis of variance (ANOVA) statistical model, Cakiroglu et al. [108] optimized the cutting parameters to study drill bit temperature during drilling of Al-7075 alloy and they concluded that the tool temperature increases with increase in cutting speed, and decreases with increase in feed rate. Eyup Bagci et al. [109] reported that the effect of feed rate on drill bit temperature during dry drilling of Al 7075-T651 alloy is insignificant. Taskensen et al. [110] used a non-contact optical pyrometer to study temperature rise during drilling of Al-B₄C composite. The multi-response optimization and grey relational analysis were performed, and the results suggest that particle volume fraction and feed rate are the most influential parameter to the tool temperature for drilling in Al-5%B₄C composite. Takeshi Yashiro et al. [111] measured cutting temperature during milling process in composite material using cemented carbide solid cutting tool. It was reported that the tool and workpiece temperatures increase with an increase in cutting speed, and the maximum milling temperature (180 °C) reaches the glass transition temperature of the composite. Komanduri and Hou [112] developed an analytical method for studying temperature distribution in chip, tool and workpiece material. Their model is in good agreement with experimental results on ultra-precision machining of aluminum alloy. Arrazola et al. [113] explored infrared microscope to study the influence of thermal field on machinability during orthogonal cutting of AISI4140 steel at various cutting conditions. The

tool-workpiece interface temperature is decreased with improved machinability characteristics.

1.8 Motivation for the study

Review of the pertinent literature reveals that both AE and IRT techniques are primarily employed for online condition monitoring of cutting tool and damage detection in workpiece, and heat evolution studies during the machining process. Many reports are available on signal processing for differentiating the sources of AE and different stages of heat evolution during machining of various metallic materials and composites. However, no open literature is found in the public domain to investigate tool and workpiece damage mechanism during dry drilling operations of metal matrix composites (MMCs) through advanced AE signal processing techniques such as continuous wavelet transform and wavelet packet transform and temperature analysis using infrared thermography. Since metal matrix composite has wide applications in automobile and aerospace industries, it is required to perform a lot of drilling works to assemble the final components. The presence of hard ceramic reinforcement in metal matrix composites and temperature rise during the drilling process cause rapid damages such as edge wear, abrasive wear, build-up edge, etc., in the cutting tool. Also, these tool damages and heat generation lead to the development of severe surface cracks and residual stress in the workpiece. Therefore, understanding of acoustic emission signals characteristics and heat evolution during drilling of MMCs is necessary to enhance the machinability of the metal matrix composites.

1.9 Objective and scope of the work

In the present thesis, tool wear, workpiece damage and heat evolution during drilling of three different metal matrix composites, i.e., (1) Al-5%SiC, (2) Al-5% B₄C, and (3) Al-5%SiC-5%B₄C are investigated for different cutting conditions, i.e., spindle speed (150-1500 rpm),

feed rate (0.05-0.4 mm/rev), and point angle (90°, 118°, 135°) by combined application of AE and IRT techniques. The major objectives of the present thesis are as follows:

- ✓ To distinguish various stages of drilling mechanism in the metal matrix composites based on AE time-domain features.
- ✓ Identification and discrimination of various AE source mechanisms during drilling of MMCs using advanced signal processing techniques.
- ✓ To establish the relationship between AE time-domain and time-frequency parameters with tool wear.
- ✓ To understand heat evolution during drilling of MMCs and measurement of tool and workpiece temperatures. Optimization of cutting tool (point angle) using temperature rise during drilling process.
- ✓ To correlate tool temperature with tool wear and validate workpiece temperature with model predicted temperature using COMSOL Multiphysics.
- ✓ The important objective of this work is the visualization of various damages in the cutting tool, drilled workpiece, and chip formation using vision measuring microscope and scanning electron microscope (SEM).

1.10 Outline of the dissertation

This dissertation is organized as follows. Subsequently after the introduction chapter (chapter 1), chapter 2 deals with the material fabrication, and characterization techniques. It also describes the importance of the chosen materials, experimental setup, drilling conditions and methodology adopted to perform the dry drilling tests. Chapter 3 includes a detailed description of acoustic emission and infrared thermography techniques for monitoring tool and workpiece damage during dry drilling of Al-5%SiC composite under different cutting conditions. The time-domain parameters of AE signals (i.e., AE count, energy, amplitude, and AE_{RMS}) are processed and correlated with the drilling parameters (feed rate, spindle

speed, and point angle). The AE count and amplitude results explore the three different stages (tool entry, cutting and tool exit) of the drilling mechanism. The frequency spectrum reveals the global frequency and predominant frequency components present in the AE signals. Further, CWT and WPT are applied to the AE signals to identify the specific frequency band and corresponding damage mechanisms operating in the drilling process. The tool wear is measured using a vision measuring microscope, and the quantified tool wear is correlated with AE_{RMS} and wavelet coefficient. Further, this chapter explains the tool and workpiece temperature rise and associated tool wear for different tool geometries. Similar to AE, heat evolution also distinguishes the three different stages of the drilling process, and the temperature rise for different cutting conditions is discussed. The most influential cutting parameters for tool temperature and surface quality of the workpiece are obtained using ANOVA model. The obtained values of tool wear are correlated with temperature rise in the drill bit. The mechanism of chip formation is correlated with temperature rise for different cutting conditions. The characteristics of tool damage and surface quality of the workpiece are examined using optical and scanning electron microscopes. Chapter 4 describes the interpretation of AE signals in different domains (i.e., time, frequency, and time-frequency) and the correlation of AE features with tool damage during drilling of Al-5%B₄C composite. The dry drilling tests are conducted for various conditions of spindle speed and feed rate. AE time-domain characteristics could distinguish the drilling mechanism into three stages (tool entry, cutting, and tool exit). The FFT spectrum of AE signal is extracted and correlated with the drilling parameters. Wavelet packet transform is applied to AE signals collected from different stages to reveal various damage sources present in the signals. The energy percentage of the decomposed components and the range of frequency band distinguishes various damage mechanisms existing in the drilling process such as matrix cracking, friction and plastic deformation. The D₂, D₃ and D₄ decomposed components show the maximum

wavelet energy percentage and their corresponding frequency bands are 62.5-125 kHz, 125-187.5 kHz and 187.5-250 kHz, respectively. These components (D_1 and D_2) are related to friction between the tool and workpiece, matrix cracking and plastic deformation. Tool wear (damage) is measured using a vision measuring microscope, and are correlated with AE_{RMS} and wavelet coefficient. Moreover, scanning electron microscope results confirm damage in the cutting tool as well as in the drilled workpiece surface. Chapter 5 explains the results of AE and temperature rise during drilling of Al-5%SiC-5%B₄C hybrid metal matrix composite. Dry drilling tests are performed for various conditions of spindle speed and feed rate. The obtained AE time-domain features are analyzed and correlated with the drilling parameters. In particular, AE_{RMS} increases with an increase in spindle speed due to an increase in strain rate. The FFT spectrum shows the variation of predominant frequency for different feed rates for constant speed. Wavelet packet transform is applied to AE signals collected from dominant frequency shift observed in the drilling tests and the different damage mechanisms identified and discriminated. The tool wear is measured and compared with AE_{RMS} and average AE energy. Temperature rise is correlated with different cutting parameters and discussed with different types of chips formation. Tool wear and surface morphology of drilled surfaces are characterized by optical microscope and scanning electron microscope. Chapter 6 concludes the thesis highlighting the significant outcome of the work carried out and discusses the scope for further investigation.

CHAPTER– 2

MATERIALS AND EXPERIMENTAL TECHNIQUES

This chapter provides the details of the fabrication process, chemical composition analysis and Hardness measurement of the prepared metal matrix composites (MMCs). The experimental techniques of acoustic emission (AE) and infrared thermography (IRT) employed during the drilling test are described. The drilling conditions, acoustic emission instrumentation, thermal imaging systems, and post-processing of AE signals are outlined. The characterization techniques adopted for the tool and workpiece damage analysis after the drilling tests are also detailed.

2.1 Fabrication of metal matrix composites

The standard methods for the fabrication of metal matrix composites (MMCs) are: (1) powder metallurgy, (2) stir casting, (3) hot isotactic pressing, and (4) squeeze casting [114]. Among these methods, the stir casting method was adopted in this work since it is simple, flexible, cost-effective and suitable for mass production and fabrication of complex composite components without damaging the reinforcement particles [115].

2.1.1 Stir casting method

Stir casting is a liquid state method and was used for the fabrication of all the MMCs samples, in which the reinforcements i.e., Silicon carbide (SiC), Boron carbide (B₄C) is mixed with a molten matrix metal (Aluminum 6061-T6 alloy) by mechanical stirring. The following methodology is adopted to fabricate the Al-5%SiC, Al-5%B₄C and Al-5%SiC-5%B₄C MMCs.

Aluminum 6061-T6 alloy 95% weight fraction and 5% weight fraction of ceramic reinforcements, i.e., SiC, B₄C, were taken to fabricate the MMCs. The average particle size

of SiC particulates was 25 μm , and 5% weight fraction (25 gm) of the reinforcement was used to prepare the MMCs. The commercially available AA 6061-T6 plates were sliced into small pieces (475 gm) and placed inside a stainless-steel crucible to preheat at 450 $^{\circ}\text{C}$ for 3 hours in resistance furnace. Further, the preheated aluminum scraps were heated above the liquidus temperature (670 $^{\circ}\text{C}$) to completely melt, and then slightly cooled below the liquidus temperature (610 $^{\circ}\text{C}$) to maintain the slurry in the semisolid state. The 2% wt. of magnesium was added to the semisolid melt to improve the wettability of the aluminum alloy. On the other hand, SiC powder particles were also preheated at 700 $^{\circ}\text{C}$ to remove moisture and enhance the wettability of the reinforcement. The preheated SiC reinforcement was then slowly added to aluminum semisolid melt under manual mixing because it was difficult to mix using the automatic device when the alloy was in a semisolid state. The composite slurry was reheated to the liquid state, and mechanical mixing (stir) was carried out for 10-15 min at an average mixing speed of 400 rpm. The final temperature was maintained at 720 ± 10 $^{\circ}\text{C}$, and the pouring temperature was controlled at 720 $^{\circ}\text{C}$. After thorough stirring, the melt was poured into the steel mold (180 mm x 70 mm x 10 mm) preheated at 500 $^{\circ}\text{C}$. The photographic images of the prepared samples Al-5%SiC, Al-5%B₄C, and Al-5%SiC-5%B₄C are shown in Fig. 2.1.

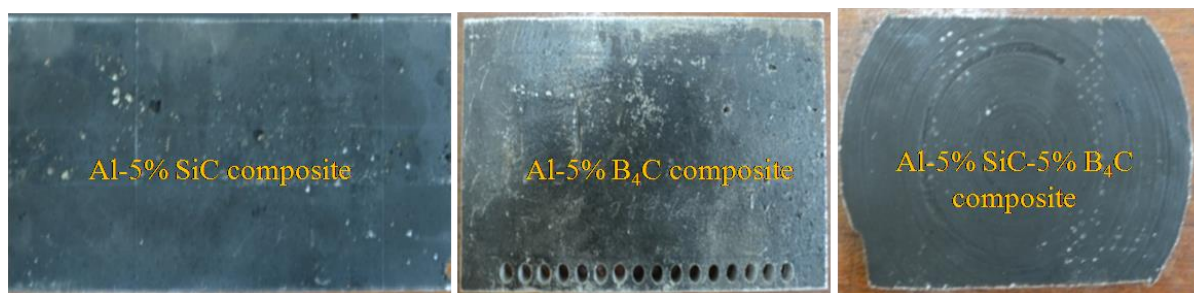


Figure 2. 1 The photographic images of the prepared samples: (a) Al-5%SiC (b) Al-5%B₄C (c) Al-5%SiC-5%B₄C.

2.2 Chemical analysis

A portable non-destructive X-ray fluorescence (XRF) spectrometer was used to identify the chemical composition (wt.%) of the fabricated MMCs and is presented in Table 2.1. X-ray spectrum was emitted by a solid sample of the MMC workpiece when a focused beam of electrons was bombarded on the sample. The spectrum displays the localized chemical component information presents in the MMC sample. In principle, elements from atomic number 4 (Be) to 92 (U) can be detected, but quantification of elements with atomic number < 10 is not reliable. It is also a quantitative analysis technique, which estimates approximate concentrations of the elements present in the material.

Table 2. 1Chemical composition (wt.%) of the fabricated MMCs specimens.

Composite materials	Cu	Fe	Mg	Cr	SiC	B ₄ C	Al
Al-5%SiC	0.20	0.35	5.2	0.12	5.00	--	Balance
Al-5%B ₄ C	0.13	0.28	4.6	0.10	--	5.00	Balance
Al-5%SiC- 5%B ₄ C	0.15	0.32	5.8	--	5.00	5.00	Balance

2.3 Hardness measurement

Hardness of the fabricated MMC specimens was measured using microhardness machine (W159PO2750). Totally five indentations are taken for each composite material, and the average hardness value is tabulated in Table 2.2.

Table 2. 2 Hardness of the fabricated composite materials.

Composite materials	Al-5%SiC	Al-5%B ₄ C	Al-5%SiC-5%B ₄ C
Hardness (HV)	88	94	112

2.4 Drilling experimental setup

Drilling tests were carried out using a computer numerical control (CNC) vertical machining center (VMC-400 Fanuc/Siemens series) having spindle power of 3.5/7.7 kW and spindle speed in the range of 40-4000 rpm. The dry drilling tests were carried out on rectangular plates of three different MMCs having different dimensions at ambient temperatures, and the experimental setup is depicted in Fig. 2.2 (a) and (b). The overall drilling conditions used in this study are shown in Table 2.3. The standard high-speed steel (HSS) tool with 5 mm diameter twist drill bit was used throughout the drilling experiment, and the characteristics of the drill bit are given in Table 2.4. A constant depth of cut 10 mm was maintained for all the drilling tests.

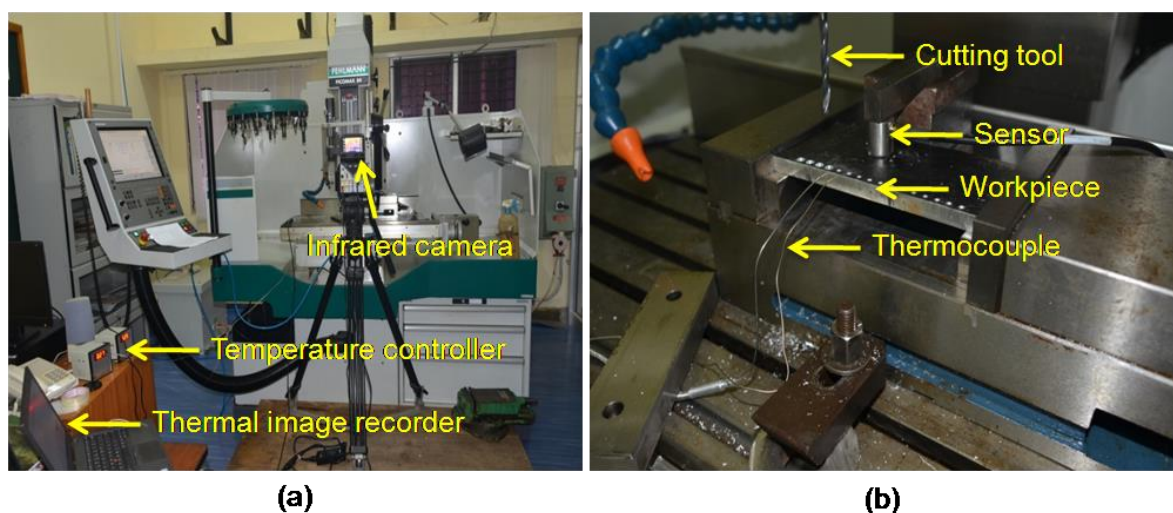


Figure 2. 2 Drilling experimental setup (a) IRT setup (b) AE sensors and thermocouple setup.

Table 2. 3 The drilling experimental conditions.

Speed (rpm)	150, 300, 600, 900, 1200
Feed rate (mm/rev)	0.05, 0.10, 0.15, 0.20, 0.25, 0.30, 0.35, 0.40
Drilled depth (mm)	10

Table 2. 4 Characteristics of drill bit used for the drilling tests.

Drill bit (material)	High Speed Steel (HSS)
Diameter (mm)	5
Drill type	Twist
Point angle/(°)	90,118,135
Helix angle/(°)	30

2.5 Acoustic emission testing instrumental setup

The acoustic emission signals were recorded during drilling of the MMC workpiece using 16 channel AE Disp system (Physical Acoustics Corporation (PAC), USA) as shown in Fig. 2.3. The sensor was firmly mounted on the surface of the workpieces by a steel clamp. A thin film of silicone grease was applied between the workpiece for good transmittance of acoustic signals to the sensor. The AE data were recorded at a sampling rate of 5 MSPS for all the drilling conditions. A threshold level of 40 dB and pre-amplifier gain of 40 dB were fixed in the AE system before the tests. In order to set the threshold, pencil lead break (PLB) tests were initially conducted [116]. In the test sensor was calibrated subsequent to the PLB tests, full trial drilling tests were conducted on the MMC workpiece. The pencil break test was conducted for the sensor calibration.

AE Disp system is provided with AEwin software for analysis of the AE signals, which provides most of the basic AE parameters like counts, amplitude, energy, and RMS etc. Depending on the requirement, parameters may be selected for analysis. Before acquiring the

AE data, pre-settings such as threshold, pre-amplification, filters sampling rate, etc., may also readily selected from the AEwin software.

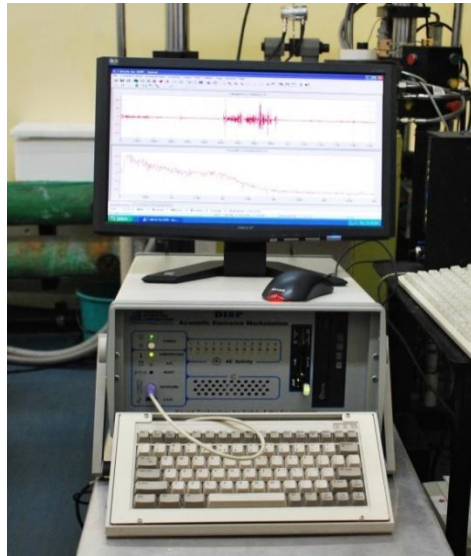


Figure 2. 3 AE Disp. system for recording of AE data.

2.5.1 Sensors

Sensors are the backbone of an AE system. A variety of sensors are available in the market with different sensitivity and frequency response. The piezoelectric wide band sensor frequency range of 20 kHz to 1MHz is one of the widely used transducers in the AE system [117]. The selection of an AE sensor with proper frequency range is important for any particular application. The frequency calibration curve of the wide band sensor is given in Fig. 2.4. Different factors need to be considered for the sensor selection, like the nature of the material, under test, type of environment, and test condition. Most of the AE sensors are specified for the typical environmental condition as one would experience during field testing or in the laboratory. The sensor has an integral preamplifier and is manufactured by M/s. Physical Acoustics Corporation (PAC), USA. A preamplifier used to reduce the external noise and amplify the AE signals in the AE testing. The typical preamplifier 40 dB provides the output of about 8 volts peak-to-peak. In this work, the wideband sensor was used, and the

AE sensor settings, as shown in Table 2.5. The signals received from the AE sensor are processed through different software, and their specific functions are shown in Table 2.6.

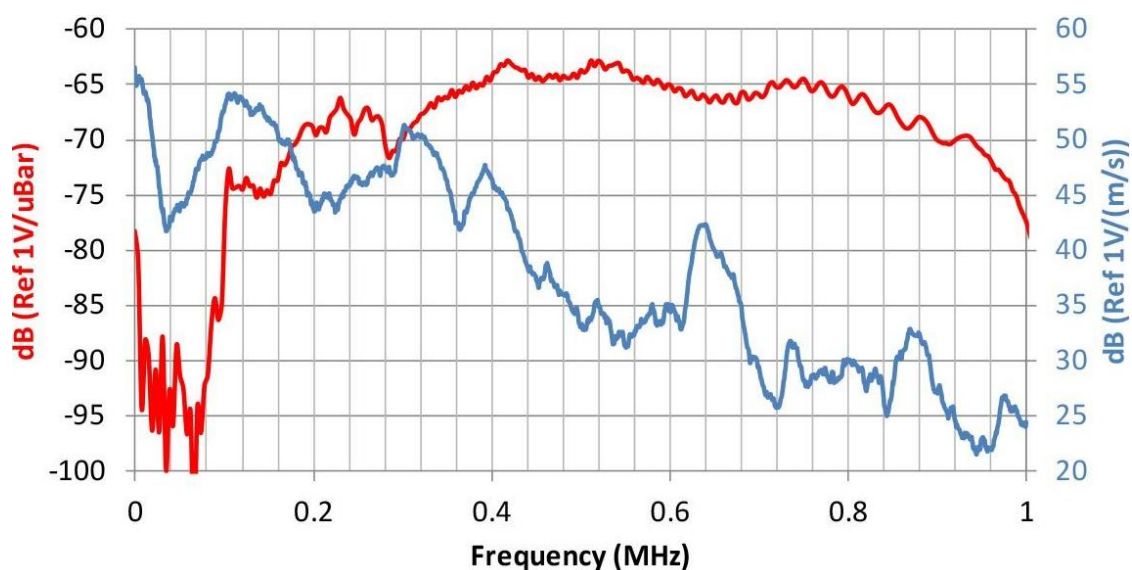


Figure 2. 4 Calibration chart of wide band sensor (WS α).

Table 2. 5 AE sensor settings.

AE system settings with wide band sensor	
Sampling rate	5 MSPS
Pre-amplification	40 dB gain
Threshold	40 dB

Table 2. 6 AE software and its functions.

Sl. No	Software	Function
1.	AE Win Disp.	Extraction of time domain parameters
2.	Noesis	Conversion of time domain signal to frequency domain
3.	Vallen Wavelet	Analysis of waveforms
4.	MATLAB	Decomposition of AE signals using wavelet packet transform
4.	Origin Lab	Plotting graphs

2.5.2 Amplification and filter

The schematic of the AE signal acquisition and processing is given in Fig. 2.5 [118]. The low amplitude AE signals are captured from a sensor, usually in the range of microvolt. The signal amplification is needed to further process the signals. The amplification of the signal was performed using an amplifier circuit which increases the power of the signals. An amplifier is a circuit that has a power gain greater than one. The amplifier gain is the ratio between output power (P_{out}) to input power (P_{in}) and is generally measured in decibel (dB). When measured in decibel, it is logarithmically related to the power ratio:

$$(Gain)dB = 10 * \log \left(\frac{P_{out}}{P_{in}} \right) \quad (2.1)$$

Filter

The sources of noise during AE testing may be due to impact loading, friction and external noise. The AE signals contaminated by background noise will influence the accuracy and reliability of the test results. So, no matter in laboratory testing or practical applications, noise control has always been an issue in AET and must be handled properly. The undesired frequency can be avoided by implementing the proper frequency range. The high bandpass and low bandpass filters were used in the AE system. The AE signals are emitted during the drilling process in the high-frequency range of 20 kHz to 1 MHz. Therefore, the cut-off frequency range was set as 20 kHz to 1 MHz [117].

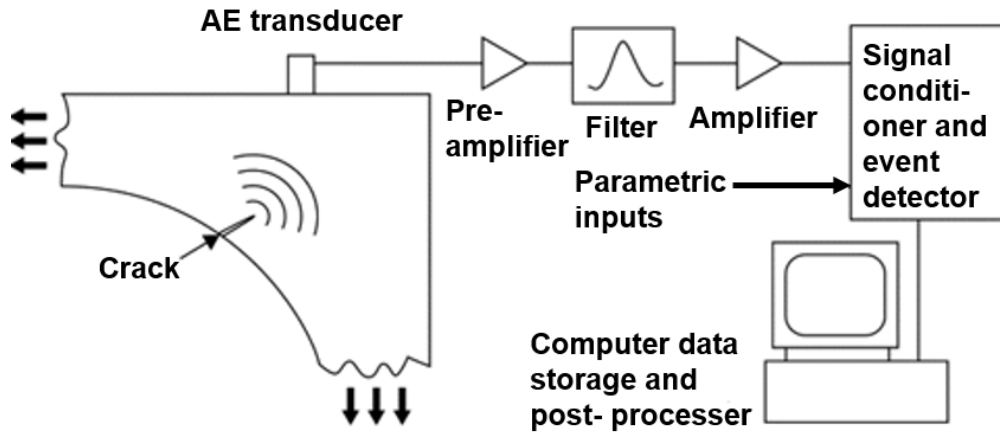


Figure 2. 5 Schematic of AE signal acquisition and processing [118].

2.5.3 Signal processing approaches

AE signals are stochastic due to multiple damage mechanisms involved in the drilling process, which generates many overlapping AE waveforms. The recorded AE signals are non-stationary with undefined waveform, and the time domain analysis is not enough to disengage various damage features in the drilling process. Thus, the frequency domain and time-frequency domain analysis are more helpful to investigate the non-stationary signals. It is significant to identify and discriminate the various damage mechanisms involved in the drilling process.

2.5.4 Frequency domain analysis

The AE time-domain signal is converted into frequency spectrum, and it represents the fundamental frequency content present in the signal. Fast Fourier Transform (FFT) converts the signals into the frequency domain signals. It is a transitional nature of the spectrum in terms of amplitude and frequency distribution. The frequency response of AE signal is expressed by equation (2.2) [119].

$$X(f) = \int_{-\infty}^{\infty} X(t)e^{-2\pi jft} dt \quad (2.2)$$

Where f is the frequency, $X(t)$ is a time-domain signal, and $X(f)$ is the signal in the frequency domain.

2.5.5 Time-frequency domain analysis

The FFT spectrum converts the AE time-domain signal into the frequency domain but does not consider the variation of the frequency component with time. Also, the determination of various damage mechanisms in composites during drilling and their associated frequency range by the FFT spectrum is very difficult. Therefore, time-frequency analysis is more useful to characterize the AE signal and the associated sources (damage) for different drilling time. The continuous wavelet transform (CWT) decomposes a signal into parts in terms of a mother signal. It deals with the non-stationary AE signals that have a short data window centred on time. In this method, AE signals are decomposed into approximated (low frequency) and detailed (high frequency) components. In the next stage, the approximated component is further decomposed into an approximate and detail component until the desired level is achieved. The commercially available Vallen software was used for the CWT analysis, and the following equation (2.3) shows the CWT function [120].

$$CWT(f, \tau) = \int_{-\infty}^{+\infty} \frac{1}{\sqrt{f}} F(t) \psi^*\left(\frac{t-\tau}{f}\right) dt \quad (2.3)$$

Where ' f ' shows frequency, ' τ ' represents the time shift, and ψ^* shows the complex conjugate of wavelet.

2.5.6 Wavelet packet analysis

The wavelet packet transform (WPT) approach has been implemented to understand the frequency band of AE signals and the related damage mechanisms in composites during the drilling process. In the present study, WPT is implemented to the AE signals, which are decomposed into approximate (A) low frequency components and detail (D) high frequency components. Further, both the approximate and detail components are decomposed to their own approximate and detail components, not as in CWT, where only approximate signals are

decomposed [121]. The WPT is applied to the recorded AE signals, and the decomposition tree is illustrated in Fig. 2.5.

The wavelet packet is given by Eqn. (2.4), where ‘ i ’ is modulation parameter, ‘ j ’ is the scale parameter and ‘ k ’ is the translation parameter.

$$\psi_{j,k}^i(t) = 2^{\frac{-i}{2}} \psi^i(2^{-j} t - k) \quad (2.4)$$

In the above eq. (2.3), $i = 1, 2, \dots, j^n$ and ‘ n ’ represents wavelet decomposition level. ψ^i can be derived from equations. (2.5) and (2.6).

$$\psi^{2i}(t) = \frac{1}{\sqrt{2}} \sum_{k=-\infty}^{+\infty} h(k) \psi^i\left(\frac{t}{2} - k\right) \quad (2.5)$$

$$\psi^{2i+1}(t) = \frac{1}{\sqrt{2}} \sum_{k=-\infty}^{+\infty} g(k) \psi^i\left(\frac{t}{2} - k\right) \quad (2.6)$$

ψ^i is main wavelet and $g(k)$ and $h(k)$ are discrete filters that depends on dilation parameter and wavelet function.

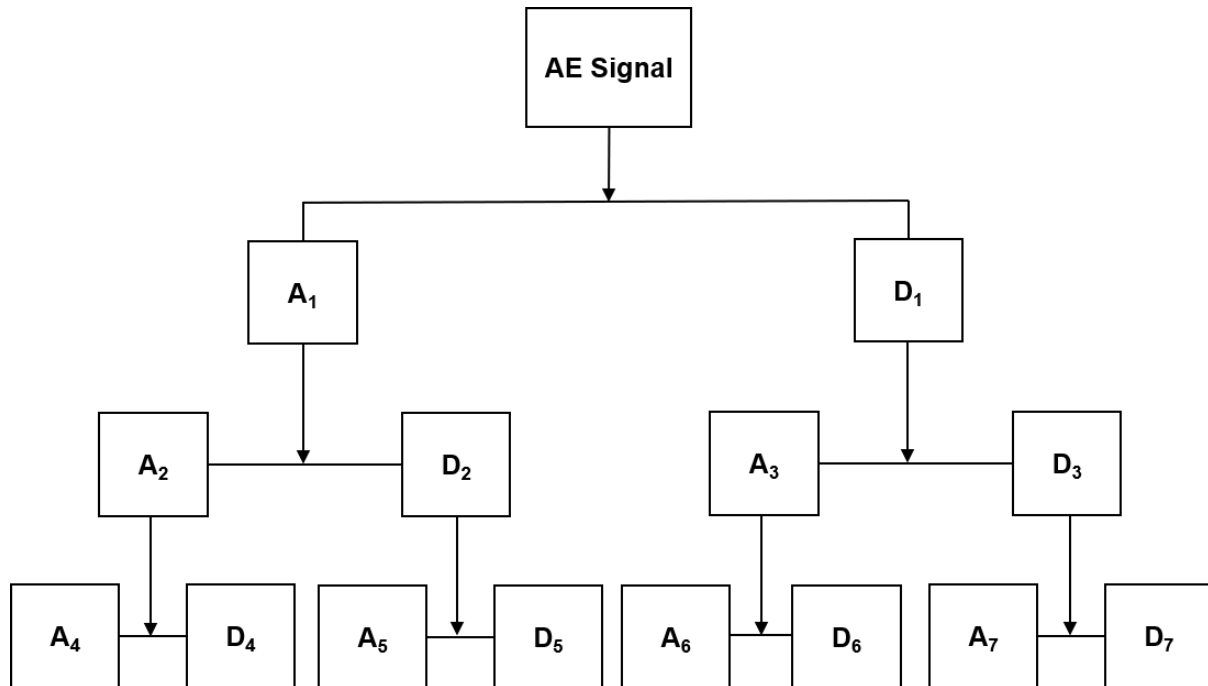


Figure 2. 6 WPT decomposition tree for AE signals.

The decomposition of approximate and detail components and their corresponding frequency ranges were calculated by using equations (2.7) and (2.8).

$$\left[0, \frac{1}{2} f_s 2^{-i}\right] \quad (2.7)$$

$$\left[\frac{1}{2} f_s 2^{-i}, \frac{1}{2} f_s 2^{-(i-1)}\right] \quad (2.8)$$

Where f_s is the sampling rate, and 2^i is the number of components in the i^{th} level. It shows that AE signals are decomposed into a set of wavelet components, and each component has a specific frequency range. In this work, wavelet packet decomposition and energy percentage features were extracted by using MATLAB. The wavelet energy criteria were employed for the decomposition since each component of wavelet packet energy is related to some specific damage mechanism. The wavelet energy content of each decomposed component is determined by using the following equation (Eq. 2.9).

$$EC_i(t) = \sum_{\tau=t_0}^t (f_i(\tau))^2 \quad (2.9)$$

Where $EC_i(t)$ represents the i^{th} energy component of a certain level. The total energy of a given level is defined as the summation of energy for all the components. The ratio of energy for each component and the total energy are used to determine the energy percentage (EPC) for each component, as shown in Eq. (2.10).

$$EPC_i(t) = \frac{EC_i(t)}{EC_{Total}(t)} \quad i = 1 \dots 2^j \quad (2.10)$$

Where, ' j ' is the level of decomposition, and ' i ' is the number of components.

There are two important factors in the wavelet packet theory, i.e., number of levels and selection of suitable mother wavelet.

The following methods were used to select the number of levels.

1. Mathematical criteria called entropy
2. Selection of optimum level based on systematic trials.

In the present investigation, the “Shannon” entropy was used, and the optimum level was set to three ($j=3$) for the wavelet packet transform. A three level ($j=3$) decomposition contains

eight components ($i=2^3$). Among various standard mother wavelets, the appropriate mother wavelet was selected based on visual assessment, to match the acquired AE signals.

2.5.7 Selection of mother wavelet and levels

The mother wavelet was selected based on the similarity with the obtained AE signals. There are different forms of Daubechies mother wavelet, as shown in Fig. 2.7. Among all the Daubechies wavelets, it was found that the db20 wavelet (Daubechies wavelet family) matches with the recorded AE signature. The Daubechies wavelets are appropriate to analyse the transient AE signals. It is also biorthogonal and efficiently supports wavelets to the AE activity. The decomposition level (j) was selected based on the sampling frequency and predominant peak frequency present in the AE signals.

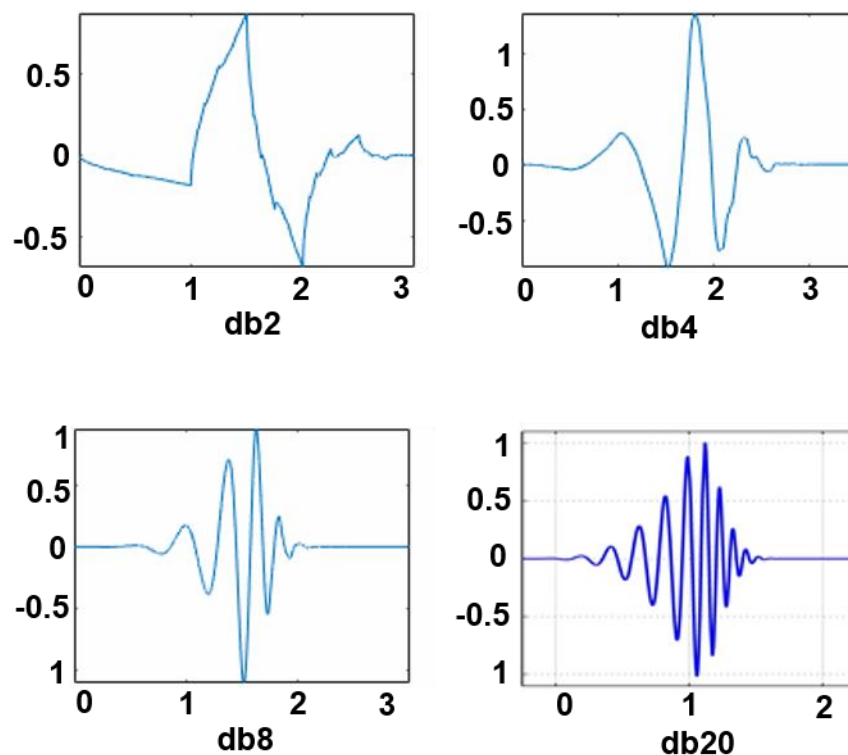


Figure 2. 7 Different forms of mother wavelets [122].

2.6 Infrared thermography experimental setup

A FLIR infrared camera was used to capture the thermal images of the cutting tool during the drilling tests. An indium antimonide (InSb) focal plane array (640×512) detector was used in

the thermal camera with a spectral range of 1.6-5.1 μm . The infrared thermography camera has a sensitivity of 25 mK and a frame rate of 100 Hz. The detector elements are cooled by the Stirling cycle. During the drilling tests, a constant distance (70 cm) was maintained between the thermal camera and the workpiece. Two K-type (NiCr-Ni) thermocouples, each with a diameter of 1 mm and length of 2-meter wires, were used to obtain the workpiece temperature during the drilling process. The thermocouples were embedded (locations) in the sidewall of the specimens. The position of the thermocouples was maintained at a constant distance (2 mm) from the drill hole. The temperature variation was noted throughout the drilling experiments. The box profile was used to measure the tool temperature, as shown in Fig. 2.8. IR camera used for this study measures the temperature value with an accuracy of $\pm 1\%$ of the scale on the thermogram.

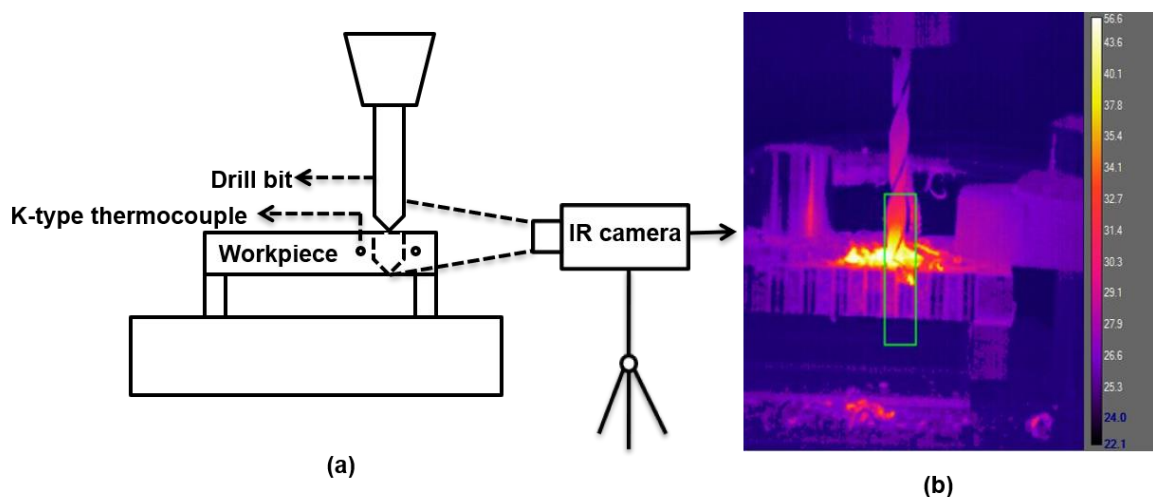


Figure 2. 8 (a) Schematic of thermocouple setup in the workpiece, and (b) thermal image.

2.6.1 Emissivity calculation

The emissivity of a material is a significant factor which affects infrared radiation. The emissivity difference shows different types of thermal images, even though it carries the same temperature. Thus, the emissivity of the cutting tool should be known a priori. The emissivity of the cutting tool surface was determined by applying a high emissivity coating.

The black paint (matt finish) was applied to the object. Coating materials like black tape typically has a thermal emissivity value > 0.90 . The measured cutting tool emissivity was 0.95. The emissivity has been determined as follows:

1. Matt finish black paint was applied to the tool.
2. The entire surface of the black paint was allowed to reach an equilibrium temperature with the target object (tool).
3. A known emissivity value of the black paint on the thermal imager was set. The temperature of the area where the black paint was applied was measured. It was ensured that the thermal imager is focused and perpendicular to the tool. The temperature values at the region of interest (black painted area) were recorded on the thermal imager.
4. The imager was then moved and refocused to the uncoated area on the tool. The emissivity value on the imager was adjusted to obtain a similar temperature reading as the coated area. This provided a very good estimation of the unknown thermal emissivity value.

2.6.2 Detector

Detector is the heart of an IRT system. The quality of detector determines the efficiency with which temperature profiles of the object can be mapped with required sensitivity. Detectors are generally classified as thermal detectors and photon detectors.

Thermal detectors

Thermal detectors work on the principle of change in any physical property like electrical resistance due to temperature rise as a result of incident radiation. They in general have a flat spectral response and important thermal detectors are explained below.

Bolometer: Bolometer is a thermal infrared detector with very high temperature coefficient of resistance and less heat capacity. Hence, when radiation is incident on the absorber material, temperature increases with decrease in resistance as a result of increase in kinetic

energy of the free electrons. Vanadium oxide and amorphous silicon are examples of bolometer detectors.

Photon detectors

In photon detectors, a change in the charge carrier concentration of the material is introduced as a result of incident infrared radiations, thereby changing the electrical properties like electrical conductivity. These detectors have high thermal sensitivity and short response time. There are different types of photon detectors as follows.

Photovoltaic detectors: Photovoltaic detectors work on the principle of photovoltaic effect, according to which, when a semiconductor is exposed to radiation, electron-hole pair is produced. The internal electric field (built-in potential) at the p-n junction separates the electron-hole pair and moves the electron into the n-type region and the hole into the p-type region resulting in an open circuit voltage that can be measured externally. Mercury cadmium telluride (HgCdTe), Indium arsenide (InAs), Indium antimonide (InSb) and platinum silicide (PtSi) are examples of photovoltaic detectors. These detectors are commonly employed for Infrared measurement, heterodyne filtering and metrology applications.

2.6.3 Cooling systems

To limit the noise induced in the measurement by heating of the detector the following cooling methods are employed. Cryogenic cooling uses liquefied gases (e.g., H₂, N₂ and He) stored in a cryogenic storage dewar vessel attached to the detector. Closed Stirling cooling, another effective method, involves repetitive expansion and compression of a gas (nitrogen or argon) by a piston. Thermoelectric cooling is based on Peltier effect which involves the generation of cooling through flow of current from one side of the Peltier element to other side, is also employed. Thermoelectric devices do not generate any vibration and hence are suitable for thermal detectors. On the other hand, photon detectors need to be cooled to less than 77 K and hence can be cooled only through thermodynamic cycle such as Stirling

cooling. In general, Stirling cooling system is the most widely used method for cooling infrared detectors because of the lower temperature that can be attained with reduced size and weight of the Stirling system.

2.7 Tool and workpiece damage analysis

The qualitative and quantitative analysis of tool and workpiece damage was carried out using different characterization techniques i.e., vision measuring microscope, surface profilometer and scanning electron microscope.

2.7.1 Vision measuring microscope

Vision measuring microscopes (tool makers microscope) includes an optical microscope with a table capable of precise movement of targets for measurement. An optical comparator and a telecentric optical system are used to enable precise measurements. The measurements are performed in a non-contact manner, so that there is no risk of damage to the cutting tool. The quantitative damage in the cutting tool was measured using vision measuring machine (INSPECT VISTA 3020 CNC) having 0.1 μm resolution and the instrumental setup with cutting tool as shown in Fig. 2.9. The damaged area in the cutting tool was marked and the calculated area was taken as tool damage/wear. The steps followed to measure the tool damage are given below:

1. Fixing the target sample within the holder and placing on the stage.
2. The light passed on the target through optical lenses, and the reflected light or transmitted light is observed in the monitor. The damaged edges in the cutting tool are marked with the reference line.
3. The damaged area was quantified using AutoCAD software. The dimension of the wear area was marked in the optical image of the damaged tool. The marked area was executed in AutoCAD software and the area of tool wear was calculated.

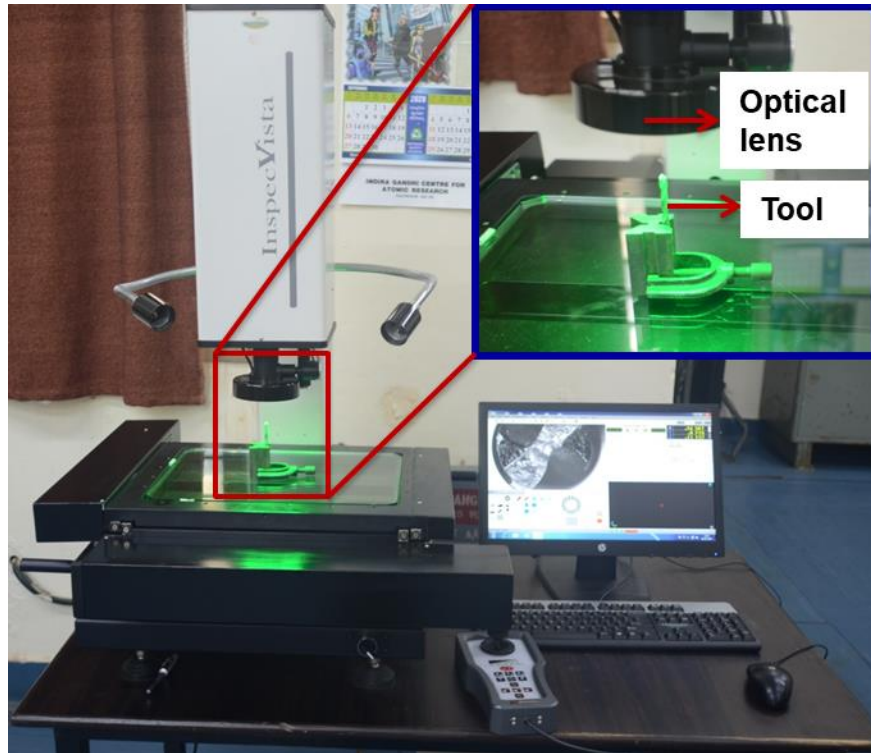


Figure 2. 9 Vision measuring microscope setup.

2.7.2 Surface profilometer

Surface profiler is a scientific measuring instrument for topographical characterization of object surface layers. It is a multipoint measuring technique and is used to estimate the sub-micron (μm) textural variation of the surface. The variation of texture in the sub-surface may contribute to a directional lay, which can have a distinct effect on the physical properties of the material. These textures should be measured to control the ongoing performance wear on the surface of a mechanical component. The surface roughness is carried out through the contact method. A diamond stylus is used to probe the workpiece surface and detect the roughness, physically moving a stylus along the surface to acquire the dimensional fractality and surface roughness. This can record surface deformations and fluctuations in friction. The surface roughness of the drilled specimens was measured using Mitutoyo surftest (TR-200, TIME) and the instrumental setup as shown in Fig. 2.10. For this purpose, the diamond tip was used with the maximum measuring range of $160\ \mu\text{m}$. After calibrating the system with

standard quartz material, the surface roughness measurement was carried out at three different places on the drilled surface, and average values are reported. The surface roughness measurement was conducted as per ISO 1997 guideline [123]. The measured surface roughness (Ra) was correlated with the drilling parameters.

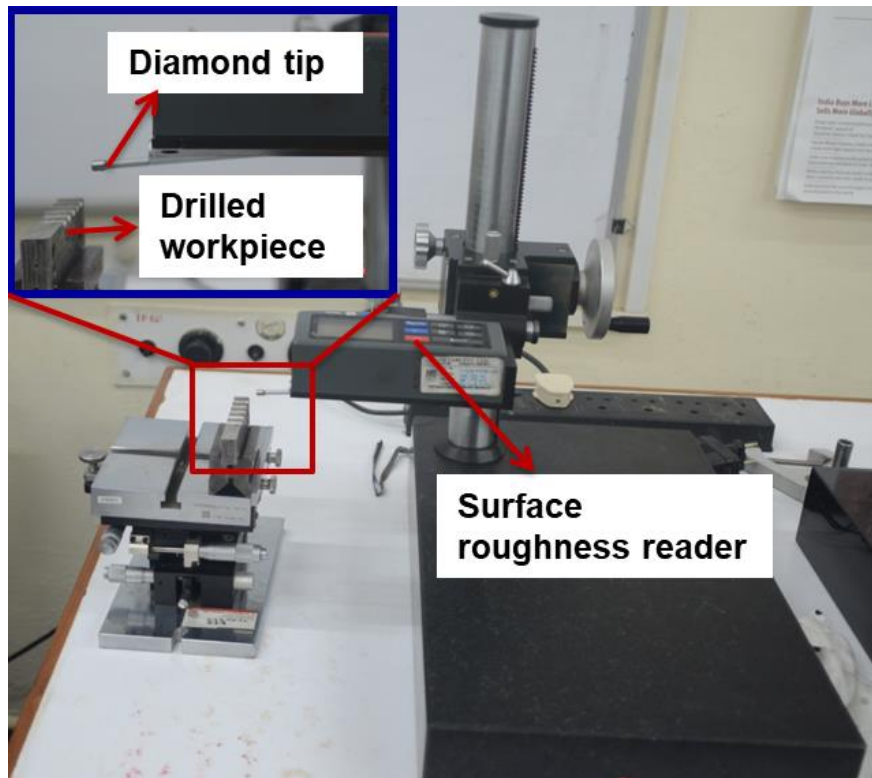


Figure 2. 10 Surface roughness instrumental setup.

2.7.3 Scanning electron microscope

A scanning electron microscope (SEM) provides surface topography images by scanning a focused electron beam over the material surface. The focused beam of electrons bombards the sample, producing various signals that can be used to obtain information about the surface morphology and topography. The SEM is one of the best analytical instruments with its extensive applicability in the study of solid materials. The SEM is critical in all fields that require the characterization of solid materials. SEM was utilized in the current study for characterizing the surface microstructure of the drill bit and drilled workpieces. The FEI make dual beam FEGSEM was used to study the morphology of the cutting tool and

workpiece damage. Accelerating voltage in the range of 5-30 kV and beam current from 1.4 nA to 5.5 nA were utilized based on the requirements. The interaction of electron beams with sample and schematic of SEM, as shown in Fig. 2.11.

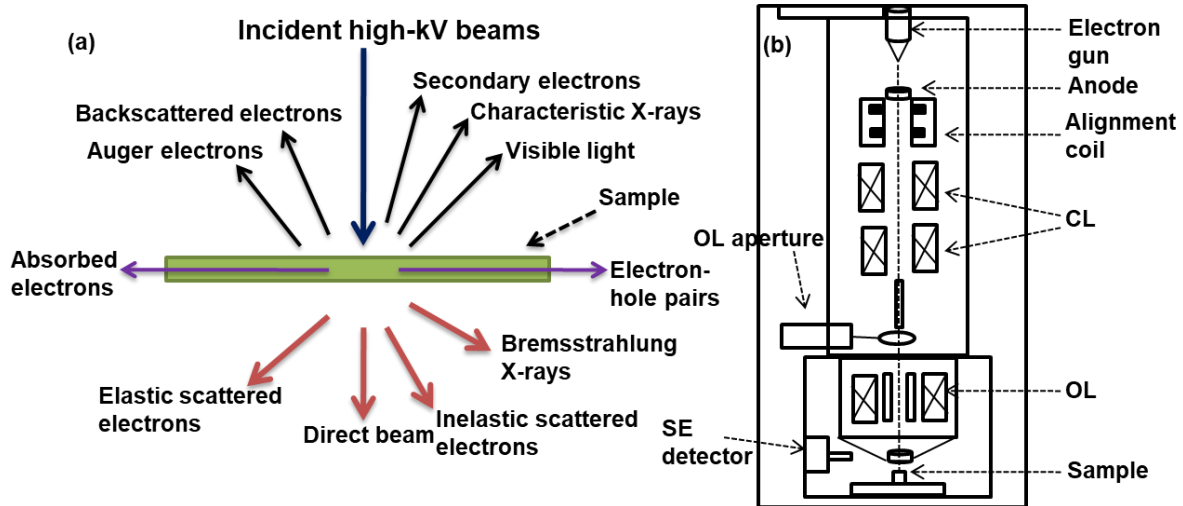


Figure 2. 11 (a) The interaction of electron beam with sample and the signal emitted the specimen (b) schematic of SEM instrumental setup.

2.8 Summary

Al-5%SiC, Al-5%B₄C and Al-5%SiC-5%B₄C metal matrix composites were fabricated by the stir casting method. Chemical analysis and hardness measurements of the fabricated materials were carried out. The details of the drilling tests and characteristics of the cutting tool are given. Acoustic emission testing setup comprising of AE instrument, sensor, filter and preamplifier are discussed in this chapter. AE signal processing methodologies namely continuous wavelet transform and wavelet packet transform for discrimination of various damage mechanism involved in the drilling process have been proposed. The IRT testing instrument, emissivity, detectors, and cooling systems are included. The cutting tool and workpiece damage characterization techniques such as vision measuring microscope, surface profilometer, and scanning electron microscope are also presented.

CHAPTER– 3

**ACOUSTIC EMISSION AND INFRARED THERMOGRAPHY STUDIES
IN Al-5%SiC COMPOSITE**

This chapter discusses the combined use of AE and IRT for understanding the damage mechanisms and heat evolution during drilling of Al-5%SiC composite under various cutting conditions. The characterization of AE signals at different domains (time, frequency and time-frequency) explores the various damage mechanisms involved in the drilling process. Heat evolution for different cutting parameters and the most influential factors for tool temperature is studied. A COMSOL Multiphysics model was implemented to validate the workpiece temperature. The correlation of AE features and tool temperature with tool wear is discussed in detail. The surface quality of the drilled workpiece and damage in the cutting tool are analyzed using scanning electron microscope (SEM).

3.1 Experimental details

The dry drilling experiments were performed on Al-5%SiC MMC workpiece (70 x 100 x 10 mm³). The three different point angle (90°, 118°, 135°) were utilised (optimize the best point angle tool) for the drilling of MMCs. Towards this, Taguchi's L9 orthogonal array design of drilling experiment was performed, as shown in Table 3.1. The tool wear can be assessed by addressing the effect of tool geometry, cutting parameters and temperature rise during the drilling process. The most influential parameters for tool wear are given in Fig. 3.1.

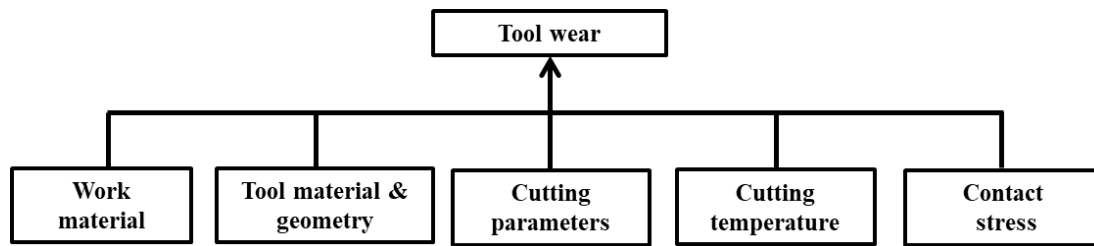


Figure 3. 1 Most influential factors for tool wear.

Table 3. 1 L₉ orthogonal array of the drilling test.

Sl. No	Spindle speed (rpm)	Feed rate (mm/rev)	Point angle (°)
1	600	0.07	90
2	600	0.12	118
3	600	0.17	135
4	900	0.07	118
5	900	0.12	135
6	900	0.17	90
7	1200	0.07	135
8	1200	0.12	90
9	1200	0.17	118

The best point angle tool (118°) was selected from the above experimental outcomes (tool temperature). Further, the obtained 118° point angle tool was utilized to study the effect of varying speed and feed rate on AE signal and tool temperature. The experimental conditions as shown in Table 3.2.

Table 3. 2 Experimental conditions in drilling test.

Spindle speed (rpm)	600, 900, 1200, 1500
Feed rate (mm/rev)	0.05, 0.10, 0.15, 0.20, 0.25, 0.30, 0.35, 0.40
Drilled depth (mm)	10

3.2 Acoustic emission signal analysis and discrimination of damage mechanisms

3.2.1 AE Time domain analysis

The variations of AE counts and amplitude with cutting time for 600 rpm spindle speed, 0.07 mm/rev feed rate, and 90° point angle are shown in Fig. 3.2(a) and Fig. 3.2(b), respectively. Based on the results of AE counts and amplitude, the drilling process can be differentiated into three stages, such as stage I (tool entry), stage II (cutting zone), and stage III (tool exit), as shown in Fig. 3.2. In stage I, low magnitude AE counts and low amplitude signals (40 dB - 60 dB) are observed upto around 11 sec. This is due to initial tool indentation and shear deformation in the workpiece during the starting of the drilling process, which contains both burst and continuous types of AE signals. The rigorous cutting commences in stage II, which is termed as cutting zone. Wherein, higher AE counts and higher amplitude (78 dB - 98 dB) signals are observed upto around 23 sec due to continuous matrix crack propagation, friction, and chip collision/breakage. Both burst and continuous types of signals are generated in this stage. Moreover, it is noted that the magnitude of AE counts in stage II varies randomly with cutting time, and this is due to the uneven emission of AE events. In stage III, a decrease in AE counts and low amplitude signals are observed due to tool exit from the workpiece, where only friction/rubbing only occurs between the tool and workpiece. Therefore, continuous types of signals are detected in stage III.

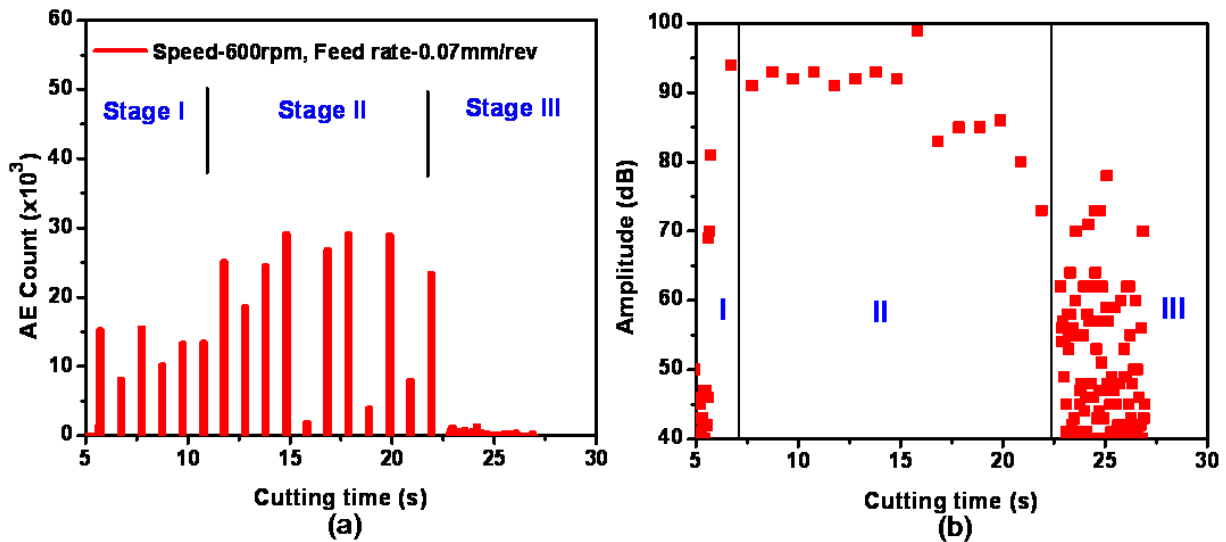


Figure 3. 2 Variation of AE parameters with cutting time for 600 rpm spindle speed and 0.07 mm/rev feed rate for 90° point angle: (a) AE count and (b) amplitude.

Similar trend is observed for all the feed rates (0.07 - 0.17 mm/rev) at 600 rpm spindle speed. However, the observed three stages disappear with an increase in the feed rate (0.07-0.17 mm/rev) at different spindle speed (600-1200 rpm). This is due to decrease in the contact time between the tool and workpiece. The existence of three stages in the drilling of MMC is concurrent with the earlier reported results [94, 96].

The variation of cumulative energy with feed rate for different spindle speed is shown in Fig. 3.3 (a). The cumulative energy decreases with an increase in feed rate and spindle speed due to a decrease in the time of contact between the tool and workpiece. Moreover, at 600 rpm spindle speed, the cumulative energy decreases drastically with feed rate than the higher spindle speeds (900 rpm and 1200 rpm). Nevertheless, for 0.07 mm/rev feed rate and 600 rpm spindle speed, the high AE energy is observed due to an increase in the time of contact between the tool and workpiece. AE root means square (AE_{RMS}) voltage is an important time-domain parameter and measure of the magnitude of the signals inspite of the shape of the waveform. AE_{RMS} value is considered as one of the important features for monitoring cutting tool damage. Figure 3.3 (b) shows the variation of average AE_{RMS} with spindle speed for

different feed rates. It is observed that the average AE_{RMS} increases with an increase in spindle speed for different feed rates and is attributed to the increase in strain rate. These results are in good agreement with the earlier reported work for the drilling of polymeric composite [96,124].

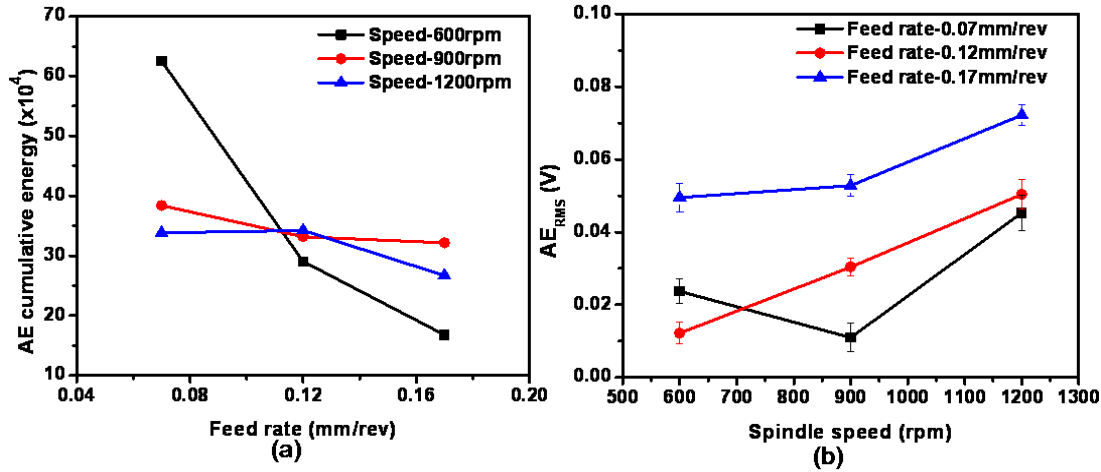


Figure 3. 3 AE features with cutting parameters: (a) cumulative energy vs feed rate, and (b) average AE_{RMS} vs spindle speed.

3.2.2 AE Frequency domain analysis

AE signals are stochastic in nature, and multiple damage mechanisms operating in the drilling process generates many overlapping AE waveforms. The time-domain parameters are not sufficient to extract valuable information about different damage mechanisms involved in the drilling process. Therefore, the AE time-domain signal is converted into the frequency spectrum to understand the fundamental frequency content present in the signal. The natural frequency of drill bit, tool holder, and workpiece is less than 5 kHz and were neglected [125,126]. However, the frequency range of the acoustic emission signal is 20 kHz to 1 MHz. Frequency domain analysis of AE signals was carried out as per the equation (2.1). Frequency analysis of AE signals in the cutting region (stage II) for the tests with 0.07 mm/rev feed rate was carried out. AE waveforms for three test conditions, i.e., (1) 600 rpm spindle speed and 90° point angle, (2) 900 rpm spindle speed and 118° point angle, and (3)

1200 rpm spindle speed and 135° point angle, are shown in Figs. 3.4 (a), (c) and (e) respectively. These three test conditions also represent the first test conducted by three different point angle tools. The frequency spectrum results for the above three test conditions are shown in Figs. 3.4 (b), (d), and (f) respectively.

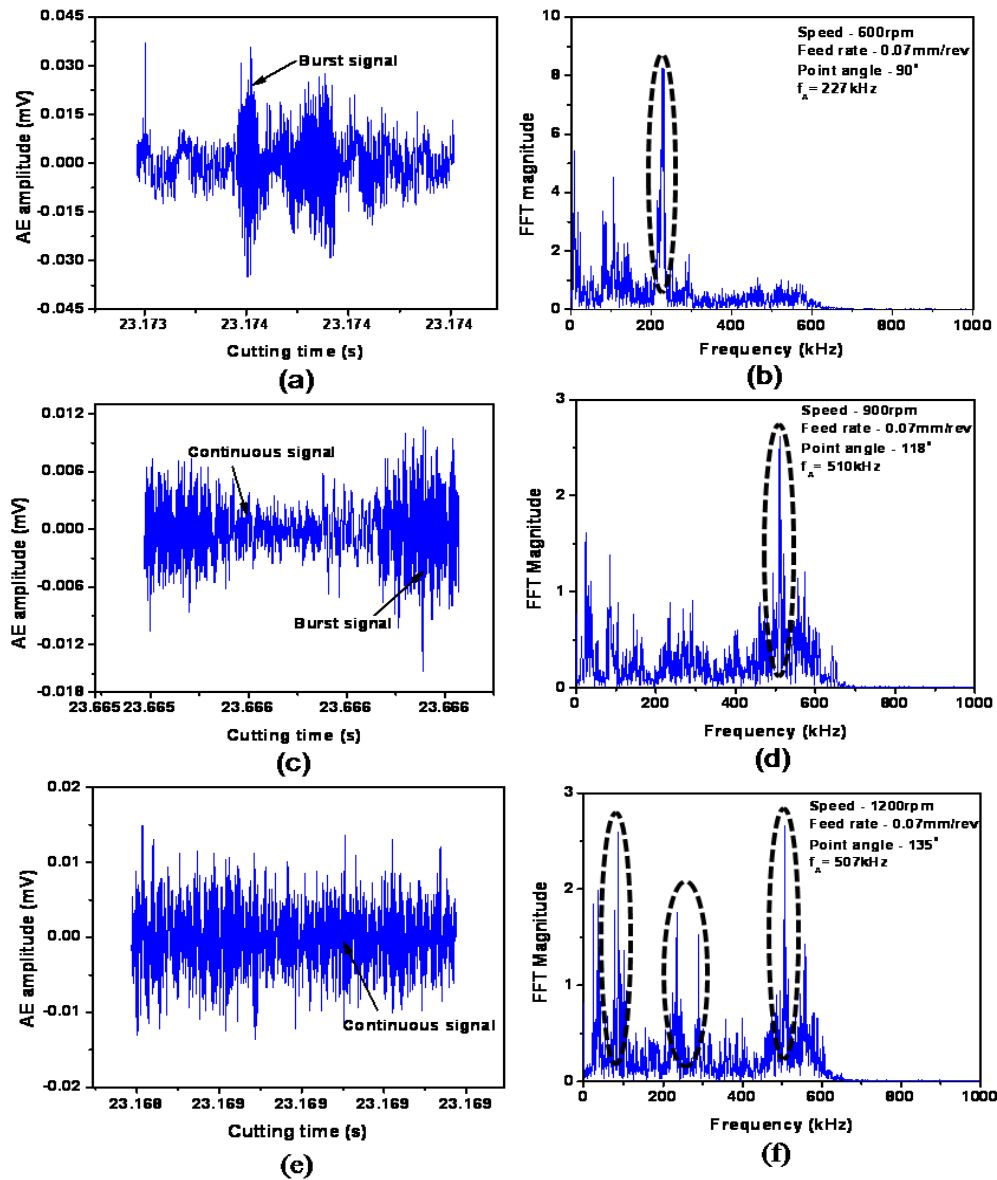


Figure 3. 4 AE wave forms (a), (c) and (e), and FFT spectrum (b), (d), and (f) for constant feed rate (0.07 mm/rev) and different spindle speeds (600, 900 and 1200 rpm) for Al-5%SiC composite.

In Figs. 3.4 (a), (c), and (e), arrow marks indicate burst type signals due to crack propagation and chip collision/breakage, and continuous type signals are due to plastic deformation and friction. In Figs. 3.4 (b), (d), and (f), dotted curves indicate predominant frequency peaks (227, 510, and 507 kHz) for the above three test conditions. The increase in the peak frequency with is due to high chip collision and breakage [127].

3.2.3 Continuous wavelet transform

The FFT converts the AE time domain signal into frequency domain but does not consider the variation of the frequency component with time. Therefore, time-frequency analysis is more useful to extract the AE signal characteristics at different drilling time. The continuous wavelet transform (CWT) decomposes a signal into parts in terms of a mother signal. The CWT was applied to the AE signals. The three waveforms used for frequency domain analysis described in section 3.2.2 were also used for CWT analysis. Figures 3.5-3.7 reveal the CWT of AE signals and frequency with cutting time. The AE waveform, CWT spectrum, and line frequency spectrum for test condition 1 mentioned in 3.2.2 i.e., for 0.07 mm/rev feed rate, 600 rpm spindle speed, and 90° point angle, are shown in Figs. 3.5 (a) and (b) respectively. It is observed that the dominant burst signals with high amplitude are recorded.

The signal was extracted from stage II of the drilling process and thus this is due to chip breakage and crack propagation in the matrix. Chip breakage and crack propagation are major sources for burst signals. It can be seen that the signal with predominant frequency 227 kHz is excited at 375 μ s, and this is associated with the wavelet coefficient value of 4.91. The distribution of low-frequency (100-200 kHz) band is noticed upto 650 μ s. The CWT results of AE signals for test condition 2, i.e., for drilling at 0.07 mm/rev feed rate, 900 rpm spindle speed, and 118° point angle, are shown in Figs. 3.6 (a) and (b). Figure 3.6 (a) depicts that both burst and continuous type signals are excited in this test condition. It is noticed from Fig. 3.6 (b) that the dominant frequency of 510 kHz is excited at 150 μ s, and also, a band of

scattered high-frequency components in the range of 200-500 kHz is observed upto 300 μ s. The wavelet coefficient of the AE signal decreases from 4.91 as observed for the test condition 1 to 1.28 for test condition 2. These observations are due to an increase in continuous type AE signals in test condition 2, which is associated with an increase in friction between the tool and workpiece.

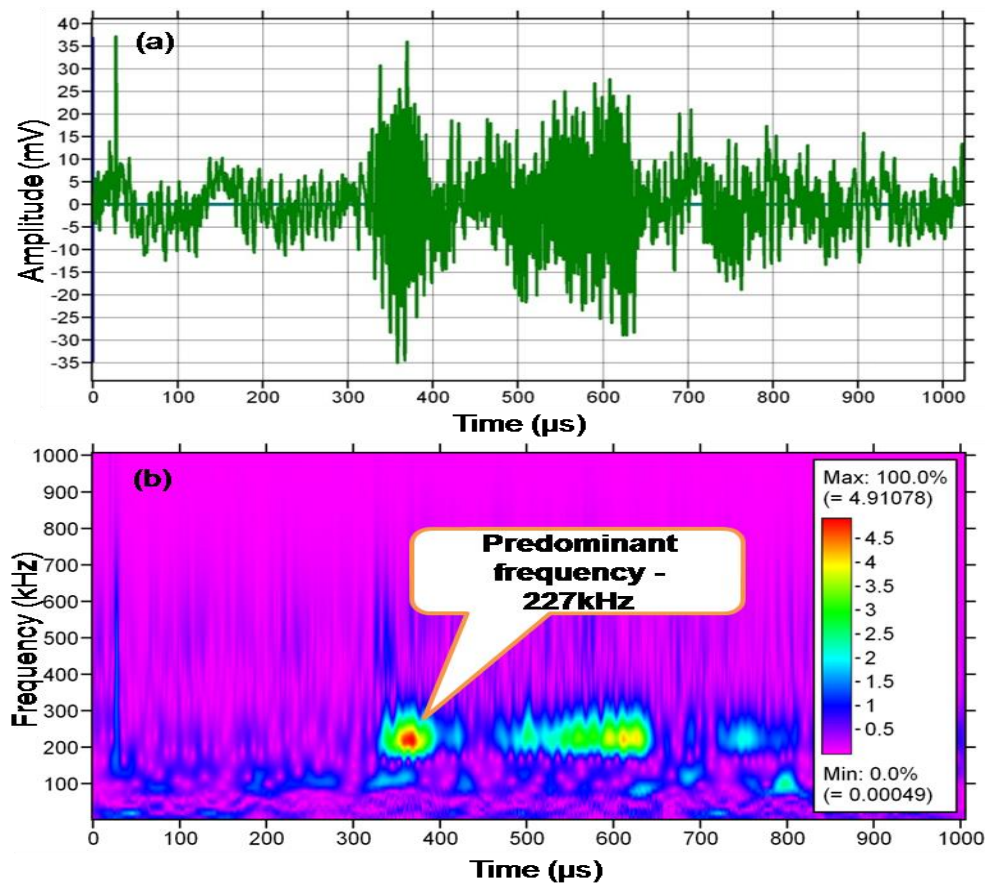


Figure 3. 5 Time-frequency spectrum of AE signals for 600 rpm spindle speed and point angle 90° (a) AE waveform and (b) CWT spectrum.

The CWT results for test condition 3, i.e., for 0.07 mm/rev feed rate, 1200 rpm spindle speed, and 135° point angle, are shown in Figs. 3.7 (a) and (b). The low amplitude continuous types of waveforms are predominant due to severe friction taking place at higher spindle speed (1200 rpm). Figure 3.7 (b) reveals that more scattered dominant high-frequency components

(100 kHz to 550 kHz) are noted upto 800 μ s, and the associated wavelet coefficient value is 1.1.

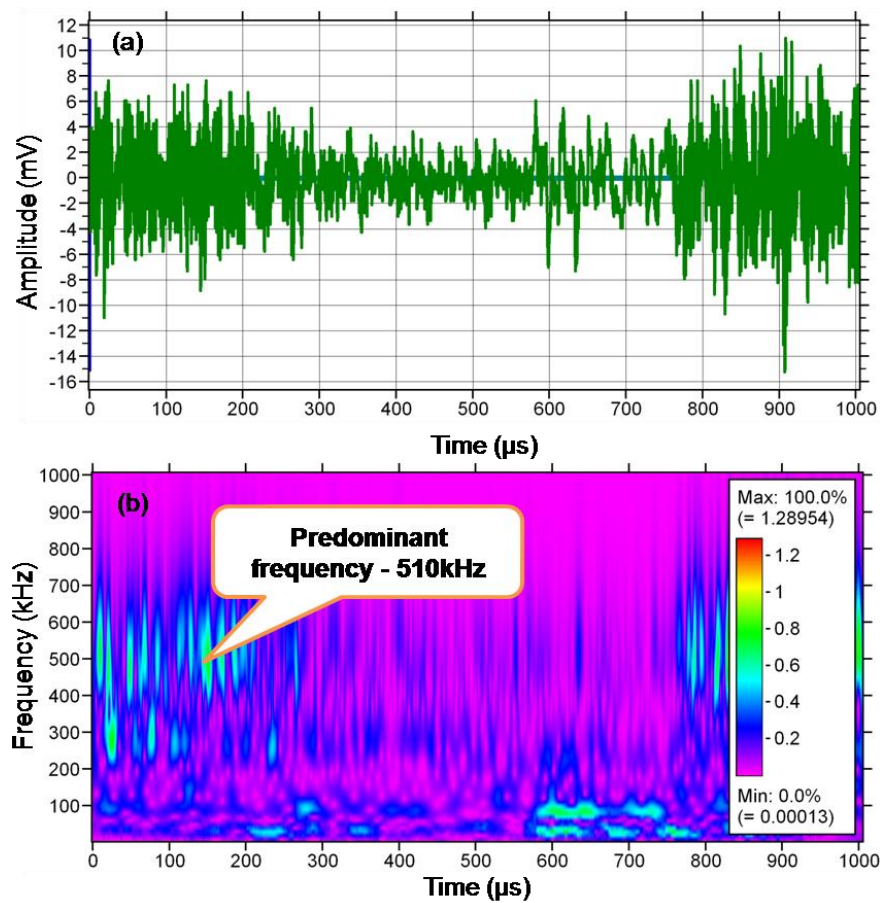


Figure 3. 6 Time-frequency spectrum of AE signals for 900 rpm spindle speed and point angle 118° (a) AE waveform and (b) CWT spectrum.

From the CWT results, it can be understood that at a constant feed rate and with the increase in spindle speed and point angle, continuous type signals become dominant over burst type signals. The reason is the enhanced friction in preference to other sources of AE. However, the CWT does not give the details of higher frequency components and the presence of source mechanisms in AE signals. Hence, the wavelet packet transform was employed to further understand the high-frequency component distribution in AE signals and the associated source mechanisms.

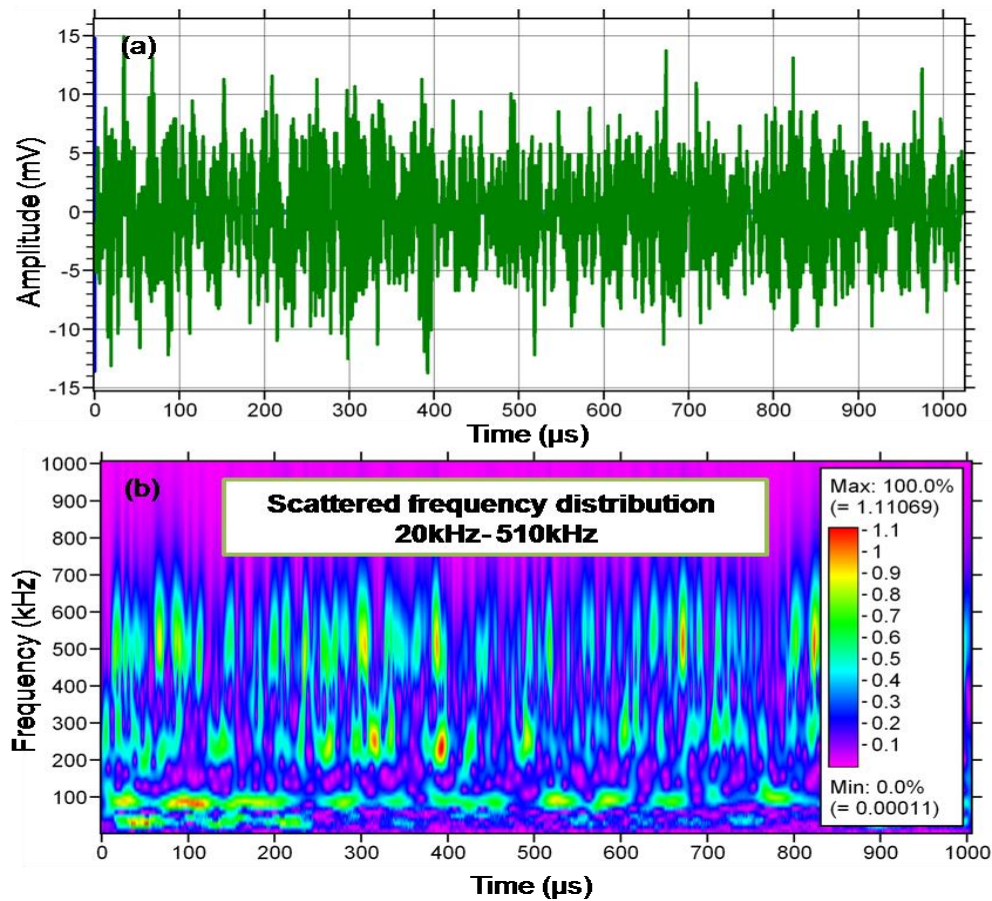


Figure 3. 7 Time-frequency spectrum of AE signals for 1200 rpm spindle speed and point angle 135° (a) AE waveform and (b) CWT spectrum.

Among the obtained AE waveforms, ten waveforms are merged and plotted the time, frequency and amplitude 3D graph as shown in Fig. 3.8. It reveals that the predominant frequency exists at 227 kHz at 3750 μs. Also, the 3D graph (Fig. 3.8) confirms that the 227 kHz is associated with higher amplitude and may be due to chip collision during drilling process. The high frequency components 507 and 510 kHz at 5000 μs and 6000 μs may be due to the combined effect of chip breaking, tool indentation, and particle fracture during the drilling of MMCs.

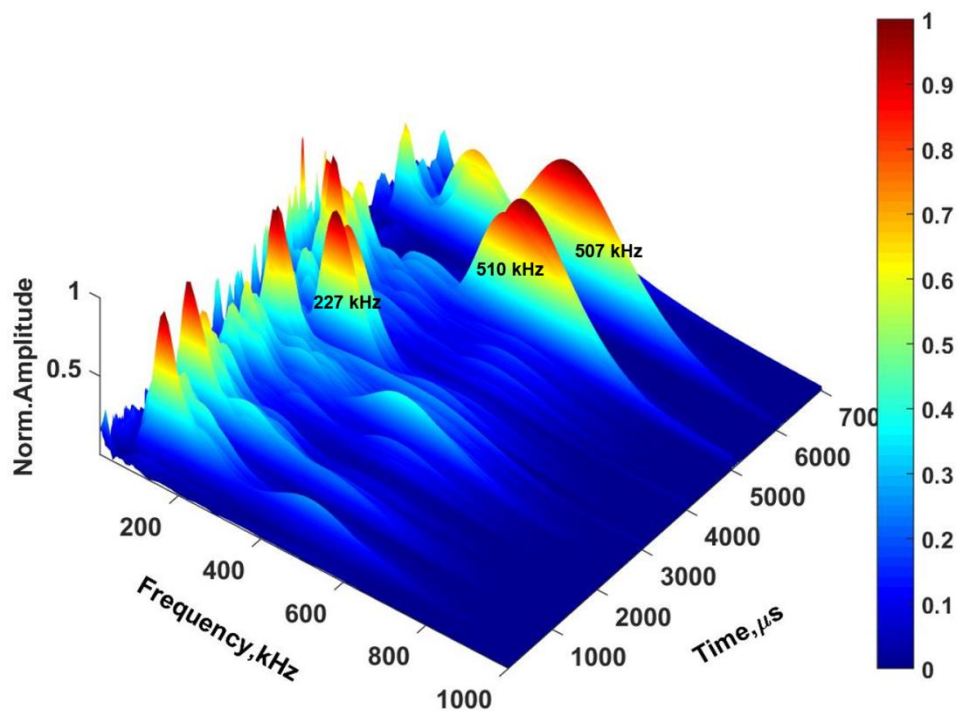


Figure 3. 8 Time-frequency-normalized amplitude spectrum of AE signals for 600 rpm speed and 0.12 mm/rev feed rate.

3.2.4 Wavelet packet analysis

The wavelet packet transform (WPT) approach is implemented to understand the frequency band of AE signals and the related damage mechanisms in the drilling process [68, 94]. In the present study, WPT is implemented to the AE signals and these are decomposed into approximated (low frequency) and detailed (high frequency) components. Further, both the approximated and detail components are decomposed into their own approximated and detailed components, unlike in CWT as discussed in the previous section, where only approximated signals are decomposed. The decomposition is continued upto the user's inevitability.

The entropy criteria and Daubechies mother wavelet forms were used. According to the Nyquist theorem, the sampling frequency should be twice the signal frequency. In the present work, the observed frequency of AE signal is 510 kHz. Therefore, the sampling rate set is 2

MHz. This is in accordance with the previously reported work where a similar procedure was followed for the analysis of AE signals recorded during drilling of glass fiber reinforced composite (GFRP) [98]. The decomposition frequency is selected based on the dominant frequency (510 kHz) existing in the AE signal, which is shown in the FFT spectrum (§ 3.2.2). AE waveforms for the WPT analysis are selected from two-point angle tools, two different cutting conditions (0.07 mm/rev feed rate, 90° point angle and 0.07 mm/rev feed rate, 135° point angle) at 1200 rpm. The above cutting conditions were considered for the WPT analysis because more scattered frequency components are observed in the FFT spectrum. The analysis was carried out only for higher spindle speed (1200 rpm) due to the scattered frequency distribution (Fig. 3.4 (e) and Fig. 3.4 (f)) observed in this condition. The selected first AE waveform (case 1: speed - 1200 rpm, feed rate - 0.07 mm/rev and point angle - 90° is decomposed into eight components with a frequency interval of 62.5 kHz, as shown in Fig. 3.9. The frequency range of the decomposed components varies as follows: (0-62.5), (62.5-125), (125-187.5), (187.5-250), (250-312.5), (312.5-375), (375-437.5), and (437.5-500) kHz. The frequency range and wavelet energy percentage of the decomposed signals are shown in Table 3.3. It is noticed from Table 3.3 that the highest energy percentage (49.59%) is present in the D_1 component with frequency range (0-62.5 kHz), which is related to environmental noise and friction between the tool and the workpiece. The results are in good agreement with the earlier reported work [94]. The second highest wavelet energy percentage (43.02%) is D_2 , and its frequency range (62.5-125 kHz) is associated with matrix cracking.

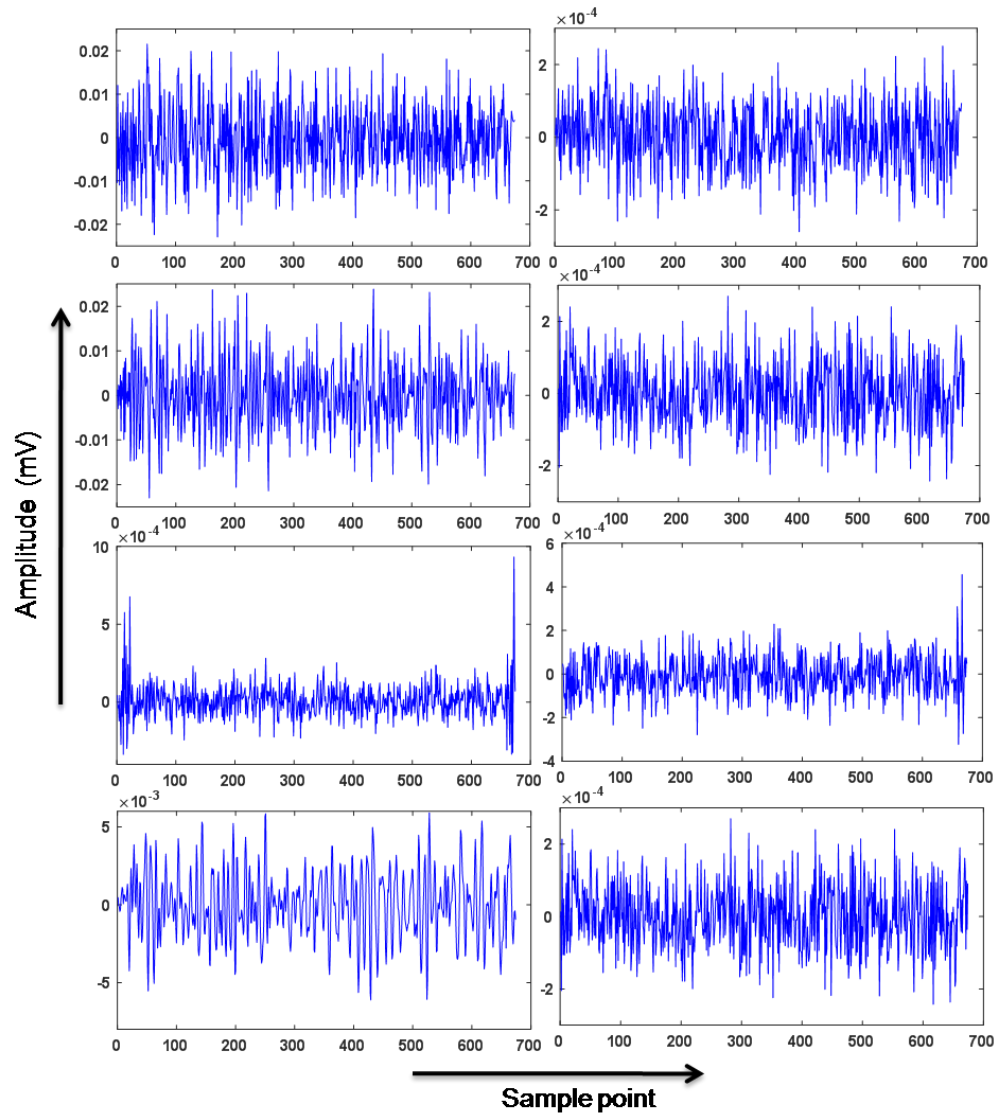


Figure 3. 9 The three level WPT decomposition of AE signal (case1).

These two wavelet components (D_1 and D_2) reveal that friction and matrix cracking are dominant sources of AE in the drilling of MMC at 1200 rpm speed. The obtained low-frequency band is inherently related to abrasive wear in the cutting tool (90° point angle) due to intensive friction between the tool and workpiece. The abrasive wear in the cutting tool with a 90° point angle was confirmed by SEM examination and is shown in the upcoming § 3.3.3. The third highest energy percentage (7.33%) component is D_4 , which is associated with 187.5-250 kHz frequency. The possible source is the plastic deformation of the workpiece material and is in good agreement with an earlier reported work [128].

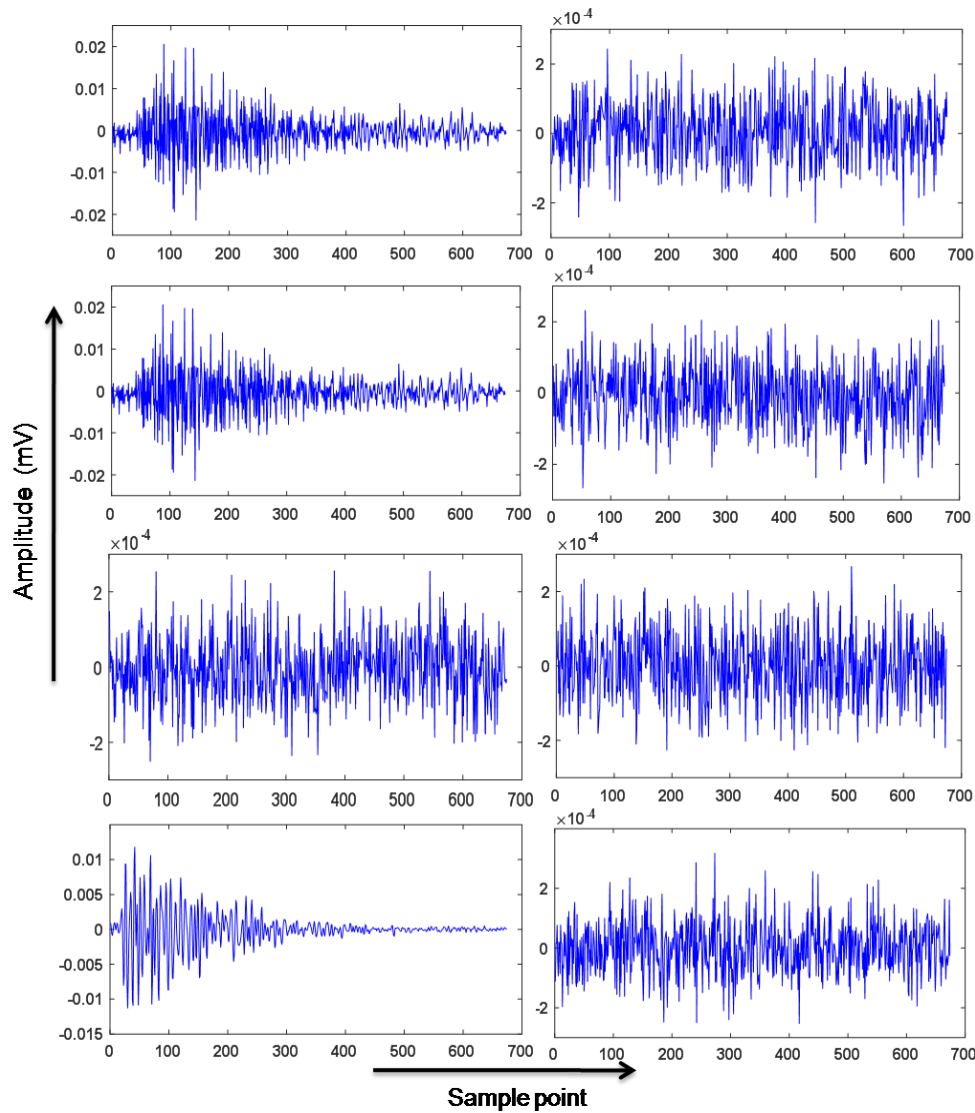


Figure 3. 10 The three level WPT decomposition of AE signal (case 2).

The second AE waveform (case 2: 1200 rpm spindle speed, 0.07 mm/rev feed rate, and 135° point angle) was also decomposed into eight components, as shown in Fig. 3.10. The wavelet energy percentage was calculated for the decomposed waveform and tabulated (Table 3.2). The maximum wavelet energy percentage of 83.45% is observed in the D₂ component, and the related frequency range is 62.5-125 kHz. This is due to dominance in matrix cracking compared to other AE sources for the higher point angle (135°). The wide angle is the reason for dominant matrix cracking in the 135° point angle tool. The second highest energy

percentage (12.66%) is the D₁ component, and its corresponding frequency range is 0-62.5 kHz, which is related to noise + friction.

Table 3. 3 Wavelet energy and frequency components of decomposed signals.

Analysis features	WPT decomposed components							
	D ₁	D ₂	D ₃	D ₄	D ₅	D ₆	D ₇	D ₈
Frequency range (kHz)	0-62.5	62.5-125	125-187.5	187.5-250	250-312.5	312.5-375	375-437.5	437.5-500
Energy percentage for AE waveform for case 1	49.59	43.02	0.01	7.33	0.006	0.008	0.006	0.008
Energy percentage for AE waveform for case 2	12.66	83.45	0.004	3.82	0.0047	0.0046	0.0053	0.0048

The third energy percentage (3.82%) is observed for D₄ for the frequency range of 187.5-250 kHz and is associated with plastic deformation. Thus, at 1200 rpm spindle speed, matrix cracking is dominant (D₂ is 83.45%) for the higher point angle tool (135°), whereas friction dominates (D₁ is 49.59%) for the lower point angle tool (90°). The observed dominant source of friction for lower point angle tool leads to increase in tool wear than higher point angle, which is also confirmed by SEM (§ 3.3.3).

Friction and tensile tests were carried to confirm the physical mechanisms such as friction and matrix crack and their corresponding frequency components. The continuous signals are generated during friction tests and the frequency components range from 60 kHz to 160 kHz

as shown in Fig. 3.11 whereas the burst and continuous types of AE signal were observed for matrix crack as shown in Fig. 3.12. The 110 kHz frequency component was observed from the matrix crack test (tensile test).

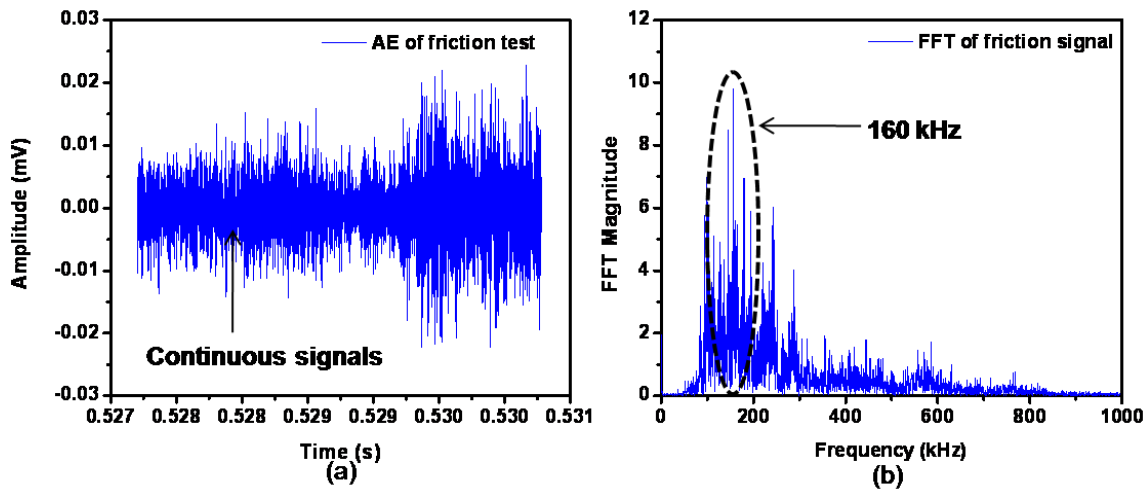


Figure 3. 11 Frequency domain analysis of AE signal for friction test.

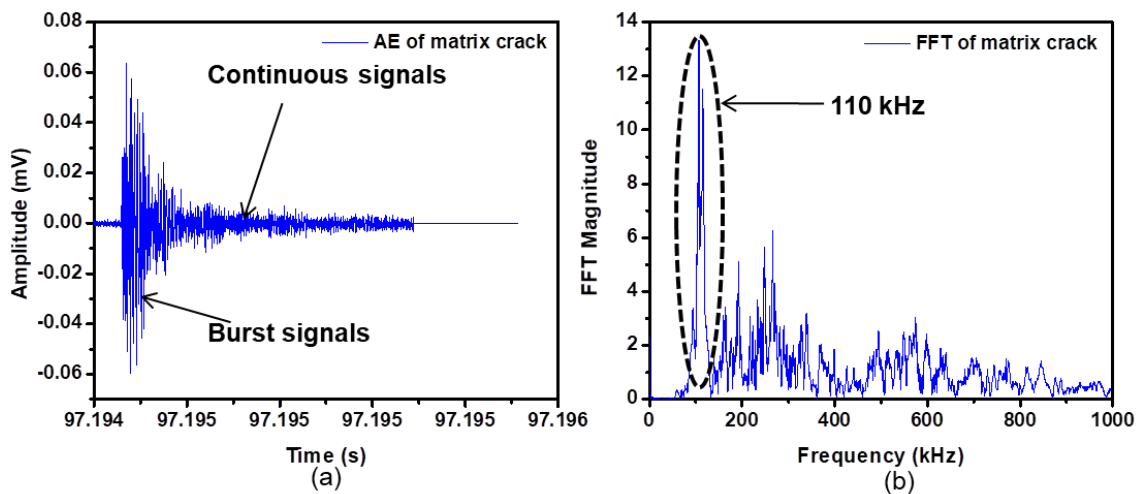


Figure 3. 12 Frequency domain analysis of AE signal for matrix crack test.

3.2.5 Tool wear detection and correlation with AE features

Tool wear was estimated by mapping the damaged area in the cutting tool using a vision measuring microscope after completion of all the drill tests. The tool wear was measured after three drill holes for each point angle, and the cumulative damage was obtained. Figures

3.13 (a) - 3.13 (d) show the optical images of tools for three different point angles (90° , 118° , and 135°). Figures 3.13 (a) and 3.13 (b) reveal intense tool damage and deformed flank surface in the 90° point angle tool due to narrow tool geometry, which provokes high friction between the tool and workpiece. As shown in Fig. 3.13 (c), non-uniform tool edge wear occurs in the flank face of the 118° point angle tool. It is attributed to high speed and high contact pressure in the edge, and this observation is in line with the earlier work reported by Taskesen et al. [110].

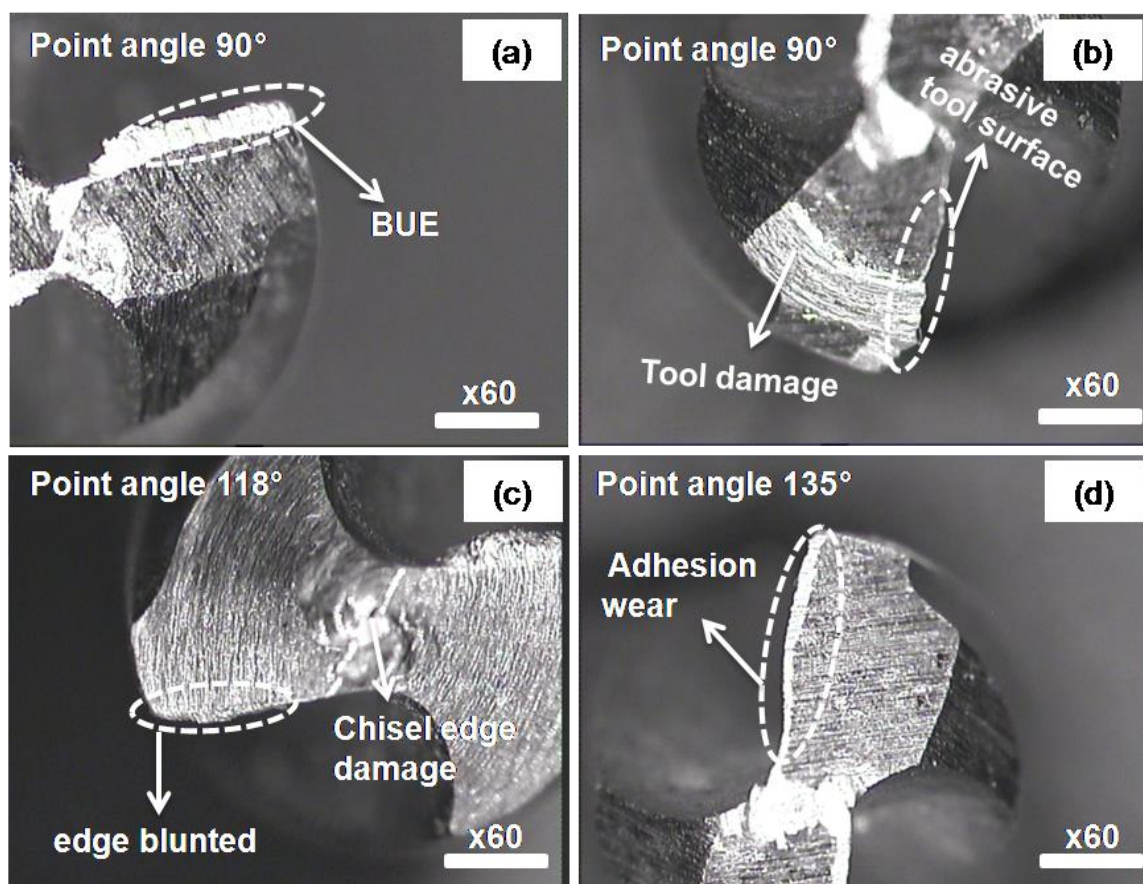


Figure 3. 13 Optical images of the cutting tool: (a) build-up edge (BUE) on the flank face (point angle 90°), (b) tool damage and abrasive wear (point angle 90°), (c) blunted edge in point angle 118° , and (d) adhesion wear in point angle 135° .

The point angle 135° tool reveals adhesion wear on the flank surface and is shown in Fig. 3.13 (d). It is observed that a large amount of Al matrix is deposited on the flank face and

chisel edge of the tool. A large amount of matrix particle deposition on the cutting surface is called a build-up edge (BUE) and is due to low spindle speed and high feed rate. Moreover, the evacuated chips slide on the rake face of the tool during drilling and also form BUE due to severe friction/collision of chips.

The measured tool wear value for different point angles (90° , 118° , and 135°) and the associated average cumulative energy and average wavelet coefficient, are shown in Fig. 3.14(a) and Fig. 3.14(b) respectively. It is observed from Fig. 3.14(a) and 3.14(b) that the average cumulative energy, wavelet coefficient, and tool wear decrease with an increase in point angle. The maximum values of tool wear (2.5 mm^2), average cumulative energy (4.8×10^5), and wavelet coefficient (5.88) are observed for the 90° point angle tool due to dominant kinetic friction, which generates high AE signals in the drilling tests. The increased formation of BUE on the cutting tool surface and decrease in friction between the tool and workpiece lead to the decrease in tool wear (0.3 mm^2 and 0.1 mm^2), cumulative AE energy (4.1×10^5 and 4×10^5) and wavelet coefficient (5.44 and 1.55) for higher point angles (118° and 135°). The observed result of the decrease in tool wear and cumulative AE energy with an increase in point angle is in agreement with earlier reported results [96]. However, an increase in point angle increases chip evacuation and matrix crack propagation. Therefore, it becomes clear that the generation of AE signal during drilling of the MMC is highly dependent on tool type and its characteristics.

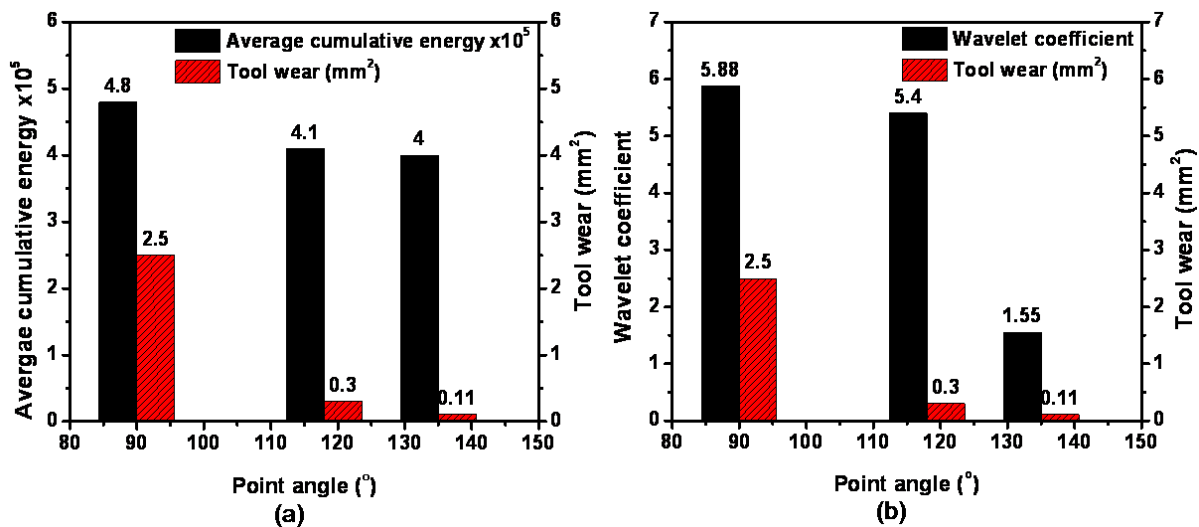


Figure 3. 14 Correlation of AE signal parameters and tool wear for different point angle tools: 90°, 118° and 135°, (a) average cumulative energy and tool wear vs point angle (b) wavelet coefficient and tool wear vs point angle.

In addition to average cumulative energy and wavelet coefficient, tool wear value was also correlated with frequency of AE signals. The dominant frequency of AE signals as discussed in section 3.2.2 is found to lie between 100 kHz and 510 kHz. The earlier reported research shows that high frequency components above 150 kHz are insignificant to tool wear [85]. Therefore, the FFT spectrum below 150 kHz was considered to correlate with tool wear. Figure 3.15 reveals the variation of AE frequency and amplitude with tool wear for a 90° point angle tool.

The 3D graph (Fig. 3.15) shows that AE amplitude decreases with increase in tool wear. The tool wear value of 1.2 mm^2 is associated with higher amplitude signals (410 mV) for the initial drill hole because the fresh drill bit is subjected to severe friction and causes abrasive damage on the flank surface. Increase in the value of tool wear up to 2.1 mm^2 progressive wear results in AE signal amplitude of 102 mV. The greater abrasive wear (2.5 mm^2) and lowest amplitude (62 mV) was noted due to higher friction. It is understood that the signal amplitude decreases with progressive wear for 90° point angle tool. The lowest amplitude is

due to rubbing action between flank face and the workpiece instead of only progressive abrasive wear in the flank face. The results are similar to that reported in Al- 20%SiC composite during friction stir welding process [85].

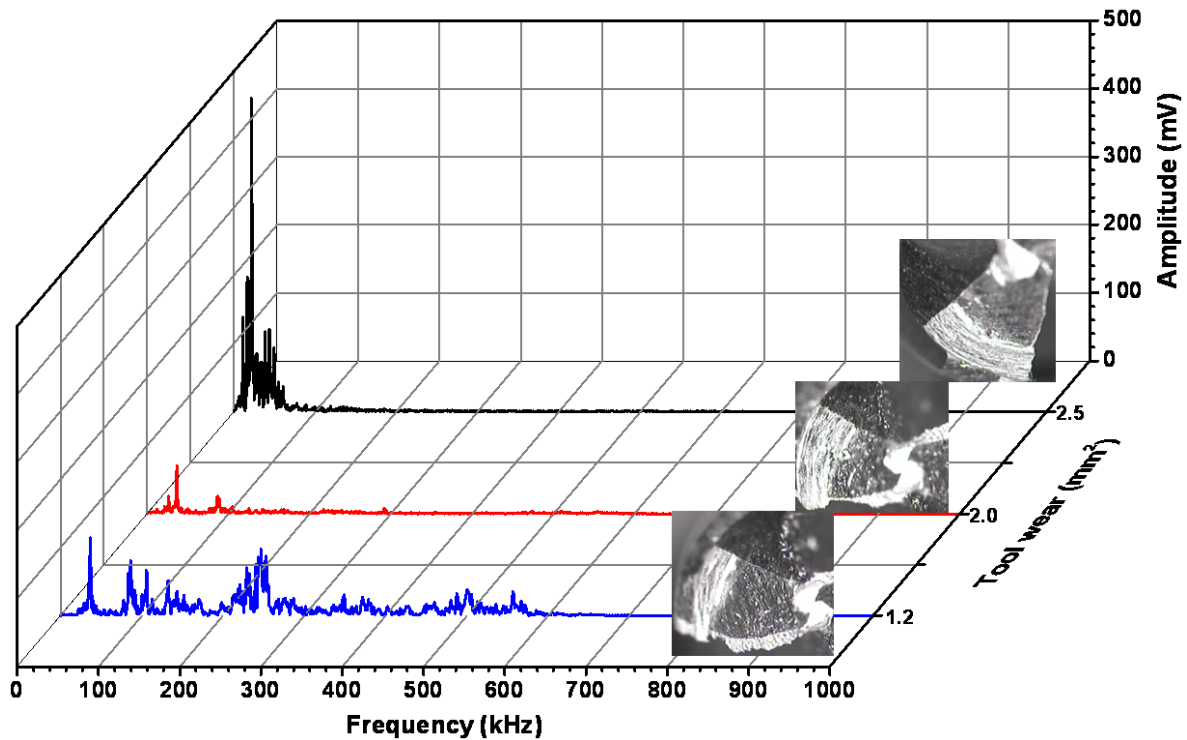


Figure 3. 15 The variation of frequency and amplitude with tool wear for 90° point angle tool.

3.3 Temperature rise during drilling of Al-5%SiC composite

The tool temperature rises were recorded as thermal images using infrared thermography. The box contour was used to analyze temperature rise in the cutting tool. The maximum tool temperature rises with cutting time for drilling at 1200 rpm spindle speed, 0.12 mm/rev feed rate and 90° point angle is shown in Fig. 3.16 (a). The illustration shows an oscillatory pattern of temperature profile due to continuous rotation of the cutting tool and chip evacuation during the drilling process. The oscillatory pattern of the temperature profile is in good agreement with the earlier work reported by Saez-de-Buruaga [103]. Figure 3.16 (a) shows that tool temperature increased upto some specific time and almost stabilized and then

increased again to the maximum temperature (93 °C) due to back-wall fracture of the workpiece. The temperature falls after the tool exits from the workpiece.

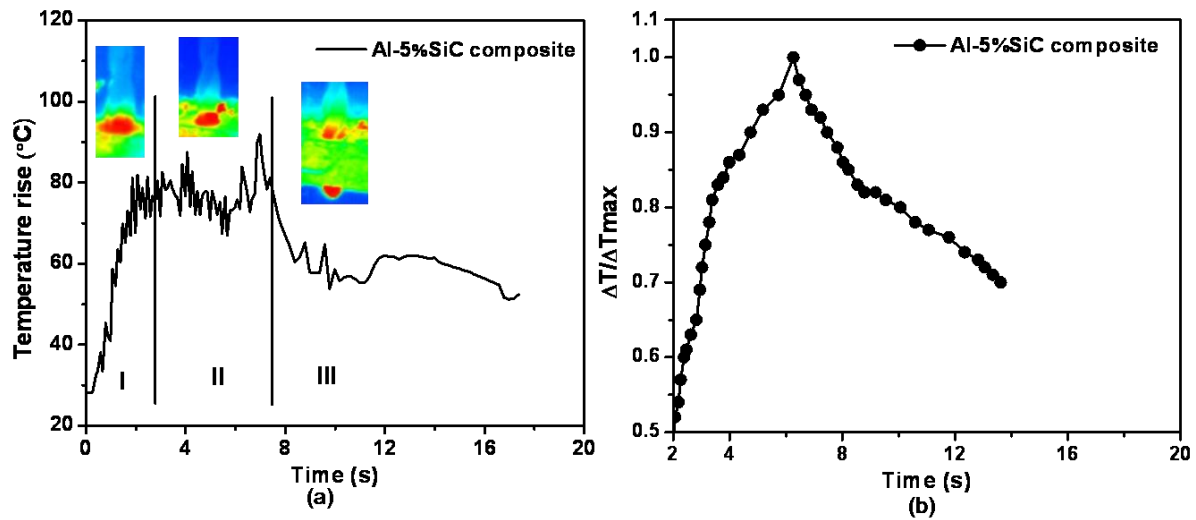


Figure 3. 16 (a) Variation of temperature rise with time for drilling at 1200 rpm spindle speed and 0.12 mm/rev feed rate for point angle 90°, and (b) normalized temperature.

Further, based on the temperature line profile, the drilling process could be divided into three stages. Stage I is known as tool entry stage (pre-drilling + indentation). In this stage, the cutting tool rotates with high speed (rpm) and moves in the Z-direction with a particular feed rate. Once the drill bit contacts the workpiece, the chisel edges start to rub with the surface of the workpiece and initiate the cutting process with the removal of chips. Low tool temperature is (smooth line) observed in Fig. 3.16 (a) before the cutting process starts. But, once drill bit edges begin to extrude the workpiece, temperature increases with an unprecedented rate from ambient temperature to 81°C.

Rigorous cutting zone (upto maximum temperature) is called stage II, where severe cutting takes place after indentation (stage I). A considerable amount of chips is discharged in stage II because of the complete interaction of drill lips with the workpiece. In this stage, maximum tool temperature of 93 °C was noted. This is due to the occurrence of shear deformation, matrix cracking, and kinetic friction between the tool and workpiece. The breakage of SiC

particles also contributes to heat generation. The cutting stage is followed by tool exit (stage III), wherein the temperature drops down to 28 °C due to tool exit from the workpiece. These results are concurrent with the results reported by Choudhury et al. [129]. In their study, the drilling of lignocellulosic fiber-reinforced laminate was classified into various stages. Figure 3.16 (b) shows the variation of normalized tool temperature with cutting time. The normalized temperature was calculated from the ratio of the rise in temperature (ΔT) to the maximum increase in temperature (ΔT_{\max}) over the time period during drilling. The obtained results confirm that the maximum temperature lies in the cutting zone (II).

In addition, thermal images were extracted from different stages of the drilling process, as shown in Figs. 3.17 (a) - 3.17 (c). The temperature rise for each stage is mentioned at the bottom of the thermal images. The thermogram mapping clearly differentiates three different stages of the drilling process.

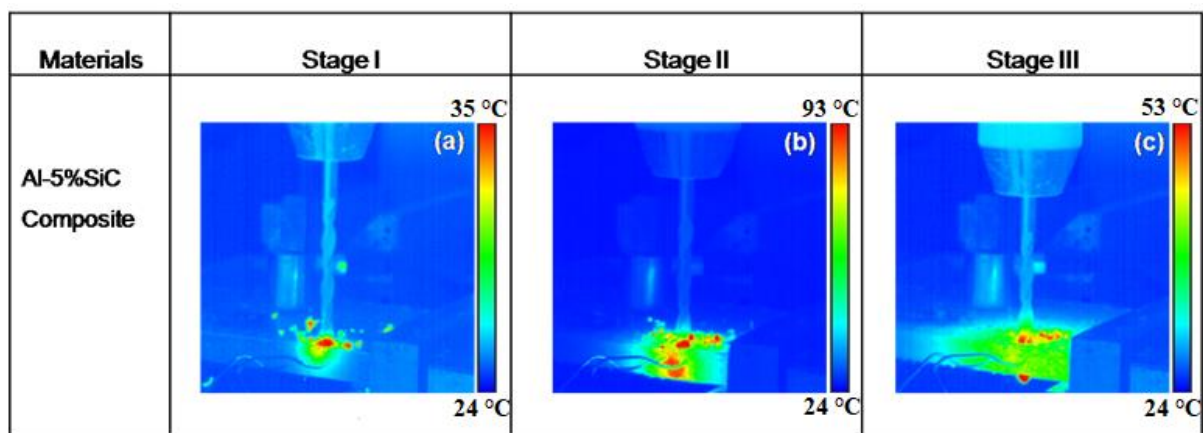


Figure 3. 17 Thermal images of the tool during drilling (a) stage I, (b) stage II, and (c) stage III.

3.3.1 Tool and workpiece temperatures

The maximum temperature rise in the cutting tool was measured instantly after the back-wall fracture of the workpiece when the tool comes out (i.e., tool exit) from the workpiece. Figures 3.18 (a) and 3.18 (b) show the variation of average tool temperature and workpiece

temperature, respectively as a function of spindle speed for different point angles. The average cutting tool temperature increases with an increase in spindle speed for different point angles due to high frictional contact between the tool and workpiece [104]. Moreover, the 90° point angle tool shows maximum temperature rise due to a lower point angle, which leads to maximum friction between the tool and workpiece. The temperature rises for the 135° point angle tool shows the second highest temperature due to high contact surface area [130]. The lowest temperature rise was observed for the 118° point angle tool due to proper chip formation and evacuation in the drilling process by this tool.

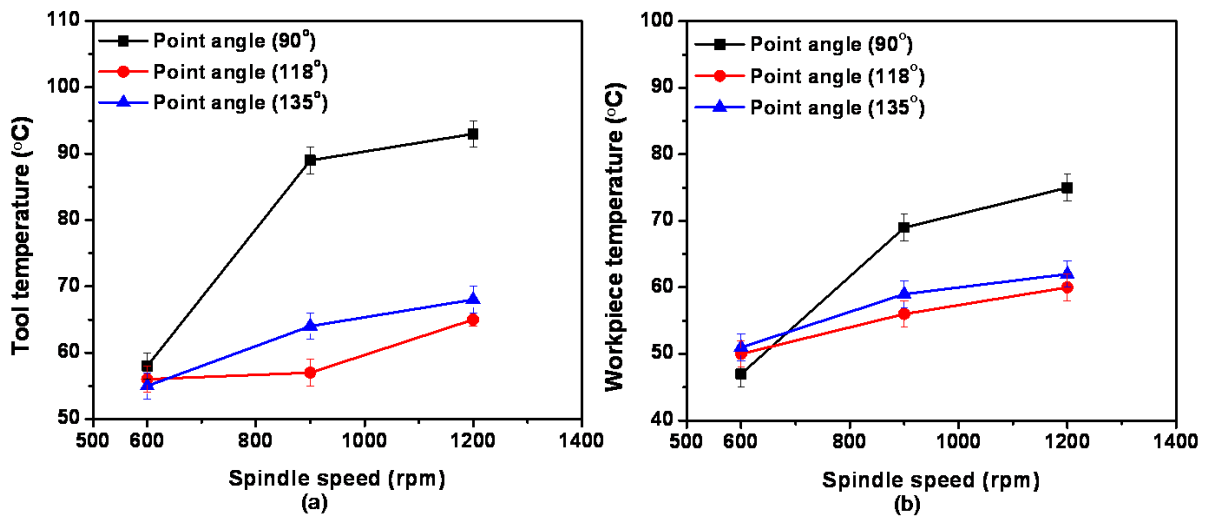


Figure 3.18 Variation of tool temperature and workpiece temperature with spindle speed for different point angles (a) tool temperature vs spindle speed, and (b) workpiece temperature vs spindle speed.

The heat generated in the drilling process is mainly due to primary and secondary shear deformation in the composite material and friction between the tool and the workpiece. The generated heat is distributed to the workpiece, chips, and cutting tool. Figure 3.18 (b) depicts the maximum temperature rise in the workpiece for each drill hole for different cutting speeds and point angles. The average workpiece temperature increases with an increase in spindle speed for different point angles. The maximum workpiece temperature (76 °C) was observed

for drilling by the 90° point angle tool as compared to other point angle tools (118° and 135°). The lowest temperature was noted for drilling by the 118° point angle tool. The reason is the point angle 90° tool encounters high friction and undeformed chip thickness as compared to 118° point angle tool. The measured workpiece temperature is lower than the tool temperature because heat generated during drilling is transferred to chips and cutting tool [130].

3.3.2 Undeformed chip thickness calculation

The undeformed chip thickness can be determined from equation 3.1. In drilling process, point angle 90° tool encounters high friction and greater undeformed chip thickness when compared to point angle 118° tool due to narrow edges of the cutting tool (90° tool). Therefore, the lower point angle (90°) tool generates higher tool temperature than the 118° point angle tool. The schematic of undeformed chip thickness in the drilling process is shown in Fig. 3.19.

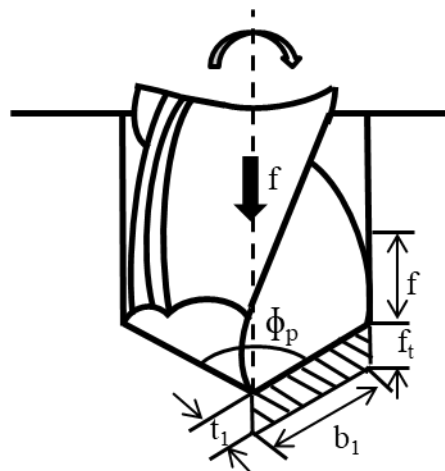


Figure 3. 19 Schematic of undeformed chip thickness in the drilling process [22]

$$t_1 = \frac{f}{z} \sin\left(\frac{\phi_p}{2}\right) \quad (3.1)$$

t_1 -Undeformed chip thickness

f -Feed rate

z - Number of cutting teeth

ϕ_p -Point angle

3.3.3 Numerical simulation of workpiece temperature

A COMSOL Multiphysics model was established on the basis of the experimental data. The model was executed to predict heat distribution in the workpiece during the drilling process. The experimentally obtained workpiece temperature was correlated with the simulated results. The following equation (3.2) was used to simulate the workpiece temperature (T) at any given time.

$$\rho c_p \frac{\partial T}{\partial t} = \nabla(k \nabla T) \quad (3.2)$$

Where ρ , C_p and k represent density, specific heat capacity and thermal conductivity of the composite material, respectively. The left side term in Eqn. 3.2 represents thermal inertia of the system, and the right-side term shows heat conduction in the material. The values of density and specific heat capacity of the workpiece were calculated from the individual constituents present in the composite. A time dependent, two-dimensional, the axisymmetric domain was used for the simulation. The geometry of the workpiece was discretized with a mesh component of 1915 triangular elements, denser near the tool cutting edge. The thermal properties of the workpiece material and the cutting tool are given in Table 3.4. According to ASTM standards, the properties belonging to the composite material were determined while Matweb was used for the M2 HSS tool material. ASTM D792 was considered for density measurement of the composite material. The calculation of specific heat capacity and thermal conductivity of the workpiece are calculated as per the following equations (3.3) and (3.4) [131].

$$\text{Specific heat can be computed as: } C_{p,c} = V_r \rho_r C_{p,r} + V_f \rho_f C_{p,f} / \rho_c \quad (3.3)$$

$C_{p,c}$ - Specific heat capacity of the composite

$$\text{Thermal conductivity can be computed as } k_{p,c} = V_r \rho_r C_{p,r} + V_f \rho_f C_{p,f} / \rho_c \quad (3.4)$$

$k_{p,c}$ - Thermal conductivity of the composite

ρ_r - Density of reinforcement, ρ_f - Density of fiber

ρ_c - Density of composite, $C_{p,f}$ - Specific heat of fiber

$C_{p,r}$ - Specific heat capacity of reinforcement

V_f - Volume fraction of fiber

V_r - Volume fraction of reinforcement

A convective thermal flux was imposed on the surface of the drill bit and workpiece. For this, a convective coefficient of 10 W/m²K and an air temperature equal to 20 °C were considered. The thermal insulation was fixed on the remaining contours because temperature measurement is at contact side of the thermal camera to the cutting tool and it is not measure of other side of tool temperature. Therefore, it was considered to insulate the remaining contour. The mesh along with the boundary conditions for the model, are shown in Fig. 3.20. For the simulation, maximum tool tip temperature of 93 °C and tool surface temperature of 84 °C obtained from IR thermography at point angle 90°, spindle speed 1200 rpm, 0.12 mm/rev feed rate were considered. The obtained temperature data was imposed on the tool to workpiece interface as a heat source.

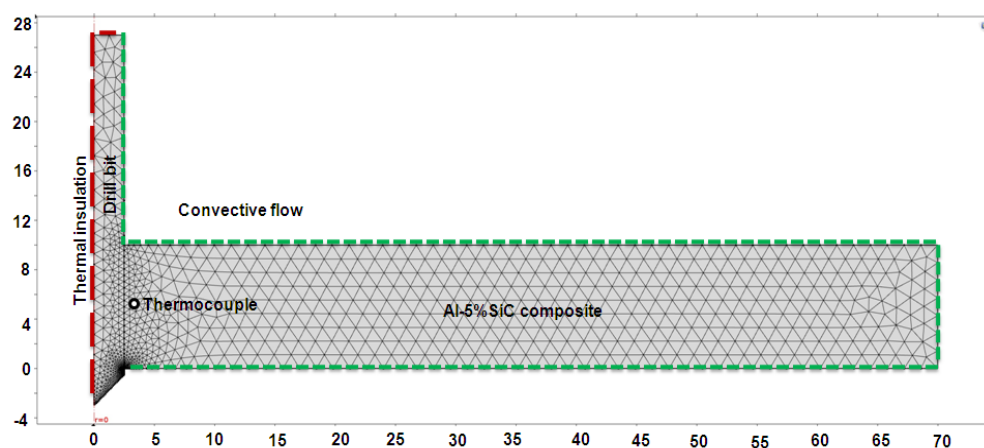


Figure 3. 20 Mesh and boundary conditions for the model.

The workpiece temperature was measured with a K-type thermocouple embedded at 2 mm distance from the drilled hole surface. Figure 3.21 shows the thermal field distribution in the workpiece and this is correlated with the experimentally obtained workpiece temperature. The thermal field (Fig. 3.21) reveals that the simulated temperature (73.2 °C) by COMSOL model is very close to the obtained workpiece temperature (76 °C).

Table 3. 4 Material properties used for the numerical simulation.

Property	Al-5%SiC composite	HSS drill bit
Thermal conductivity [W/mK]	180	41.5
Density [kg/m ³]	2740	8138
Heat capacity [J/kg.K]	741	460

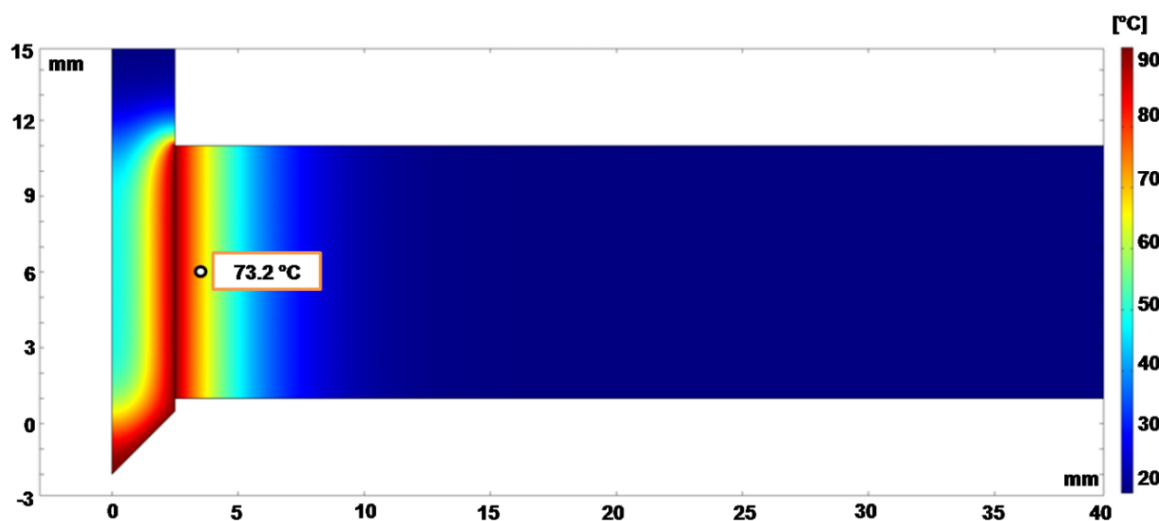


Figure 3. 21 Simulated temperature distribution in the workpiece at 2 mm distance from drilled hole.

3.3.4 Tool wear detection and corresponding tool temperature

Scanning electron microscope (SEM) studies were carried out for better understanding the mechanism of tool wear during drilling of MMC. Figures 3.22 (a) - 3.22 (d) show different types of wear that are formed on the 90° point angle tool, i.e., abrasive wear, grooves, and

build-up edge on chisel face. The 90° point angle tool encounters higher friction and thrust force in the cutting edges because of its tapered shape. This leads to abrasive wear in the flank face of the 90° point angle tool as shown in Fig. 3.22 (a). SEM images reveal a lot of grooves on the flank surface due to cutting tool abrasion with silicon carbide particulates in the workpiece and are in good agreement with earlier reported results for drilling of Al/Al₂O₃ MMC [98]. The SEM image is shown in Fig. 3.22 (b) describes that the tool edge is deformed from cutting surface to outer surface because the tool edge surface experiences high pressure along with friction at a greater speed and feed rate. Figures. 3.22 (c) - 3.22 (d) illustrate that the Al alloy matrix gets deposited on the flank face of the cutting tool and forms a build-up edge on the cutting edge due to lower cutting speed and higher feed rate.

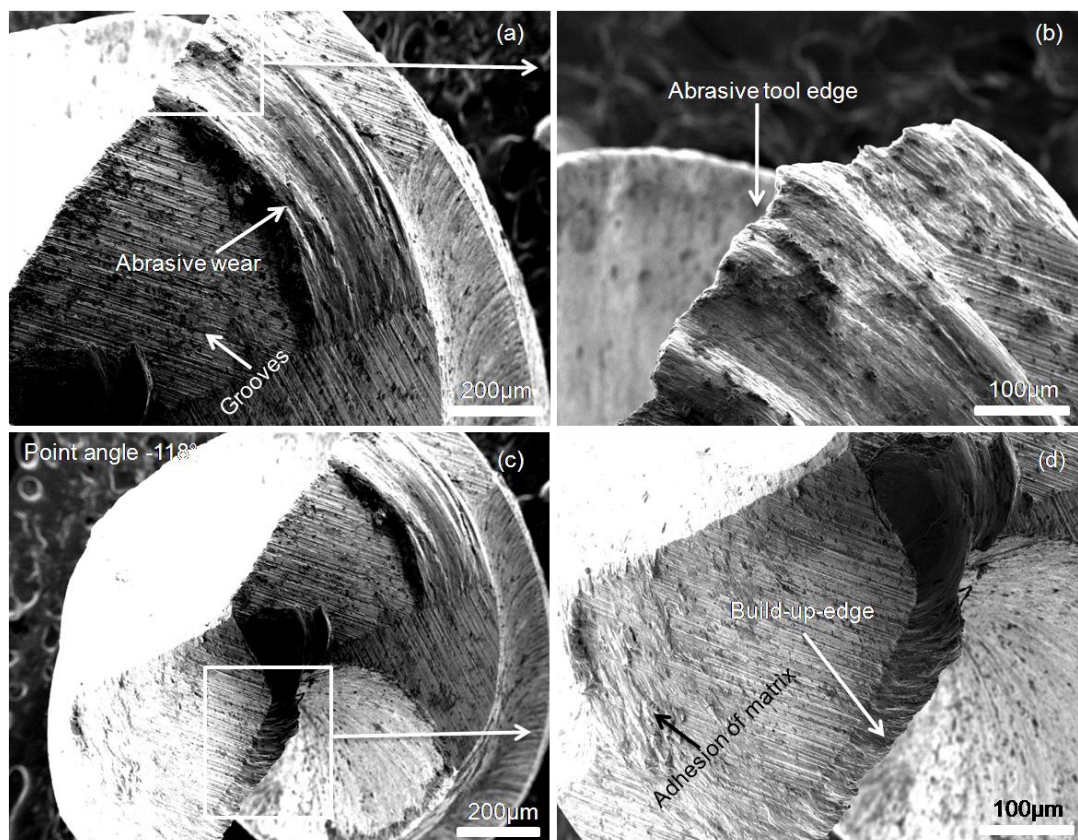


Figure 3. 22 SEM images of 90° point angle tool (a) abrasive wear, (b) deformed tool surface, (c) build-up-edge (BUE), and (d) adhesion of matrix.

SEM images of 118° and 135° point angle tools are shown in Figs. 3.23 (a) - 3.23 (d). From Figs. 3.23 (a) - 3.23 (d), it is observed that various types of wear such as adhesion wear, build-up edge, adhesion of chips, and edge blunt are formed on tool surface for 118° and 135° point angle tools. The build-up edge accumulated on the chisel edge as well as cutting edge is due to lower speed and feed rate. Also, Al debris and adhesion of chips are observed on the flank face, as shown in Figs. 3.23 (a) and 3.23 (b). The SEM images of the 135° point angle (Figs. 3.23 c and 3.23d) tool reveal the formation of build-up edge on the chisel edge, and this is due to low pressure and force at the chisel edge as compared to the tool edge. Adhesion of Al matrix is less in the cutting edge as compared to the chisel edge due to large tool contact surface area between the tool and workpiece.

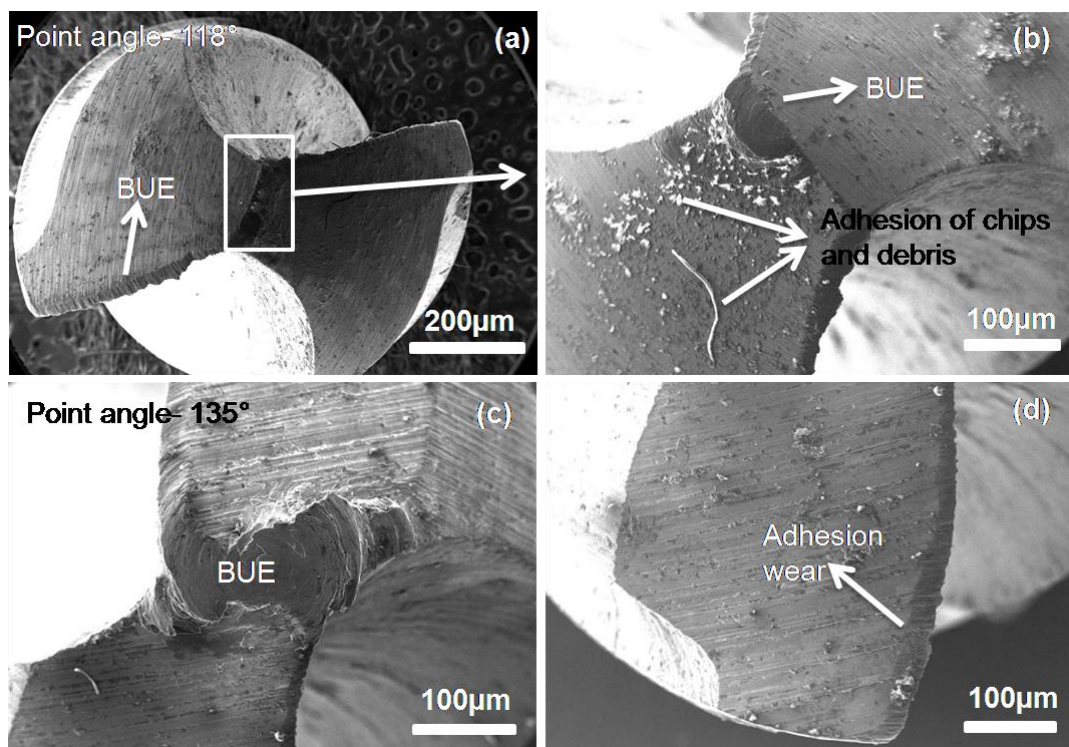


Figure 3. 23 SEM images of 118° and 135° point angle tools (a) BUE, (b) adhesion of chips on flank space in 118° point angle drill bit, (c) BUE formation on chisel edge of 135° point angle tool, and (d) adhesion wear on 135° point angle tool.

The tool wear was correlated with tool temperature. The tool wear was measured after every three drill holes for each point angle, and the cumulative damage was obtained. The cumulative tool damage and the associated maximum tool temperature rise are plotted as a function of point angle and are shown in Fig. 3.24. It is evident from Fig. 3.24 that the lower point angle (90°) tool is subjected to severe tool damage (2.5 mm^2), and this is due to sharp tapered edges of the drill bit and the corresponding average tool temperature is 93°C . The area of tool damage is 0.3 mm^2 for the point angle 118° tool, and the resultant tool temperature is 66°C . The tool temperature decreases for the 118° point angle tool compared to the point angle 90° because of less friction between the 118° tool and workpiece and limited interruption of chips. The tool wear value of 0.11 mm^2 was observed for the point angle 135° because of the formation of build-up edge on cutting surface as well as on chisel edge, and the equivalent measured tool temperature is 56°C . The correlation of tool temperature with tool wear shows that higher tool temperature is associated with higher tool wear, and vice versa, and this observation is in line with the earlier published works [98, 101].

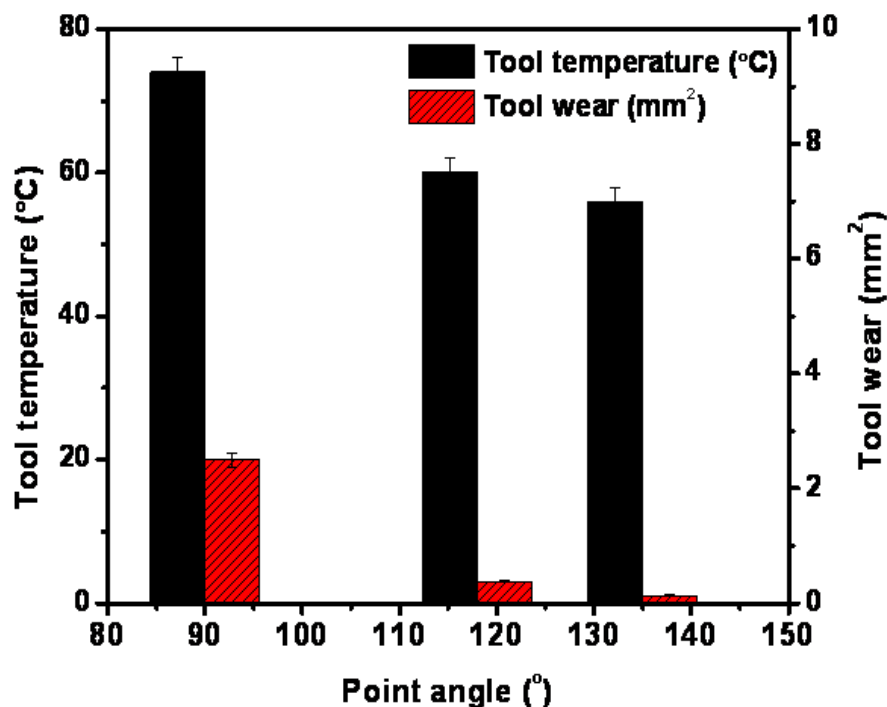


Figure 3. 24 Tool wear and tool temperature for three different point angle.

3.4 Analysis of variance (ANOVA) for identification of significant cutting parameters

The analysis of variance (ANOVA) is mainly used to interpret the experimental data and make necessary decision about the effect of experimental parameters (speed, feed rate, and point angle) on quality characteristics such as tool temperature and surface roughness of the workpiece. To identify the most influential cutting factors for the output responses, the percent contribution ratio (PCR) of these parameters is analyzed. The percent contribution ratio is calculated from equation (3.5).

$$PCR = \frac{SS_A - (V_e)(DOF)}{SS_T} \times 100 \quad (3.5)$$

Where SS_A represents the sum of squares of parameter A, ' V_e ' is the variance of error, ' DOF ' is the degree of freedom, and SS_T is the total sum of squares. The machining parameters are evaluated, wherein the values of % probability (P) and F-test correspond to 95% confidence level. The cutting parameters are considered a significant factor in output responses (tool temperature and surface roughness) at the 95% confidence level, since the P-value in the ANOVA for any input is smaller than 0.05. The cutting parameters, P values, and their corresponding significant rates are given in Table 3.4. The percent contribution ratio for tool temperature is analyzed and tabulated (Table 3.4). The values of percent contribution ratio of point angle (42.32%) and spindle speed (37.30%) are most significant for tool temperature. The feed rate does not show any statistically significant effect on tool temperature (18.49%). However, point angle and spindle speed are the most effective parameters for tool temperature for drilling of Al-5%SiC composite. The statistical calculation and percentage of contribution results for surface roughness are shown in Table 3.5. From the analysis of variance, the most significant parameter for surface roughness is feed rate with 77.36% contribution to the total variation. The least influential parameter is point angle, with a percent contribution ratio of 12.85%. From the analysis of variance, it is understood that feed

rate is a dominant influential factor for surface roughness of workpiece and is in good agreement with the previously reported results [132]. The present results suggest that feed rate and point angle have statistical and physical significance on the surface roughness.

Table 3. 5 Analysis of variance (ANOVA) for tool temperature.

Source	DOF	Adj SS	Adj MS	F-Value	P-Value	PCR, (%)
Speed	2	614.89	307.44	19.91	0.048	37.30
Feed	2	304.89	152.44	9.87	0.092	18.49
Point angle	2	697.56	348.78	22.58	0.042	42.32
Error	2	30.89	15.44			1.8
Total	8	1648.22				100

DOF: degrees of freedom, SS: Sum of squares, MS: Mean square, F: F-test value, P: %Probability, PCR: Precent contribution ratio.

Table 3. 6 Analysis of variance (ANOVA) for surface roughness.

Source	DOF	Adj SS	Adj MS	F-Value	P-Value	PCR, (%)
Speed	2	0.4027	0.20134	2.69	0.271	7.13
Feed	2	4.3670	2.18351	29.23	0.033	77.36
Point angle	2	0.7254	0.36268	4.85	0.171	12.85
Error	2	0.1494	0.07471			2.64
Total	8	5.6445				100

DOF: degrees of freedom, SS: Sum of squares, MS: Mean square, F: F-test value, P: %Probability, PCR: Precent contribution ratio.

3.5 Surface quality characterization

Surface roughness (Ra) of the drilled MMC workpiece was measured by using Mitutoyo surftest. The variation of surface roughness with feed rate at different speeds is shown in Fig.

3.25. As can be seen from Fig. 3.25 that the surface roughness decreases with an increase in speed for 0.07 mm/rev feed rate, which is due to an increase in friction coefficient. This result is in good agreement with the earlier published work [132]. However, the highest surface roughness value of 4.2 μm is observed for drilling 0.17 mm/rev feed rate and 1200 rpm speed.

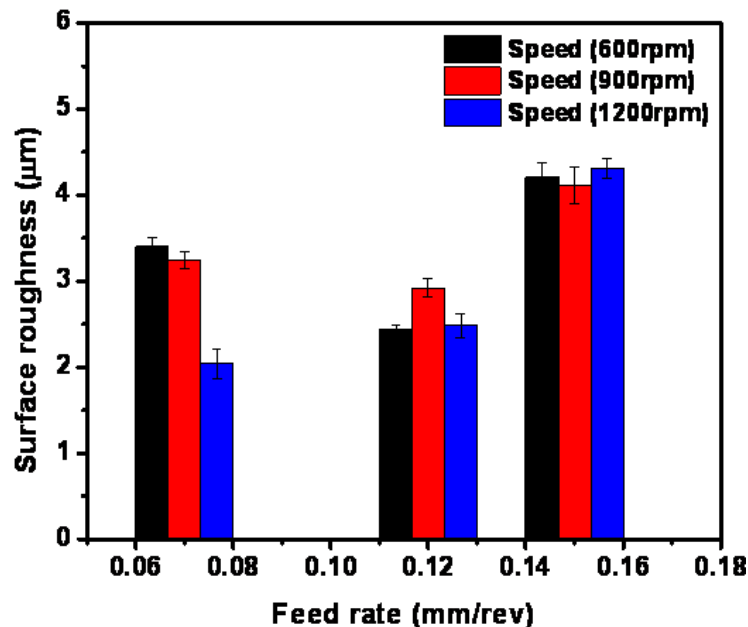


Figure 3. 25 Surface roughness vs feed rate at different speeds for Al-5%SiC composite.

Various damages present in the drilled surface are evaluated using SEM for 0.07 mm/rev feed rate. The damages are evaluated for 900 rpm speed and point angles (90° and 135°), as shown in Figs. 3.26 (a) and (b). For this purpose, the drilled MMC specimen was separated into two parts by using metal-cutting machining after completion of all the tests. The different direction of the scratches is observed in the drilled surface. This is due to the chip collision/rubbing with drilled surface of the workpiece during drilling process. The drilling direction has been given in Fig. 3.26. It is observed from Fig. 3.26 (a) that the scratches are present in the workpiece surface drilled by 90° point angle tool and this is due to weak bonding between SiC particles and Al matrix. The material flow and micro-cracks are present in the workpiece surface drilled by 135° point angle tool. This is due to temperature rise in

the deformation zone and strain hardening of the composite material drilling by 135° point angle tool [133].

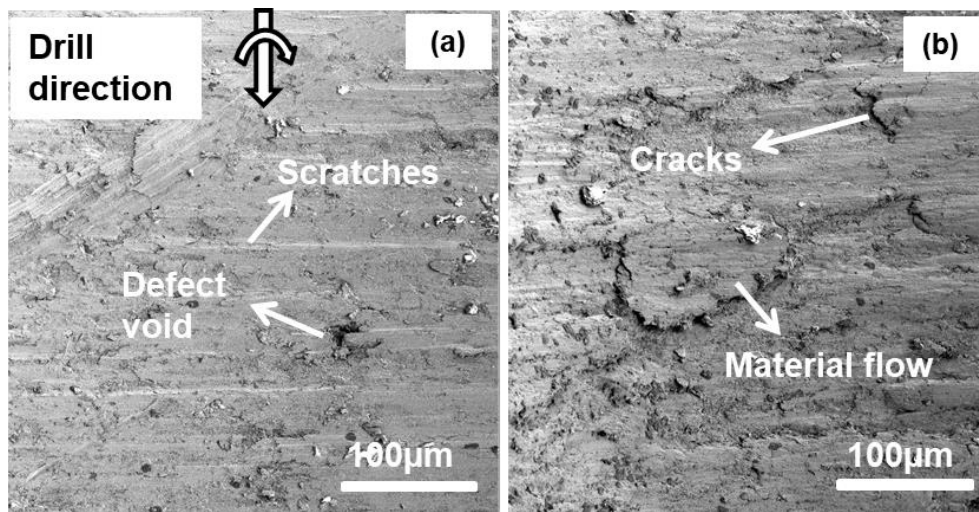


Figure 3. 26 Surface morphology of the machined surface (a) scratches and particle pullout in point angle 90° drilled surface and (b) material flow and cracks at point angle 135° drilled surface.

3.6 Chip formation mechanism

Different types (i.e., broken, comma, helical, conical, saw-tooth and continuous) of chip segmentation are observed for drilling at different speeds (600, 900 and 1200 rpm) and point angles (90°, 118°, and 135°) at constant feed rate (0.07 mm/rev) and are shown in Figs. 3.27 (a) - 3.27 (c). The photograph (Fig. 3.26 a) depicts broken and comma types of chips for cutting at 600 rpm spindle speed and 90° point angle tool at 0.07 mm/rev feed rate. This is due to the occurrence of discontinuous plastic deformation. Saw-tooth and short helical chips (Fig. 3.27 b) are observed for cutting at 900 rpm spindle speed and 118° point angle tool due to increased tool-workpiece temperature leading to plastic deformation in the material.

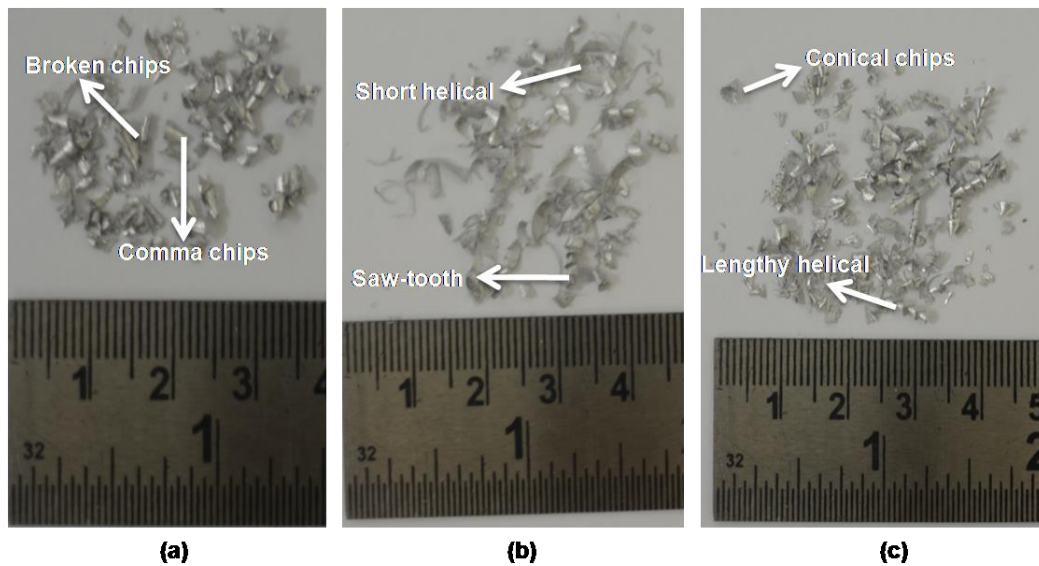


Figure 3. 27 Variation of chip formation at different cutting conditions for constant 0.07mm/rev feed rate: (a) speed 600 rpm and point angle 90°, (b) speed 900 rpm and point angle 118°, and (c) speed 1200 rpm and point angle 135°.

Figure 3.27 (c) illustrates that conical and lengthy helical chips are formed for cutting at 1200 rpm spindle speed and 135° point angle tool due to an increase in strain rate with the increase in the spindle speed. The length of the chip slightly increases with an increase in point angle (90°, 118°, and 135°). The chip formation results are in concurrence with an earlier report [119]. Figures 3.28 (a) - 3.28 (d) show the SEM images of the short conical type of chips and continuous chips. The SEM image reveals that flakes, folding, and voids are present in the short conical chips due to the presence of reinforcement in the Al matrix, which promotes the brittle nature of the composite material [135-136]. Figure 3.28 (d) reveals cracks and saw-tooth behavior in the chip formation due to strain hardening of the workpiece material during drilling. The presence of silicon carbide reinforcement in Al matrix modifies the mechanical properties and microstructure of the Al alloy and also attributes to the different types of chip formation during drilling.

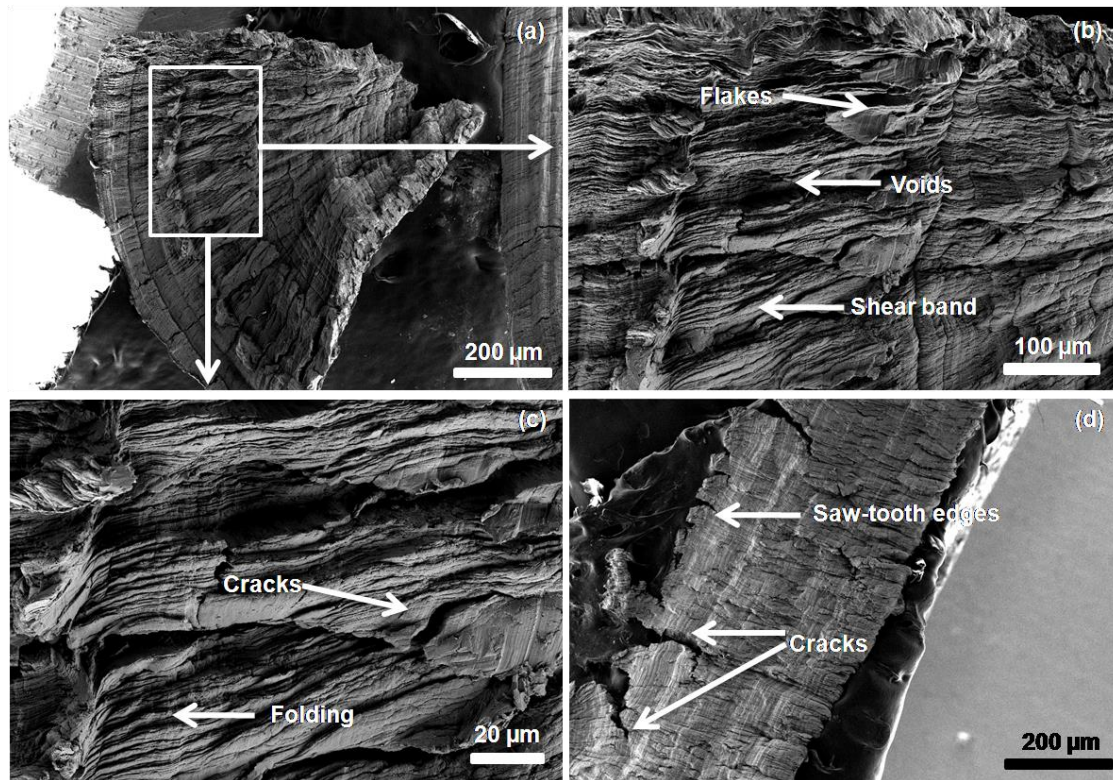


Figure 3. 28 SEM images of chip formation: (a) conical chip, (b) zoomed version of conical chip, (c) folding and cracks in conical chips, and (d) cracks and saw-tooth edges in lengthy chips.

3.7 Effect of cutting parameters on AE and IRT

The AE and IRT studies on drilling of Al-5%SiC composite have shown three stages of the drilling process. The IRT studies have also shown that 118° point angle tool is the best optimized tool for the drilling of SiC based composites. Thus, 118° point angle tool was further used to study the effect of spindle speed and feed rate on AE and tool temperature. The results obtained are described in the following sections.

3.7.1 Variation of AE time domain parameters with cutting conditions

The identified best point angle 118° tool was used for the drilling of Al-5%SiC composite under varying feed rates (0.05, 0.10, 0.15, 0.20, and 0.25 mm/rev) and spindle speeds (600, 900, 1200 and 1500 rpm). The variation of AE signals and temperature rise during drilling of

Al-5%SiC composite is recorded. The experimental details for recording of AE signal and temperature are given in section 3.1. The values of AE cumulative count and AE_{RMS} are extracted from the AE signals using AE Win software. The variation of AE cumulative count with feed rate and that of AE_{RMS} with spindle speed are shown in Fig. 3.29 (a) and 3.29 (b), respectively. It is observed from Fig. 3.29 (a) that cumulative count decreases with an increase in feed rate due to decrease in contact time between the tool and the workpiece. However, the magnitude of cumulative counts is increased for 0.15 and 0.20 mm/rev feed rates at 600 rpm spindle speed and 0.20 and 0.25 mm/rev feed rates at 900 rpm spindle speed (shown by circles in Fig.3.29 (a)). This is due to the generation of higher AE signal for the particular drill hole and possibly attributed to the encounter of the cutting tool with ceramic reinforcements. The contact of cutting tool with reinforcement (SiC) in the matrix produces burst + continuous types signal due to particle breakage and abrasion between the tool and particulates during the drilling process.

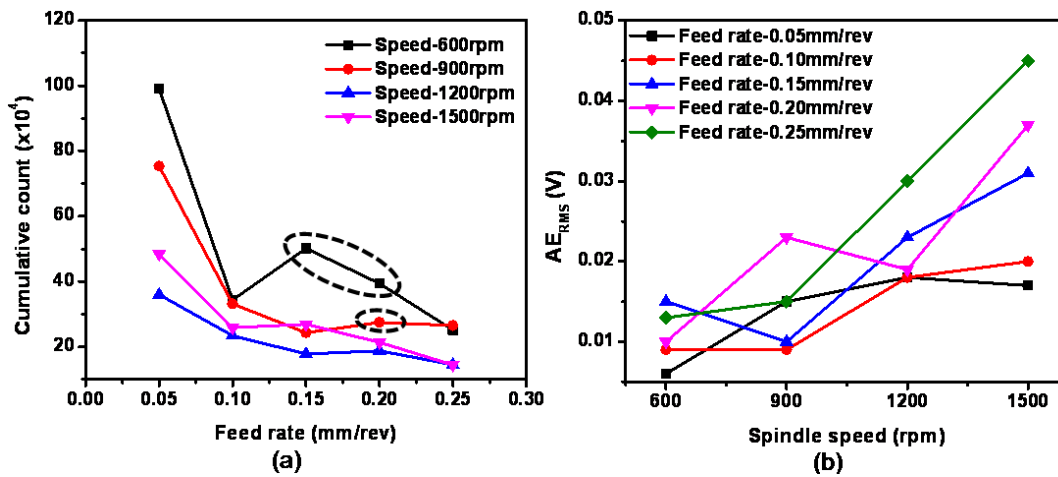


Figure 3. 29 Variation of AE features with cutting conditions (a) cumulative count vs feed rate (b) AE_{RMS} vs spindle speed.

The average AE_{RMS} values are correlated with feed rate, as shown in Fig. 3.29 (b). Though AE_{RMS} shows randomness with spindle speed but the overall trend indicates increasing order.

The AE_{RMS} is directly related to the strain rate which increases with an increase in spindle speed. The present result is in concurrence with the previous published work [99].

3.7.2 Variation of tool temperature with cutting conditions

Figure 3.30 (a) elucidates the maximum temperature rise in the cutting tool as a function of spindle speed at different feed rates. It is observed from Fig. 3.30 (a) that the tool temperature increases with an increase in spindle speed due to increase in kinetic frictional contact between the tool and the workpiece. The maximum temperature (99 °C) was obtained for the spindle speed of 1200 rpm and feed rate of 0.25 mm/rev. Figure 3.30 (b) shows linear relationship between the average tool temperature and feed rate. The results are in good agreement with the previous reported work [104].

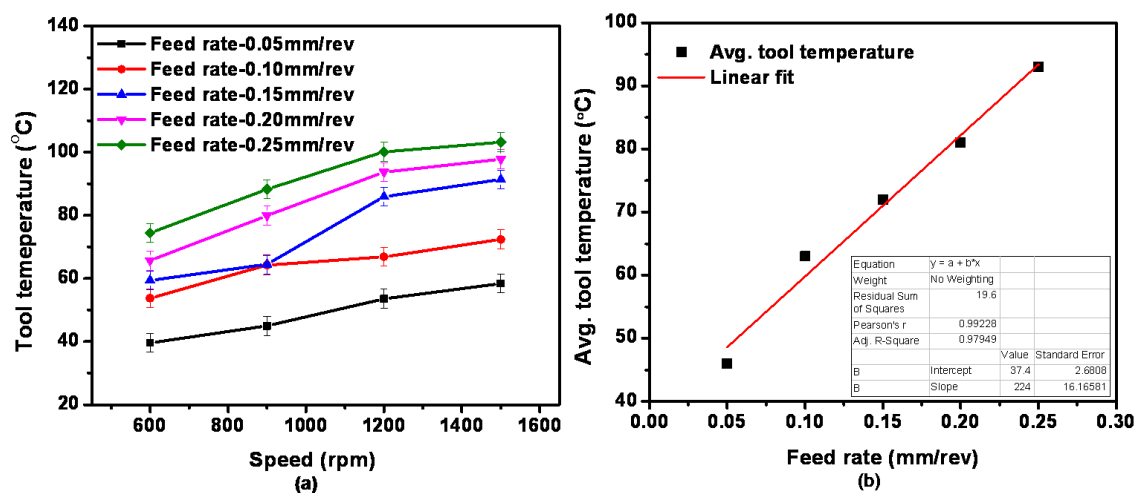


Figure 3. 30 Variation of tool temperature with cutting conditions (a) tool temperature vs spindle speed and (b) average tool temperature vs feed rate.

3.7.3 Correlation of AE_{RMS} and average tool temperature with tool wear

AE_{RMS} and tool temperature rise are two important features which indicate the condition of the cutting tool during drilling process. Figure 3.31 (a) shows the variation of AE_{RMS} and tool wear with spindle speed while Fig. 3.31 (b) shows the variation of average tool temperature and associated tool wear with spindle speed. Figure 3.31 (a) indicates that AE_{RMS} increases

with an increase in spindle speed due to increased strain rate. The increase in strain rate generates higher AE signals. Similarly, average tool temperature also increases with an increase in friction and strain rate during the drilling process.

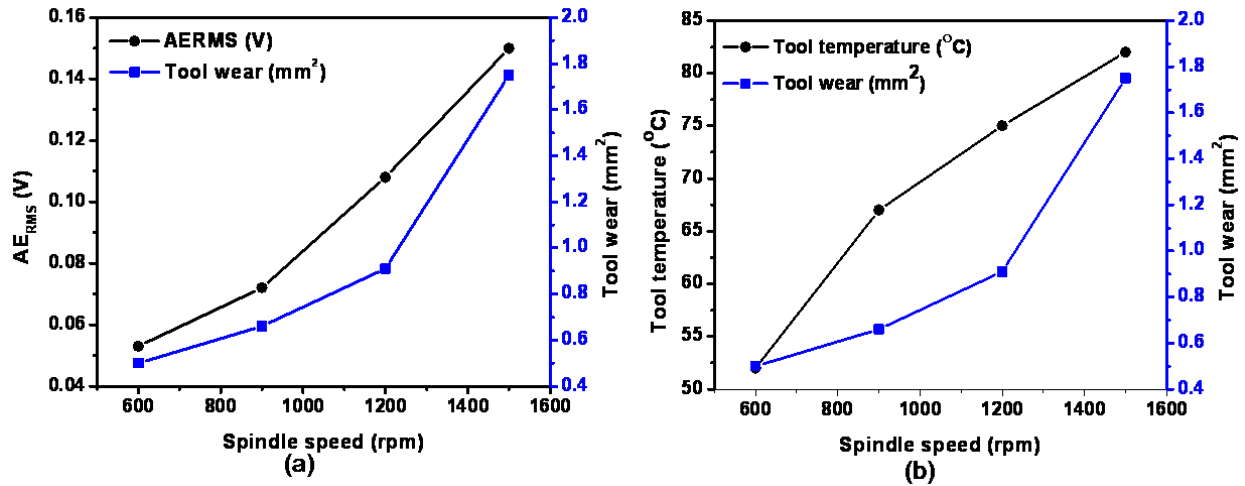


Figure 3.31 AERMS, tool temperature and tool wear correlated for different spindle speeds (600, 900, 1200 and 1500 rpm).

3.8 Summary

Acoustic emission and infrared thermography have been employed to characterize damage mechanisms and heat evolution during the drilling of Al-5%SiC composite under various cutting conditions. The following are the conclusions drawn from this study.

- ❖ The drilling process can be divided into three stages (tool entry, cutting zone, and tool exit) based on the AE time-domain results of AE count and amplitude.
- ❖ The predominant peak frequency of AE increases (227 kHz to 510 kHz) with speed and point angle. The CWT spectrum could identify the dominant frequency component existing time in the AE signals.
- ❖ The WPT could successfully identify the different damage mechanisms such as noise + friction, matrix cracking, plastic deformation, and tool wear in the drilling process by decomposing the frequency spectrum into different frequency components.

- ❖ The wavelet energy percentage is calculated for decomposed signals, and it shows that D_1 , D_2 and D_4 components carry the majority of wavelet energy percentage. It is due to noise + friction between the tool and workpiece, matrix cracking, and plastic deformation. The severe friction in turn leads to abrasive wear.
- ❖ ANOVA results show that the drill bit point angle (PCR of 42.32%) and cutting speed (PCR of 37.30%) are the more significant factors for tool temperature. The result also shows that the feed rate (PCR of 77.36%) and point angle (PCR of 37.40%) are the most influential factors for surface roughness.
- ❖ The lower point angle (90°) tool becomes blunt rapidly compared to higher point angle tools. The dominant friction leads to increased tool wear and is correlated with average cumulative energy and wavelet coefficient.
- ❖ The SEM image confirms the presence of scratches, defect void, plastic flow and cracks on the surface of the drilled workpiece.
- ❖ The maximum tool temperature rises (93°C) was observed for 1200 rpm speed at 0.12 mm/rev feed rate and point angle 90° . The simulated results are validated with experimentally obtained workpiece temperature values.
- ❖ The 118° point angle tool is optimized based on the maximum temperature rise in the cutting tool for different cutting conditions.

CHAPTER-4

**ACOUSTIC EMISSION SIGNAL ANALYSIS AND INFRARED
THERMOGRAPHY TECHNIQUE FOR THE DRILLING OF Al-5%B₄C
COMPOSITE**

This chapter presents the results of acoustic emission and infrared thermography for understanding damage in the cutting tool (118°) and heat evaluation during drilling of Al-5%B₄C composite. The main emphasis of this part of the thesis is the analysis of time domain, frequency domain and time-frequency domain at individual stages of AE signals and correlation to drilling conditions and tool damage. The continuous wavelet transform (CWT) and wavelet packet transform (WPT) were applied to AE signals to identify the specific damage mechanisms operating in the drilling. The usefulness of AE signal parameters i.e., AE_{RMS} and wavelet coefficient are discussed with respect to tool wear. On the other hand, heat evolution, chip formation, and temperature rise in the cutting tool and workpiece are discussed. Also, a finite elemental model is implemented to validate the workpiece temperature. The quality of the drilled surface and damage in the cutting tool are characterized using scanning electron microscope (SEM).

4.1 Experimental details

Al-5%B₄C composite workpiece (70 x 100 x 10 mm³) was subjected to dry drilling tests. The drilling parameters are varied for different feed rates (0.05 - 0.25 mm/rev) in the interval of 0.05 mm/rev at four constant spindle speeds (600, 900, 1200 and 1500 rpm) as shown in Table 4.1.

Table 4. 1 Conditions for the drilling tests.

Parameters	Cutting conditions
Spindle speed (rpm)	600, 900, 1200, 1500
Feed rate (mm/rev)	0.05, 0.10, 0.15, 0.20, 0.25
Drilled depth (mm)	10

4.2 AE signals analysis

4.2.1 Time domain analysis

AE signals recorded during drilling of Al-5%B₄C composite were analyzed. AE time domain parameters (AE counts, amplitude, energy, and root mean square voltage) are correlated with cutting time and drilling conditions (i.e., feed rate and spindle speed). Figures 4.1 (a) and (b) depict the variations of AE count and amplitude with cutting time for 600 rpm speed and 0.05 mm/rev feed rate. The obtained AE counts and amplitude results show three different stages, i.e., stage I (tool entry), stage II (cutting zone), and stage III (tool exit). In tool entry (stage I), the cutting tool starts indentation and shears with the workpiece prior to the start of rigorous cutting. In this stage, AE count and amplitude (40 dB to 78 dB) increase due to tool indentation, and shear deformation of the workpiece. The dense burst and continuous type AE signals are observed in this stage. The severe cutting starts after indentation; which is called cutting zone (stage II) wherein AE counts suddenly decreases and indicates random nature because of continuous crack propagation and friction between the tool-workpiece. In stage II, the minority of burst and majority of continuous type signals are noticed. The amplitude of AE signals almost increases with cutting time and the maximum amplitude value (78 dB - 99 dB) is observed in stage II.

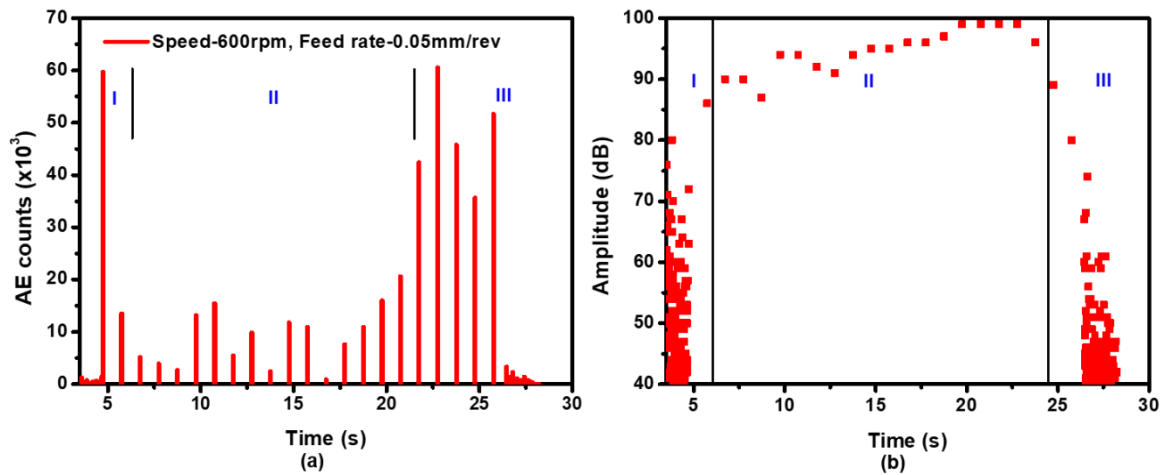


Figure 4. 1 Variation of AE time domain parameters with time for 600 rpm speed and 0.05 mm/rev feed rate (a) AE count, and (b) amplitude.

Further, it is observed that AE counts increases again after 19 sec upto 24 sec and this is due to penetration of the cutting tool in to the back wall of the workpiece. The penetration causes severe back wall fracture of the workpiece which generates dense majority of burst signals associated with high magnitude AE counts. The increase in AE count and amplitude after 19 sec thus indicates back wall fracture of the workpiece.

In stage III, AE count and amplitude (65 dB - 40 dB) decrease due to exit of the tool from the workpiece, wherein friction dominates between the tool and workpiece. The classification of AE count and amplitude reveals three stages of drilling mechanism in Al-5%B₄C composite. This is in line with the result obtained for Al-5%SiC composite discussed in the previous chapter. The results are in good agreement with the earlier reported results [96]. Further, the values of AE cumulative count and cumulative energy are extracted using AE Win software and plotted with feed rate for different cutting speeds, as shown in Figs. 4.2 (a) and (b). It is observed from Fig. 4.2 (a) that cumulative count decreases with an increase in feed rate (0.05 - 0.25 mm/rev) and this is due to decrease in contact time between the tool and the workpiece. The variation of cumulative count for different speeds shows fluctuation due to inhomogeneity and porosity in the workpiece. However, decreasing trend in the variation of

cumulative count with speed is observed. The contact of the cutting tool with reinforcement (B₄C) in the matrix triggers both burst and continuous types of AE signals because of particle breakage and abrasion between the tool and particulates during the drilling process. Figure 4.2 (b) reveals that AE cumulative energy exponentially decreases with feed rate. The cumulative energy also decreases with spindle speed.

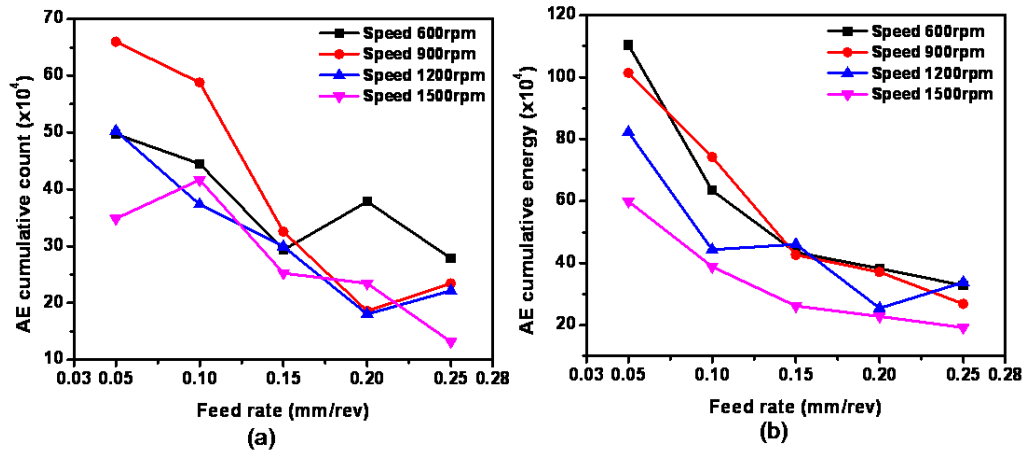


Figure 4. 2 (a) AE cumulative count and (b) AE cumulative energy as a function of feed rate for different speeds.

The average AE_{RMS} value is also correlated with feed rate, as shown in Fig. 4.3. Though AE_{RMS} shows random variation with feed rate, the overall trend indicates an increasing order. On the other hand, the magnitude of AE_{RMS} increases with an increase different feed rates at different speeds. The present result is in concurrence with the previously published work [96].

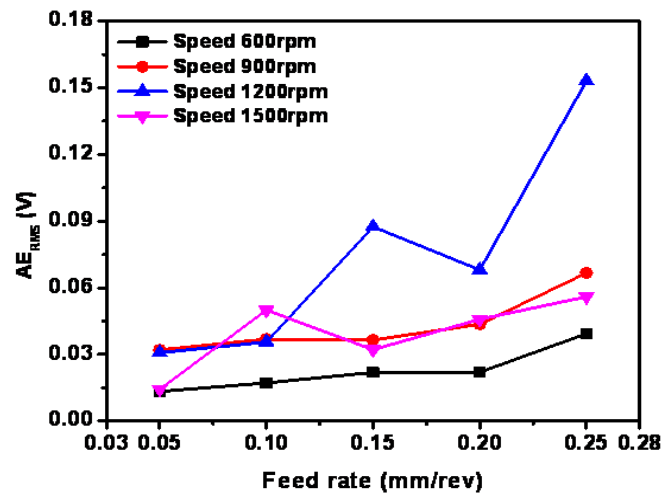


Figure 4. 3 Variation of AE_{RMS} with feed rate at different speeds.

4.2.2 Frequency domain analysis

The fast Fourier transform (FFT) was applied to the AE signals to understand various frequency components presents in the signals. The waveform and the corresponding frequency spectrum of the AE signals are shown in Figs. 4.4 (a-d) and Figs. 4.5 (a-d) for different speeds (600, 900, 1200 and 1500 rpm) at constant feed rate (0.05 mm/rev). Figure 4.4 (a) depicts that the burst and continuous type of signals and the corresponding predominant frequency is 550 kHz (Fig.4.4 (b)) for 600 rpm speed and 0.05 mm/rev feed rate. This is associated with friction, tool indentation and fresh sharp edges of the cutting tool that blunts rapidly in the first hole at beginning of the drilling process. Figures 4.4 (c) and (d) reveal the dense majority of burst and mixed burst + continuous waveforms, and predominant frequency (294 kHz) for 900 rpm speed and 0.05 mm/rev feed rate. The increase in speed from 600 rpm to 900 rpm results in more chip breaking/collision and increased friction which produces burst and mixed (burst + continuous) AE signals. The friction test was carried out to confirm the obtained AE results as shown in Figs. 4.5 (a)-(b).

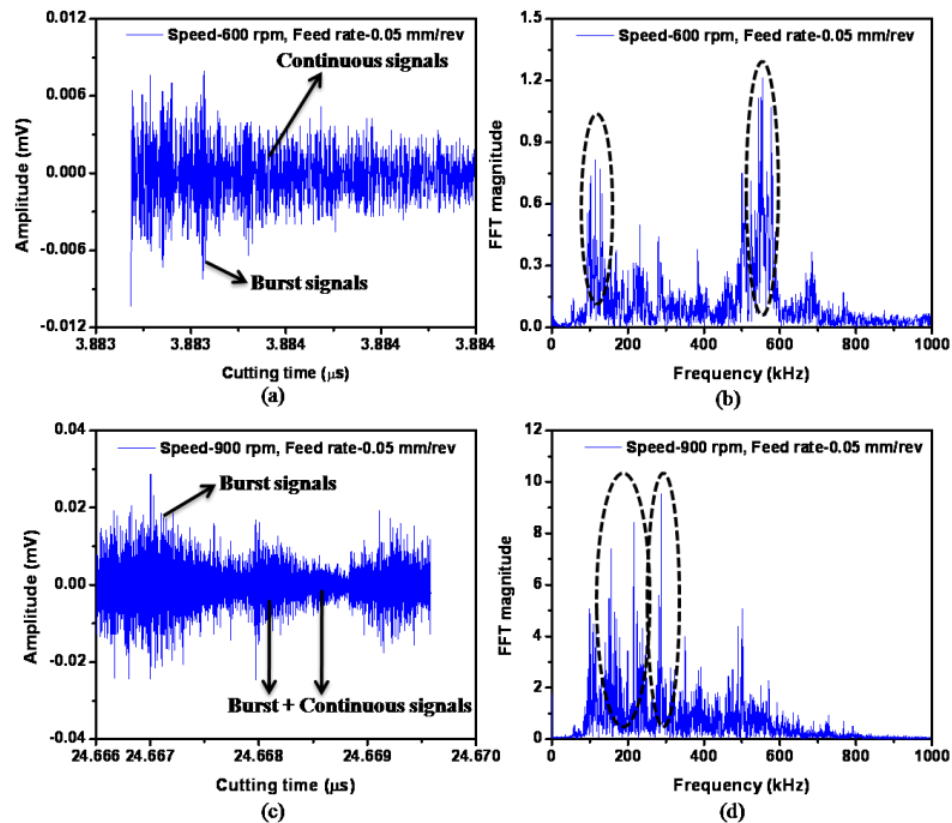


Figure 4. 4 AE waveforms (a and c) and its frequency spectrum (b and d) for different speeds (600 rpm and 900 rpm) at constant feed rate (0.05 mm/rev).

The high amplitude (0.15 mV) and dense burst type waveform for 1200 rpm speed and 0.05 mm/rev feed rate are shown in Fig. 4.5 (a). Figure 4.5 (b) reveals the predominant frequency as 582 kHz and scattered frequency band of 100 kHz - 582 kHz and this is associated with increase in friction/rubbing, crack propagation, and progression of tool wear. The low frequency band (100 kHz - 250 kHz) is possibly due to friction and tool wear. The high frequency (250 kHz - 582 kHz) band can be attributed to the fracture of B₄C particles and tool fracture. The continuous and dense burst type signals are observed for 1500 rpm speed and 0.05 mm/rev feed rate, as shown in Fig. 4.5 (c). The emission of burst signal increases with increasing speed, which is due to increased chip breaking rate and crack propagation. The FFT spectrum (Fig. 4.5 (d)) for 1500 rpm speed shows scattered and reduced predominant frequency due to higher friction/rubbing between the tool and workpiece. The

scattered frequency increases with increase in speed (600, 900, 1200, 1500 rpm) at a constant feed rate.

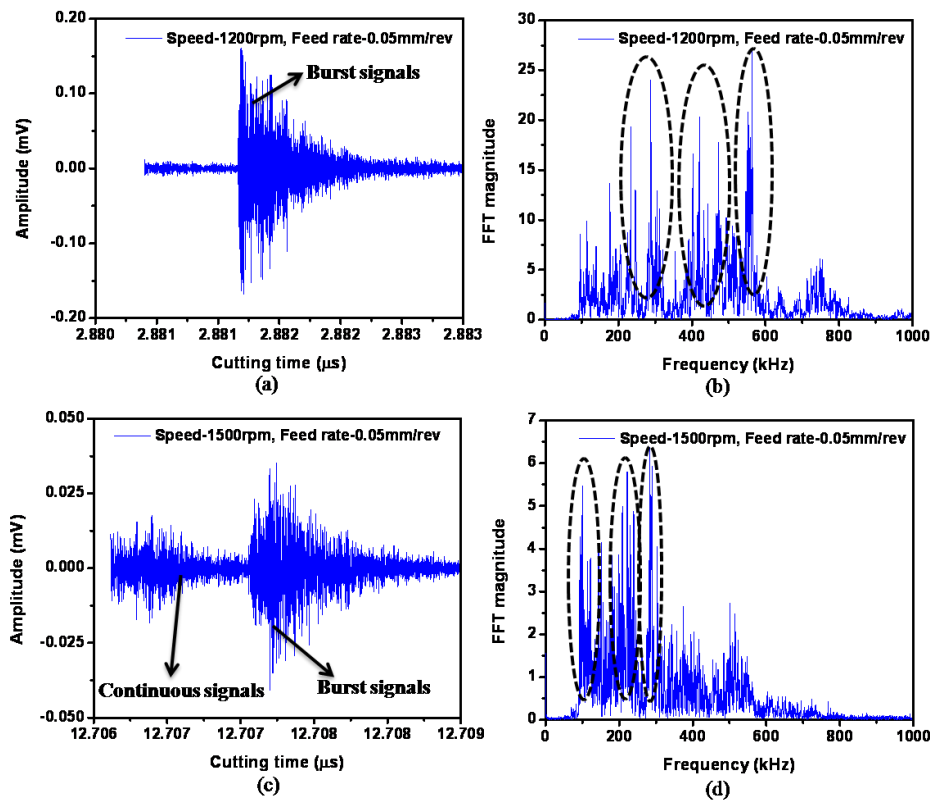


Figure 4. 5 AE waveforms (a and c) and its frequency spectrum (b and d) for different speeds (1200 rpm and 1500 rpm) at constant feed rate (0.05 mm/rev).

Friction tests have been carried out to confirm the wavelet components. It is observed that the continuous types of signals are generated in the friction tests while burst types of AE signals are observed for the matrix crack test, as shown in Figs. 4.6 (a) and (d). It is confirmed from Figs. 4.6 (a) and (b) that the continuous signal and frequency of 160 kHz is corresponding to friction between the tool and workpiece. A tensile test has been carried out to confirm the matrix crack, as shown in Figs. 4.6 (c) and (d). The burst type of AE signal and frequency of 110 kHz is observed from the matrix crack test. Similarly, chip breaking test and tool indentation are shown in Figs. 4.7 (a) and (d). The burst types of AE signal and high frequency (372 and 665 kHz) components are noticed in the chip breaking tests. The burst

types and high frequency of 582 kHz of AE signals are observed from the tool indentation test. The above-discussed confirmation tests of AE signals and their frequency component are almost similar to the existing time-frequency domain results.

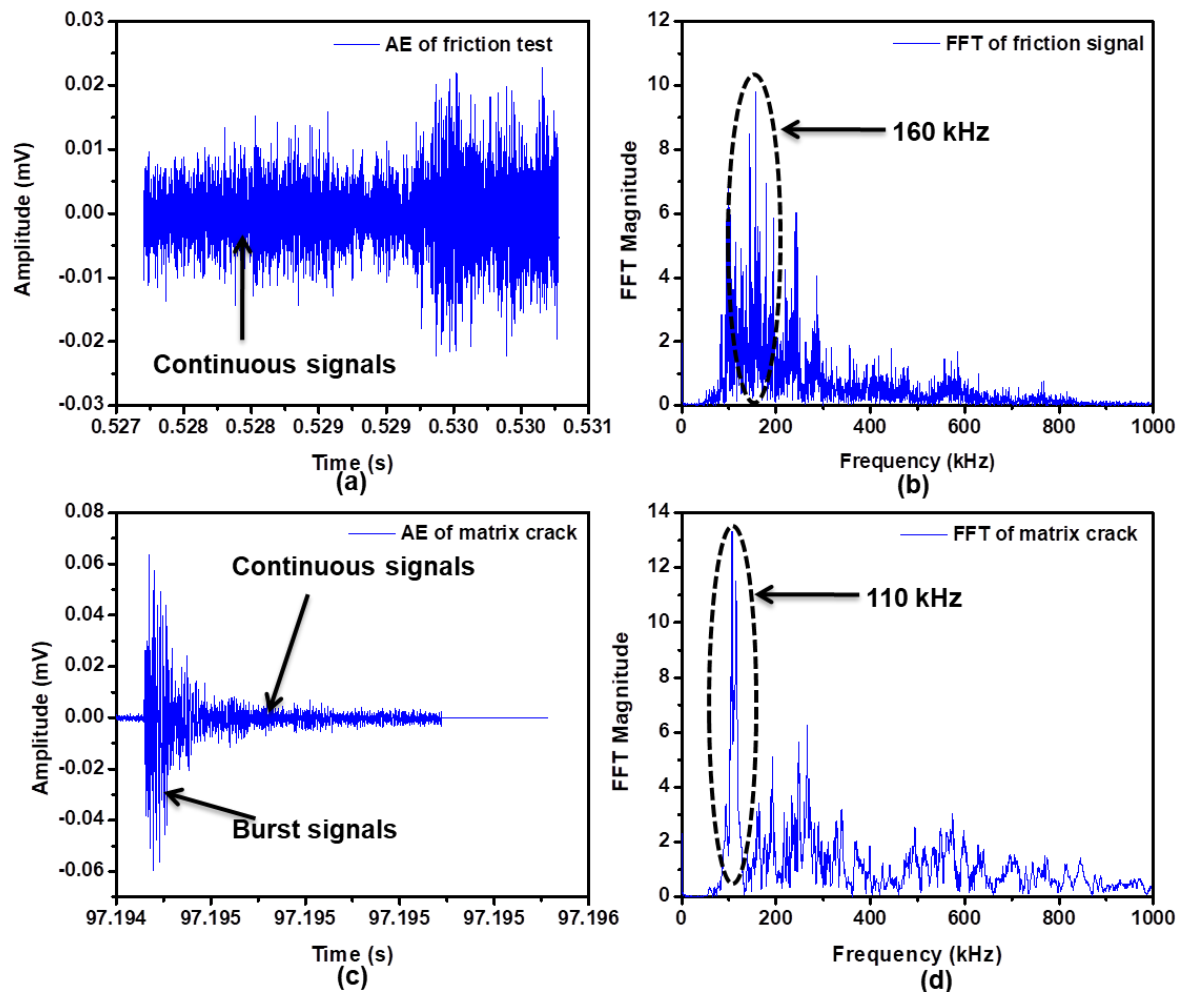


Figure 4. 6 Frequency domain analysis of AE signal (a and b) AE waveform and FFT spectrum of friction test, (c and d) AE waveform and FFT spectrum of matrix crack.

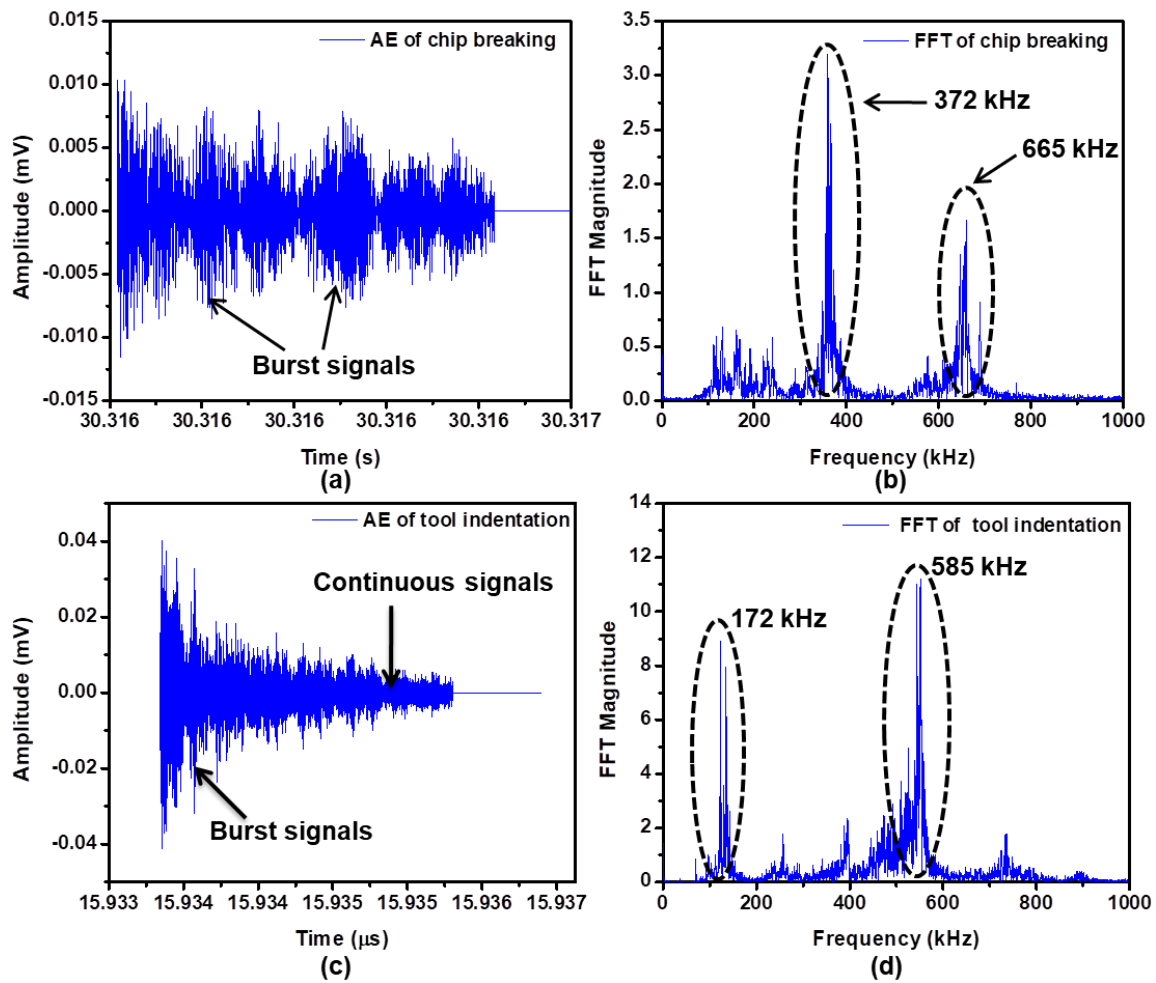


Figure 4. 7 Frequency domain analysis of AE signal: (a and b) AE waveform and FFT spectrum of chip breaking, (c and d) AE waveform and FFT spectrum of tool indentation.

4.2.3 Wavelet packet analysis of AE signals

WPT is an advanced signal processing technique and was applied to investigate various AE sources involved in the drilling of Al-5%B₄C composite. WPT code was written in MATLAB using wavelet toolbox. The WPT provides AE energy value for each decomposed component, which represents the frequency bands with highest and lowest activities. A large number of waveforms are recorded during the drilling tests. The wavelet energy percentage and frequency band obtained from the waveforms were used to characterize the different sources of AE. The entropy criteria and Daubechie's mother wavelet family were utilized. As per

Nyquist theorem, the signal is sampled at twice the highest frequency contained in the signal. Thus, the sampling rate was kept at 5 MHz since peak frequency of the signal was upto 1 MHz. The decomposition frequency (1 MHz) was selected based on the predominant frequency (582 kHz) existing in the signal which is shown in the FFT spectrum (Figs. 4.5). The number of levels was set to four ($j=4$) and thus the number of decomposed components will be sixteen ($i=2^4$) with frequency interval of 62.5 kHz. The wavelet packet analysis of AE signals for Al-5%SiC MMC conducted in chapter 3 was done for the signals generated in stage II i.e., cutting zone. In the present chapter, AE signal generated at different stages are considered for the WPT analysis and the results for 600 rpm speed and 0.05 mm/rev feed rate are given in Table 4.1. The low frequency band (D_1 : 0-62.5 kHz) was eliminated because it could contain environmental noise. Since, 4 level decomposition is carried out in this work, the D_1 component can be neglected. The second frequency component (D_2 : 62.5-125 kHz) is related to friction/rubbing in the drilling process and the wavelet energy increases from 41.53% in the tool entry to 58.43% in the tool exit stage due to increase in the depth of cut. The third component (D_3 : 125-187.5 kHz) corresponds to matrix cracking. The wavelet energy for matrix cracking decrease from 15.93% to 11.40% while tool entry to exit stage. The fourth component is related to plastic deformation which increases (17.15% to 19.39%) with increase in the depth of cut. Based on the wavelet energy percentage, AE source mechanism in different stages of drilling were tabulated and shown in Table 4.2. This indicates that the various AE source mechanisms are involved in the drilling process at different stages.

Table 4. 2Wavelet energy percentages for three different stages at 600 rpm speed and 0.05 mm/rev feed rate.

Frequency band (kHz)	Tool entry (Stage I)	Cutting zone (Stage II)	Tool exit (Stage III)
D ₁ : 0-62.5	20.93423	11.59936	8.349626
D ₂ : 62.5-125	41.53478	32.66518	58.42877
D ₃ : 125-187.5	15.93373	30.91123	11.40224
D ₄ : 187.5-250	17.15201	19.48359	19.39529
D ₅ : 250-312.5	0.056034	0.091271	0.058789
D ₆ : 312.5-375	0.076177	0.080555	0.087925
D ₇ : 375-437.5	3.419111	4.402213	1.714748
D ₈ : 437.5-500	0.73512	0.35916	0.153176
D ₉ : 500-562.5	0.004794	0.020668	0.038868
D ₁₀ : 562.5-625	0.007175	0.028287	0.053073
D ₁₁ : 625-687.5	0.015498	0.06216	0.062649
D ₁₂ : 687.5-750	0.011361	0.04696	0.047885
D ₁₃ : 750-812	0.047719	0.062834	0.071957
D ₁₄ : 812-875	0.034113	0.06147	0.072281
D ₁₅ : 875-937.5	0.016043	0.067557	0.036174
D ₁₆ : 937.5-1000	0.022103	0.057513	0.024068

Table 4. 3 AE source mechanisms in the three stages of drilling process.

Frequency band (kHz)	AE source mechanisms	Tool entry	Cutting zone	Tool exit
D ₁ : 0-62.5	Noise	Present	Present	Present
D ₂ : 62.5-125	Friction + tool wear	low	High	Very high
D ₃ : 125-187.5	Matrix cracking	Low	Very high	No
D ₄ : 187.5-250	Plastic deformation	High	Very high	No
D ₆ : 312.5-375	Chip breakage	Low	Very high	Very low
D ₇ : 375-437.5	Tool and particle fracture	Low	High	No

The wavelet energy ratio for different speeds was also determined and its variation with the number of decomposed components for different speeds (600, 900, 1200, 1500 rpm) and at 0.05 mm/rev feed rate is shown in Fig. 4.8. The wavelet energy percentage was calculated using MATLAB code. The energy percentage distribution graph is shown for only eight components because beyond that the energy percentage become almost zero (negligible). It is understood from the point plot (Fig.4.8) that the wavelet energy distribution is concentrated in three components (i.e., decomposed components 2, 3, and 4). The effect of spindle speed on three (2, 3 and 4) energy components are also shown in Fig. 4.8. The wavelet energy ratio (component 2) corresponds to friction and tool wear and it increases with increase in speed due to more kinetic force between the tool and workpiece. This is the dominant damage mechanism from beginning to end of the drilling process. The component 3 is associated with matrix cracking and it decreases with an increase in speed because of the formation of build-up edge on the tool resulting in dominant frictional energy source. The shear/plastic deformation (component 4) increases with an increase in speed.

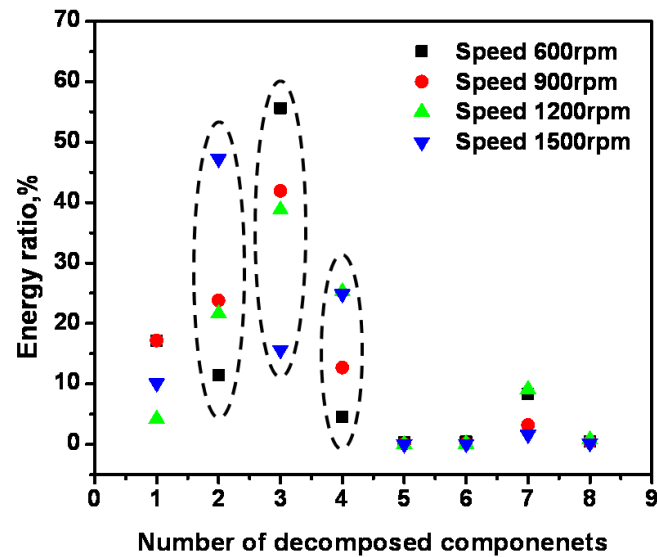


Figure 4. 8 Decomposition of AE signals for different speeds (600-1500 rpm).

Figure 4.9 describes the energy percentage distribution of AE signals as a function of spindle speed. As mentioned above the energy is concentrated on particular bands, i.e., band 2-3 and band 4-16. The frequency band (2-3) increases from 65% to 90% with increase in spindle speed (600 to 1500 rpm) due to increase in friction between the tool and workpiece, which leads to tool wear. On the other hand, frequency band 4-16 decreases with increase in spindle speed. The observed results are concomitant with earlier reported results [89].

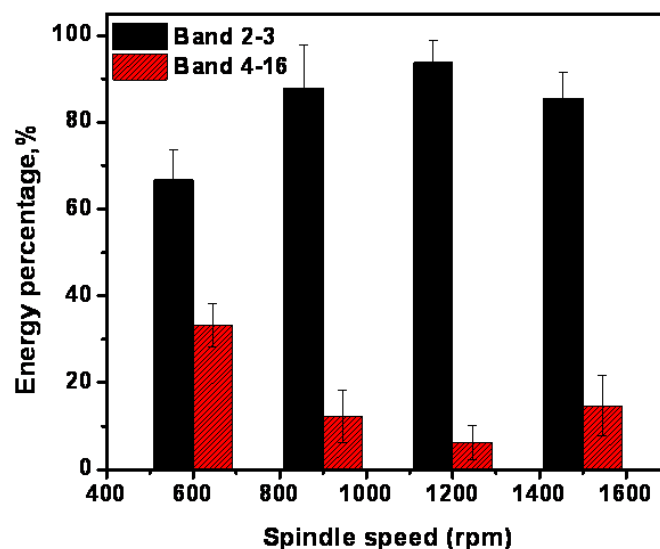


Figure 4. 9 Wavelet energy distribution of AE signals at different speeds (a) wavelet energy ratio for band (2-3), and (b) energy ratio for band (4-16).

4.3 Temperature analysis

4.3.1 Heat evaluation during drilling process

The temperature rises during drilling of Al-5% B₄C composite was recorded as thermal images using infrared thermography. Following the procedure described in section 3.3 box contour was utilized to obtain the temperature line profile for different drilling tests. The temperature line profile with cutting time for 600 rpm speed and 0.05 mm/rev feed rate is shown in Fig. 4.10 (a). The variation of temperature rises with time shown oscillatory pattern due to continuous rotation of the cutting tool and chip evacuation during drilling. This oscillatory pattern of temperature rise profile is similar to that observed in Al-5%SiC composite as described in the previous chapter and is in good agreement with the work reported by Saez-de-Buruaga [103]. Similar plot for 1500 rpm speed and 0.25 mm/rev feed rate is shown in Fig. 4.10 (b). But the maximum temperature is observed in between the drilling process at 24 sec in Al-5%B₄C composite while the maximum temperature notice at 7 sec and this is very close to the tool exit stage in Al-5%SiC composite. It is observed from Fig. 4.10 (a) that temperature increased upto some specific time and almost stabilized and then increased again to temperature 43°C due to back-wall fracture of the workpiece. Beyond that, the temperature decreases rapidly due to tool exit from the workpiece.

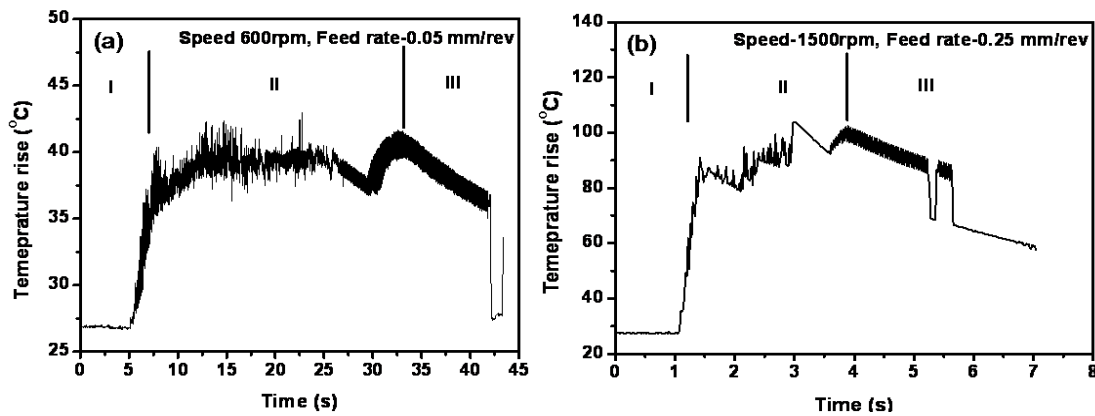


Figure 4. 10 Three stages of temperature rise for different cutting parameters (a) temperature rise with time for 600 rpm speed and 0.05 mm/rev feed rate (b) temperature rise with time for 1500 rpm speed and 0.25 mm/rev feed rate.

Figure 4.10 also shows that the temperature line profile during drilling of Al-5%B₄C composite could be classified into three stages. Stage I is the tool entry stage (pre-drilling + indentation), stage II is cutting stage, and stage III is the tool exit stage. In stage I, the cutting tool rotates and moves in the z-direction. Once the drill bit contacts the workpiece, the chisel edges start to rub with the surface of the workpiece and initiate the cutting process with removal of chips. Low tool temperature is observed before rigorous cutting starts. But, once drill bit edges begin to extrude the workpiece, temperature increases with an unprecedented manner from ambient temperature to 40 °C.

Stage I is followed by stage II, where severe cutting occurs with the attainment of maximum temperature. In stage II, complete interaction of drill lips with the workpiece takes place, and this produces a considerable amount of chips. In this stage, the maximum temperature of 43 °C was noted. This is due to the effect of shear deformation, matrix cracking, and kinetic friction between the tool and the workpiece. The breakage of B₄C particles also results in heat generation. In stage III, the tool exit from the workpiece leads to the drastic drop in temperature upto 28 °C. These results are in good agreement with the earlier reported results [128]. It is also seen that for 1500 rpm speed and 0.25 mm/rev feed rate, temperature

increases non linearly with time (Fig. 4.10 (b)). This is due to the presence of B₄C reinforcement in Al matrix. The maximum temperature observed for this test was 103 °C.

The thermal images extracted from different stages of the drilling process for 1500 rpm speed and 0.25 mm/rev feed rate, are shown in Figs. 4.11 (a) - 4.11 (c). The temperature rise corresponding to different stages is shown at top of the thermal images. Three stage of drilling can be observed from the thermal images.

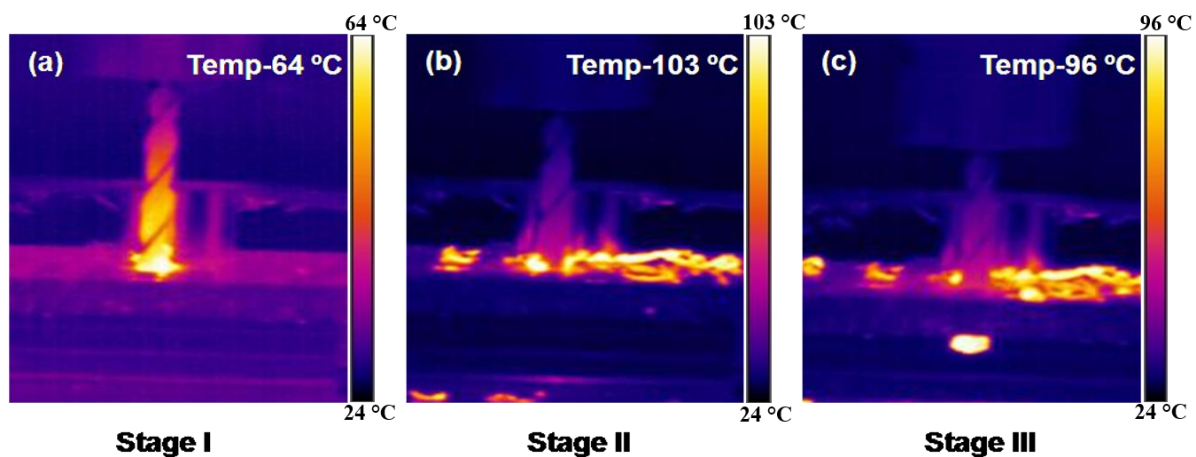


Figure 4. 11 Three stages of thermal images during drilling of Al-5%B₄C composite for 1500 rpm speed and 0.25 mm/rev feed rate: (a) stage I (b) stage II (c) stage III.

4.3.2 Tool temperature and its correlation with cutting parameters

Figures 4.12 (a) and 4.12 (b) reveal the variation of tool temperature as a function of speed (600 -1500 rpm) for different feed rates (0.05 - 0.25 mm/rev). The tool temperature increases with an increase in speed at different feed rates due to high frictional contact between the tool and workpiece [120]. For any particular speed, tool temperature also increases with an increase in feed rate. The lowest tool temperature rise (43 °C) was observed for 600 rpm speed and 0.05 mm/rev feed rate, and this is due to low frictional contact between the tool and workpiece. On the other hand, the temperature measured for 1500 rpm speed and 0.25 mm/rev feed rate was maximum (103 °C) due to increased frictional contact between the tool

and workpiece. It is also observed from Fig. 4.12 (b) that the average tool temperature increases linearly with speed.

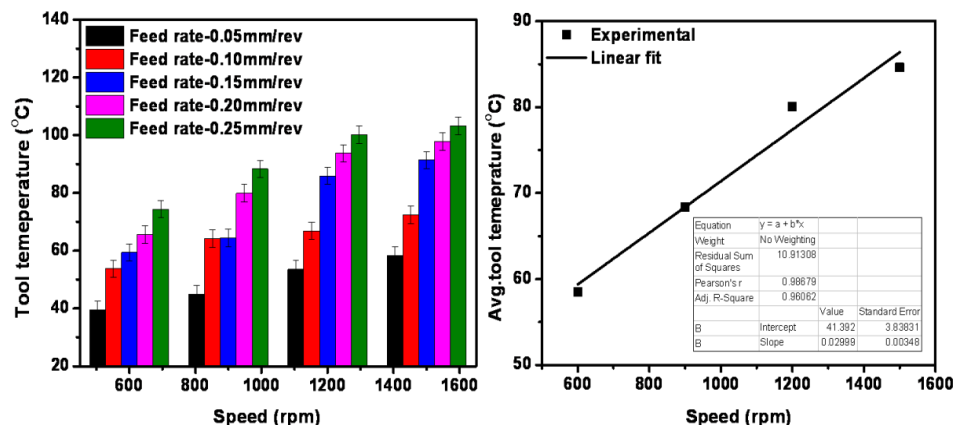


Figure 4. 12 Temperature rises with cutting parameters: (a) tool temperature as a function of speed at different feed rates and (b) average tool temperature as a function of speed.

4.3.3 Numerical model for the validation of workpiece temperature

A numerical model based on COMSOL Multiphysics was used to validate the measured experimental data. The model was used to predict heat distribution in the workpiece due to drilling. The density and specific heat capacity of the workpiece material (Al-5%B₄C MMC) were calculated from the individual constituents present in the composite. The value of thermal conductivity, density, and heat capacity of the workpiece material and cutting tool are given in Table 4.3. ASTM standard was used to determine the properties of the composite material while Matweb was used for the M2 HSS tool material. The density of Al-5%B₄C composite was measured as per ASTM D792 standard. The values of specific heat capacity and thermal conductivity of the workpiece material were determined based on the earlier report [130]. A convective thermal flux with convective coefficient value of 10 W/m²K was imposed on the surface of the drill bit and workpiece. For the simulation work, an ambient temperature equal to 20 °C was considered and thermal insulation was fixed on the remaining contours.

Table 4. 4 Material properties used for the numerical simulation.

Property	Al-5%B ₄ C composite	HSS drill bit
Thermal conductivity [W/mK]	162	41.5
Density [kg/m ³]	2690	8138
Heat capacity [J/kg.K]	900	460

Figure 4.13 shows the mesh along with the boundary conditions. The simulation was carried out for drilling conducted at 1500 rpm speed, and 0.25 mm/rev feed rate. The experimentally obtained maximum tool tip temperature of 103 °C from IR thermography was imposed on the tool to workpiece interface as a heat source.

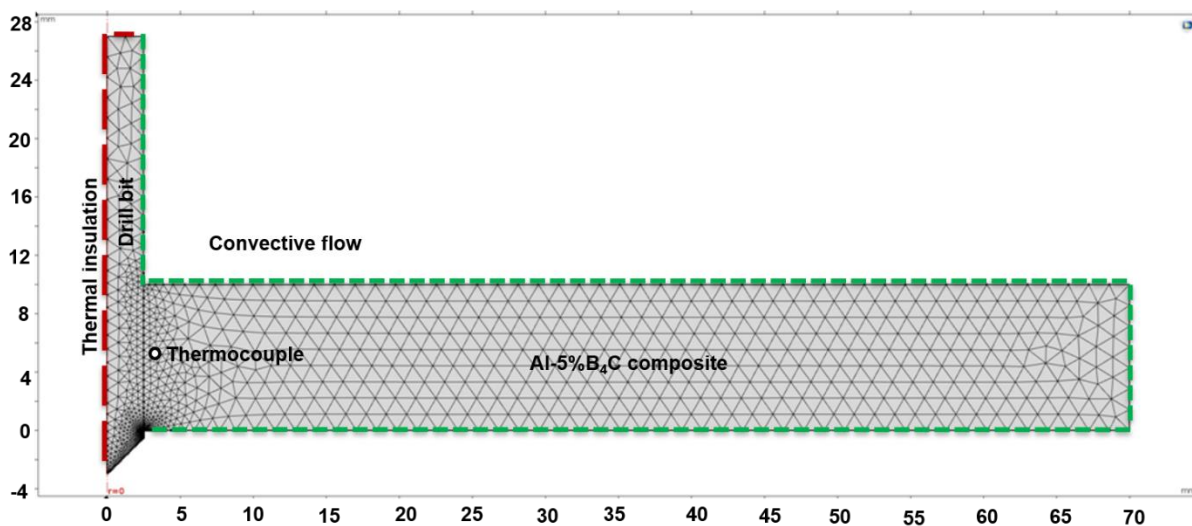


Figure 4. 13 Mesh and boundary conditions for the model.

A K-type thermocouple was embedded at a 2 mm distance from the drilled hole surface to obtain the workpiece temperature. The thermal field distribution in the workpiece is shown in Fig. 4.14. The thermal field distribution on the workpiece is correlated with the experimentally obtained workpiece temperature. It is seen that the simulated workpiece temperature (95.4 °C) is very close to the experimentally obtained workpiece temperature (98 °C) by thermocouples.

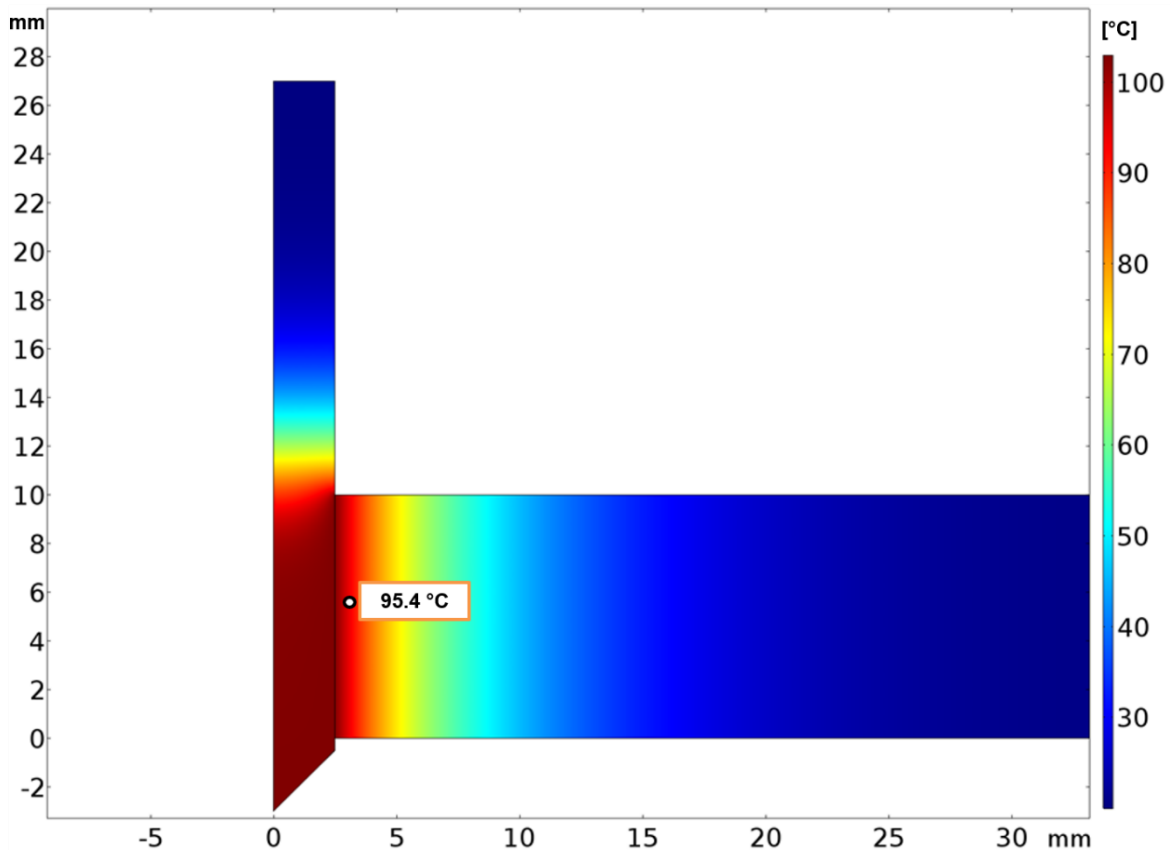


Figure 4. 14 Thermal field distribution in workpiece at 2 mm distance from drilled hole.

4.4 Characterization of tool wear

The major types of tool wear formed on HSS drills are flank wear, BUE, chipping, tool edge wear, and abrasive wear during the drilling of Al-5%B₄C composite. Figures 4.15 (a) to (d) show the optical images of the damaged tool after different holes. The flank edge wear and BUE on chisel edge were observed after five drill holes drilled at 600 rpm spindle speed and different feed rates, as shown in Fig. 4.15 (a). This is due to initial sharp cutting edges of the drill bit and lower spindle speed. Figure 4.15 (b) reveals non-uniform flank wear and increased BUE on chisel edge after ten drill holes (after drilling for different feed rates at 900 rpm speed) which is due to increased thrust force and cutting temperature. Figure 4.15 (c) depicts adhesion wear on the flank surface and the deposition of large amount of matrix particle on chisel edge after fifteen drill holes (after drilling for different feed rates at 900 rpm

speed). This is because of high cutting temperature and ductile characteristics of the matrix material. After twenty drill holes (after drilling for different feed rates at 1500 rpm speed), catastrophic edge fracture and chipping were observed in the cutting edge (Fig. 4.15 (d)) due to increased thrust force and torque. This observation is in line with the earlier reported works [98].

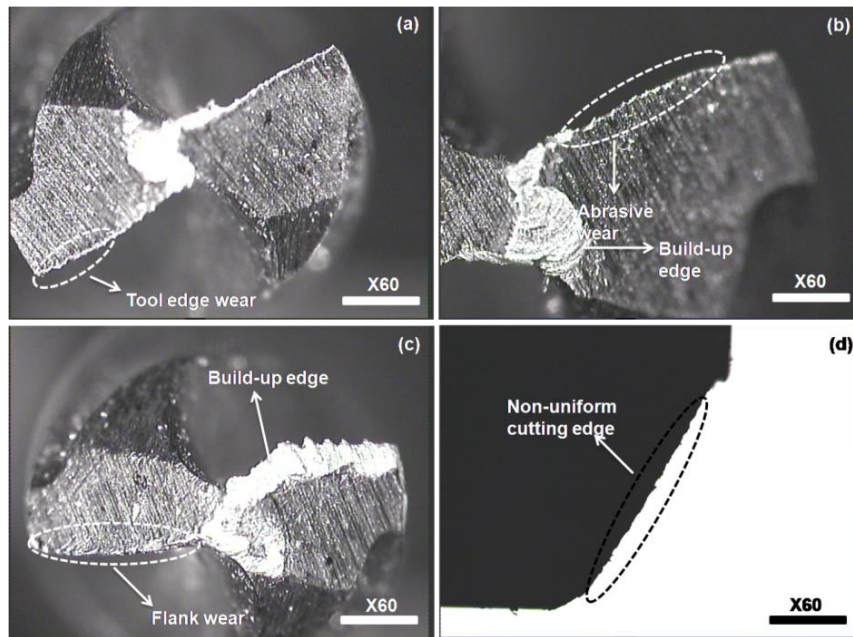


Figure 4. 15 Optical images of the cutting tool for different drilling conditions (a) after five drill holes, (b) after ten drill holes, (c) after fifteen drill holes, and (d) after twenty drill holes. In addition, the SEM was used to evaluate damage in the cutting tool and reveal more insight into the mechanism of tool wear in Al-5%B₄C composite after drilling. The SEM characterization of the cutting tool was done after all the drill tests. Different types of wear formed on the cutting tool i.e., flank wear, tool edge chipping, BUE on chisel face and adhesion wear are observed as shown in Figures 4.16 (a) - 4.16 (d). Fig. 4.16 (a) reveals the overall view showing various damages present in the cutting tool. Figure 4.16 (b) depicts the Build-up-edge formation on chisel edge and cutting-edge wear due to temperature rise in the matrix. There are lot of grooves on the flank face due to cutting edge contact with hard and

brittle B_4C particles. This is in good agreement with earlier reported results for drilling of Al/ Al_2O_3 MMC [98]. Tool edge chipping was observed (Fig. 4.16 (c)) due to high contact force and pressure. Figure 4.16 (d) reveals the deposition of Al alloy matrix on flank face and this is due to lower cutting speed and higher feed rate.

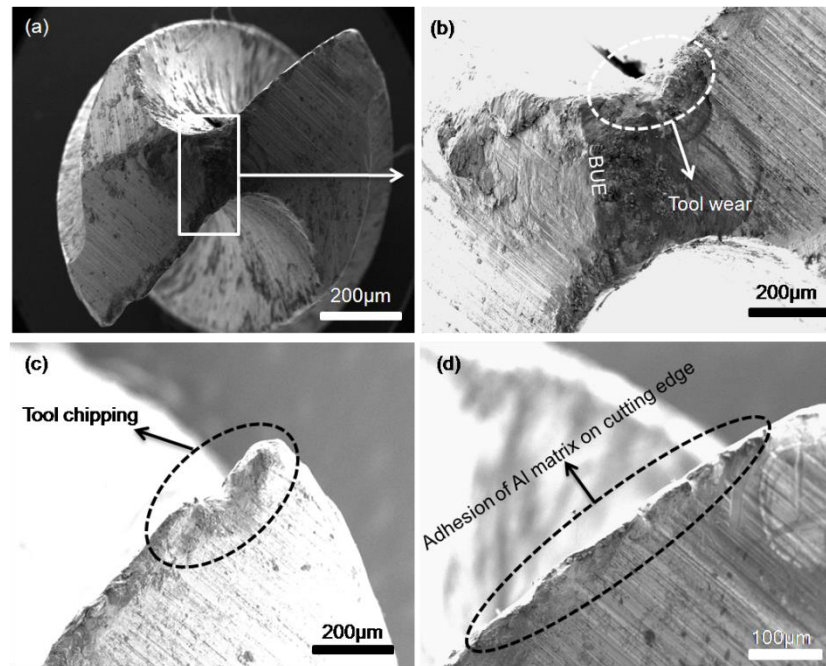


Figure 4. 16 SEM images of worn-out tool (a) overall view after twenty drill tests, (b) BUE formation and tool wear, (c) tool chipping, and (d) adhesion wear.

4.4.1 Correlation of tool wear with AE features

The AE_{RMS} and wavelet coefficient values were determined from signals acquired at different drilling conditions and compared with the quantified values of tool wear. Wavelet transform was applied to the AE signals using Vallen software. The time-frequency wavelet results for drilling at 600 and 1500 rpm speed and 0.05 mm/rev feed rate are shown in Figs. 4.17 (a) - 4.17 (b). The wavelet coefficient was extracted from the AE signals corresponding to each drill hole and the average wavelet coefficient was correlated with tool wear.

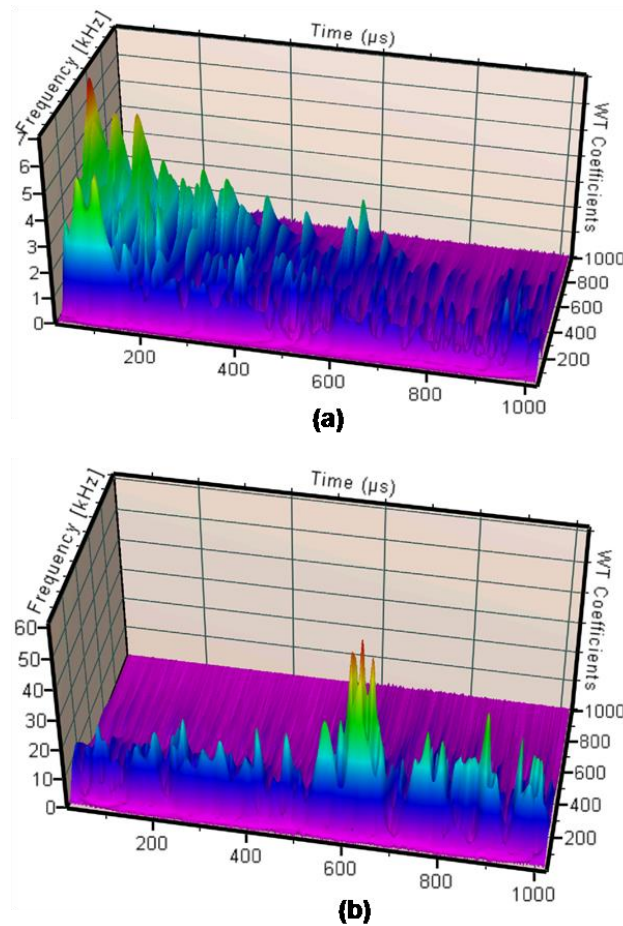


Figure 4. 17 Wavelet transformation of AE signals for two different speeds and 0.05 mm/rev feed rate (a) 600 rpm, and (b) 1500 rpm.

Figures 4.18 (a) and (b) describe tool wear and the corresponding AE parameters (i.e., AE_{RMS} and wavelet coefficient) values. From Fig. 4.18 (a) it is noted that the tool wear and AE_{RMS} increase with an increase in spindle speed due to increased friction between the tool and the workpiece. Tool wear and wavelet coefficient value increase with an increase in spindle speed as shown in Fig. 4.18 (b). The AE_{RMS} and wavelet coefficient are sufficient parameters to understand the state of the cutting tool during machining process. The obtained results are in good agreement with the previous reported studies [89].

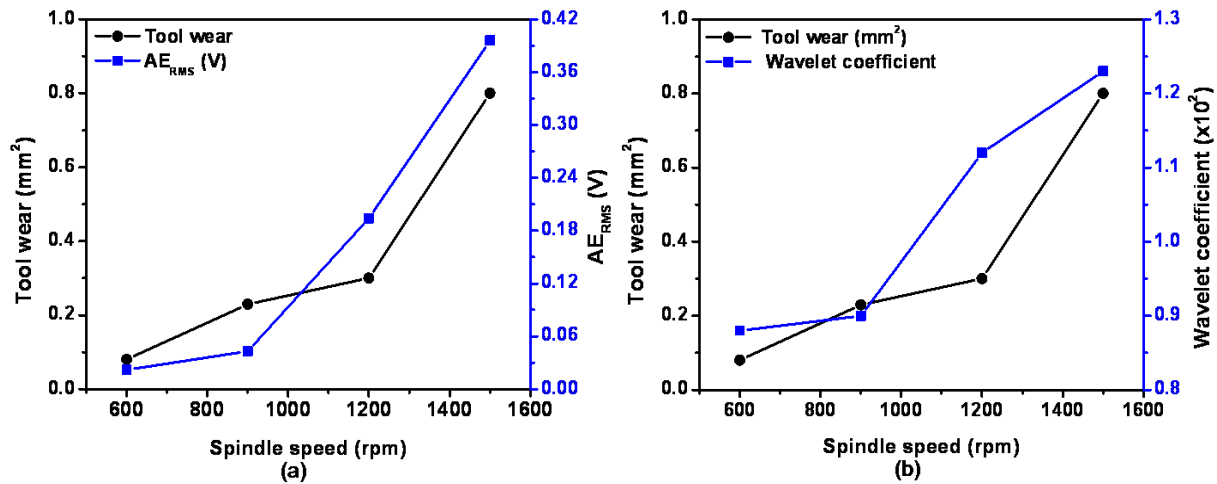


Figure 4. 18 Variation of tool wear and AE parameters with spindle speed: (a) tool wear and AE_{RMS} with spindle speed, and (b) tool wear and wavelet coefficient with spindle speed.

4.4.2 SEM characterization of drilled workpiece surface

Damage in the drilled surface of the workpiece was evaluated using SEM for the drilling conducted at 600 rpm speed and 0.05 mm/rev feed rate; and 1500 rpm speed at 0.25 mm/rev feed rate. The images obtained are shown in Figs. 4.19 (a) and (b). The drilled MMC workpiece was separated in to two parts by using metal cutting machining for surface damage analysis. Rough surface and adhesion of chips in the drilled surface were observed for lower speed and feed rate (Fig. 4.19 a) and this is due to improper evacuation of chips. Matrix crack was also observed due to low speed and feed rate. Figure 4.19 (b) depicts the presence of matrix flow and micro cracks in the drilled surface for drilling conducted at 1500 rpm speed and 0.25 mm/rev feed rate. This is due to high temperature rise in the deformation zone and strain hardening of the composite material. Moreover, crushed B₄C particle was observed in the drilled surface and oxidized white layer was observed due to higher friction between the tool and B₄C particles at 1500 rpm speed and 0.25 mm/rev feed rate. The observed surface damage in the drilled surface of the Al-5%B₄C MMC is similar to the previously reported studies [134].

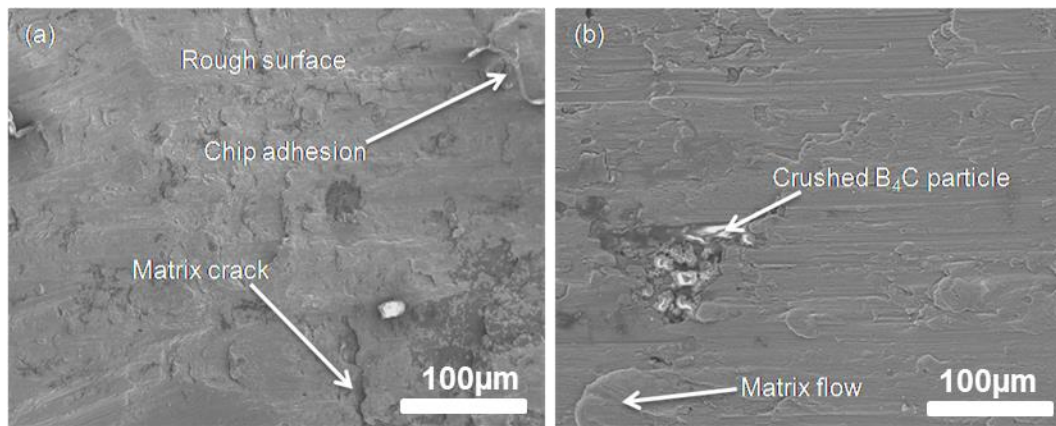


Figure 4. 19 SEM images of drilled workpiece (a) rough surface, chip adhesion and matrix crack for 600 rpm speed at 0.05mm/rev feed rate, and (b) crushed B₄C particle and matrix flow for 1500 rpm speed at 0.25 mm/rev feed rate.

4.5 Summary

Acoustic emission and infrared thermography have been utilized for the characterization of damage mechanisms and heat evolution during drilling of Al-5%B₄C composite under various cutting conditions. The following are the conclusions drawn from this study.

- ❖ The count and amplitude of AE signal show three stages of drilling mechanisms in Al-5%B₄C composite. AE_{RMS} non-linearly increases with spindle speed due to increased strain rate and friction.
- ❖ The FFT spectrum reveals that the predominant peak frequency increases from 227 to 582 kHz. The distribution of low frequency components increases with speed at constant feed rate. The burst type signals become dominant over continuous signals due to matrix cracking and chip collision/ breakage at higher spindle speed.
- ❖ Plastic deformation dominates at stage 1 while matrix cracking, plastic deformation, crack propagation and tool fracture are predominant AE damage sources in stage 2. Frictional source dominates at stage 3. Among all the stages, the decomposed components i.e., D₂, D₃, and D₄ are dominant, and their corresponding to frequency

bands are 62.5-125 kHz, 125-187.5 kHz and 187.5-250 kHz. This is attributed to friction, matrix cracking and plastic deformation.

- ❖ The variation of wavelet energy ratio of decomposed components for different speeds are discussed which explore the rate of friction, tool wear and plastic deformation are increase with an increase in speed.
- ❖ Similar to acoustic emission, temperature line profile also differentiates the drilling process into three stages and tool temperature increases with increasing speed and feed rate.
- ❖ Optical and SEM images are the evidence for different types of wear such as flank wear, tool chipping, adhesion wear and build-up-edge are formed on cutting tool.
- ❖ The quantified tool wear is correlated with AE_{RMS} and wavelet coefficient results. The quantified tool wear increases with an increase in AE_{RMS} and wavelet coefficient. The results are in good agreement with the previous published results.
- ❖ The SEM images confirm material flow, matrix cracking and B_4C particle fracture during the drilling process.

CHAPTER-5

ACOUSTIC EMISSION AND INFRARED THERMOGRAPHY STUDIES IN Al-5%SiC-5%B₄C COMPOSITE

This chapter is directed to study the application of AE and IRT for monitoring drilling process in Al-5%SiC-5%B₄C hybrid composite. AE signals obtained during drilling were analyzed in time, frequency and time-frequency domain. Tool wear was measured using vision measuring microscope and correlated with AE parameters. On the contrary, heat evolution, chip formation mechanism, and temperature rise in cutting tool and workpiece are discussed. The effect of spindle speed and feed rate on AE signal and tool temperature are discussed. The quality of machined surface and damage in the cutting tool are analyzed using scanning electron microscope (SEM).

5.1 Experimental details

The dry drilling experiments were performed on Al-5%SiC-5%B₄C hybrid composite workpiece (70 x 100 x 10 mm³). The feed rate is varied in the range of 0.10-0.40 mm/rev in the interval of 0.05 mm/rev for constant speed (150, 300, and 600 rpm) as shown in Table 5.1. In this chapter, the lower speed and higher feed rate was selected to understand the AE signal characterization and heat evolution at higher strain rate.

Table 5. 1 Conditions for the drilling tests.

Parameters	Cutting conditions
Spindle speed (rpm)	150, 300, 600
Feed rate (mm/rev)	0.10, 0.15, 0.20, 0.25, 0.30, 0.35, 0.40
Drilled depth (mm)	10

5.2 Analysis of acoustic emission signals

5.2.1 Time domain analysis

The acquired AE signals are complex and stochastic in nature due to multiple factors involved in the generation of elastic waves in the drilling process. The obtained AE signals were analyzed and compared with the cutting parameters as well as tool wear. The AE time domain signal shows significant indication of tool wear and chip breaking. The variations of AE count and cumulative count with cutting time for drilling of Al-5%SiC-5%B₄C composite are shown in Fig. 5.1 (a) and 5.1 (b) respectively for 150 rpm speed and 0.10 mm/rev feed rate. The obtained AE count and cumulative count are classified in to three different stages i.e. stage I: initial tool entry, stage II: cutting zone and stage III: tool exit. In the tool entry stage (stage I), the cutting tool first shears the workpiece before the start of cutting. At this stage, the generation of AE counts is very low and approximately constant upto 22 sec due to shear deformation and chip breaking. Whereas in stage II, AE counts increases drastically and is attributed to continuous crack propagation in the workpiece. The tool wear and chip breaking occur in this stage, which emit dense AE wave packets. It is observed from Figs. 5.1 (a) and (b), that stage III reveals decrease in AE count whereas, the cumulative count becomes constant and this is due to tool exit from the workpiece. These three stages are evident for all the feed rates (0.10-0.40 mm/rev) at 150 rpm cutting speed. These three stages of AE generation in the hybrid composite are similar to that generated in the Al-5%SiC and Al-5%B₄C composites discussed in the preceding chapters. All the three stages of AE signal generation during drilling in HMMC are also in good agreement with the previous results reported by Hossein et al. [76].

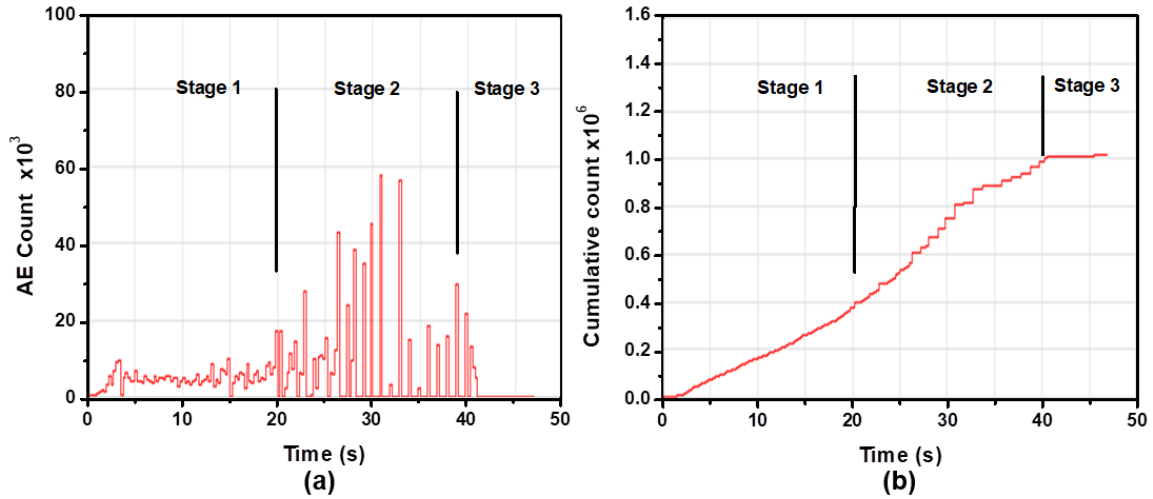


Figure 5. 1 (a) Variation of AE count with time and (b) AE cumulative count with time at constant speed (150 rpm) and feed rate (0.1 mm/rev).

On the other hand, for higher cutting speeds and feed rates, separation of AE count for different stages is difficult due to the overlapping of signals and also decreases in the time of contact between the tool and workpiece. Because of this, cumulative count for each drilled hole is chosen for studying the effect of feed rate on AE at different speeds. AE cumulative count is plotted as a function of feed rate at different spindle speeds and shown in Fig. 5.2 (a). The variation of cumulative count with feed rate follows the same trend as observed in Al-5%SiC and Al-5%B₄C MMCs and decreases with feed rate. At cutting speed 150 rpm, the cumulative count decreases rapidly upto the feed rate of 0.25 mm/rev, and then it shows marginal decrease. For high cutting speeds (300 rpm and 600 rpm), the cumulative count decreases rapidly upto 0.20 mm/rev feed rate and then it is almost constant. The change in the variation of AE cumulative count beyond a certain feed rate (0.25 mm/rev for 150 rpm and 0.20 mm/rev for 300 rpm and 600 rpm) can be attributed to the increase in rubbing/friction and contact pressure between the tool and the workpiece. It is also observed from Fig. 5.2 (a) that the cumulative count decreases with an increase in cutting speed for all the feed rates. The variation of cumulative energy with feed rate is shown in Fig. 5.2 (b) for different speeds.

It is found that cumulative energy also decreases with feed rate for all the cutting speeds (150 rpm, 300 rpm, and 600 rpm). The difference in the magnitude of cumulative energy is lesser than the cumulative count for different cutting speeds. This indicates that AE cumulative count is a better parameter than cumulative energy for differentiating drilling behavior of HMMC for different speeds. The similar trend is observed in the earlier chapters 3 and 4.

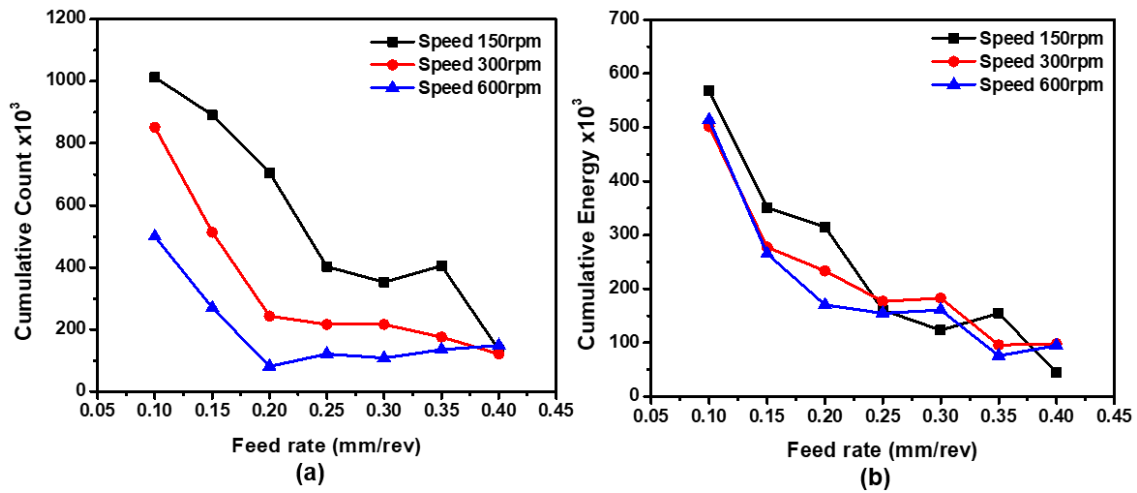


Figure 5. 2 AE parameters with feed rate for different speeds (a) AE cumulative count vs feed rate and (b) cumulative energy vs feed rate.

The AE_{RMS} has been used to study the drilling process in Al-5%SiC and Al-5%B₄C composites. The variation of average AE_{RMS} with cutting speed for different feed rates of hybrid MMC is shown in Fig. 5.3. The AE_{RMS} increases with cutting speed for different feed rates. The obtained results are in good agreement with the earlier results reported by [96, 124].

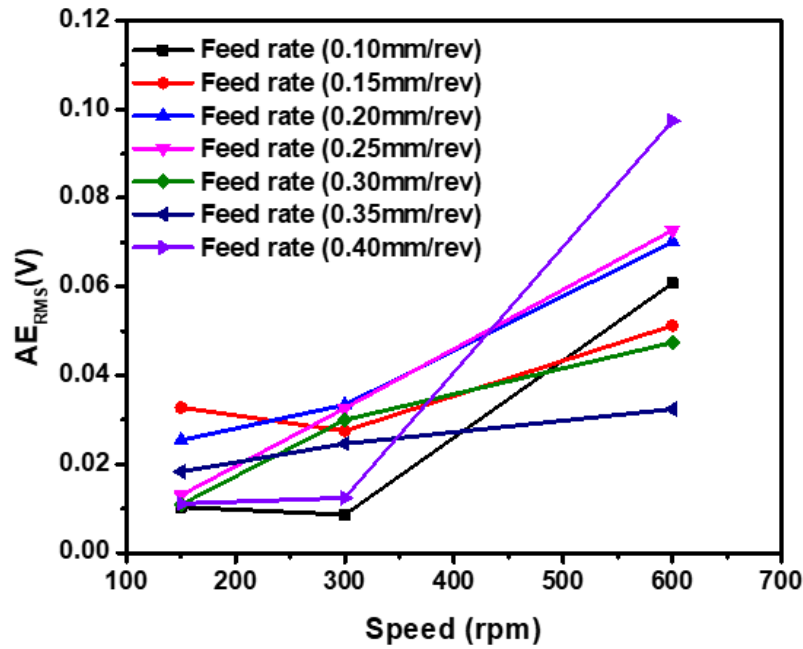


Figure 5. 3 AE_{RMS} with spindle speed at different feed rate.

Figures 5.4 (a) to 5.4 (c) show the amplitude vs time plots for different speeds (150 rpm, 300 rpm and 600 rpm) and constant feed rate (0.1 mm/rev). It is seen from Fig. 5 (a) that many low amplitude signals in the range of 45 dB to 60 dB are generated upto 22 sec (stage I) due to shear deformation. Signals above 60 dB are also generated in stage I and this can be attributed to the chip breaking. In stage II, high amplitude signals are generated in the range from 85 dB to 95 dB due to tool chip-out and chip breaking in addition to cutting. In stage III, the generated signals are found to have the amplitude of around 50 dB and this is due to friction between the tool and the workpiece.

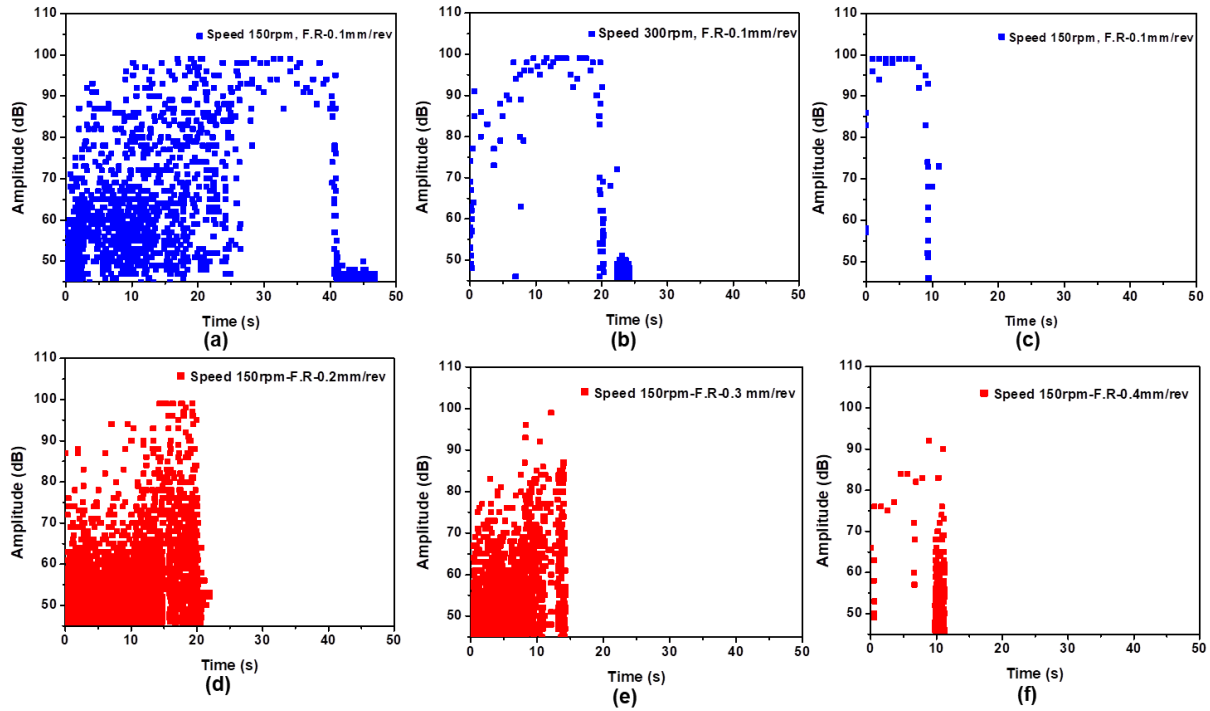


Figure 5. 4 Variation of AE parameters with cutting conditions: (a, b, c) AE amplitude vs time for 150, 300, and 600 rpm speeds and (d, e, f) AE amplitude vs time for 0.2, 0.3, and 0.4 mm/rev feed rates.

The variation of amplitude with time for different feed rate for a constant cutting speed of 150 rpm is shown in Figs. 5.4 (d) to 5.4 (f). The dense low amplitude and higher amplitude signals are dominant with an increase in feed rate due to shear deformation and chip breaking during the drilling.

5.2.2 Frequency domain analysis

The Fast Fourier Transformation (FFT) was used to transform the AE signal from time domain to frequency domain. The obtained waveforms and frequency spectrum of AE signals for different feed rates are shown in Figs. 5.5 (a) to 5.5 (f). Waveforms for determining the dominant frequency were extracted from the signals generated in stage II. It is evident that the dominant frequency decreases with the increase in cutting speed for constant feed rate (0.1 mm/rev). In Figs. 5.5 (a), (c), and (e), arrow marks indicate burst type signals due to

crack propagation and chip breakage, and continuous type signals are due to plastic deformation and friction. The dominant frequency for different feed rates is shown in Fig. 5.6 as a bar chart. It is observed that the dominant frequency increases with increase in feed rate from 546 to 780 kHz for 150 rpm cutting speed which is associated with the generation of the majority of burst signals. The observed predominant frequency mainly originates from crack growth, tool chipping and chip breaking.

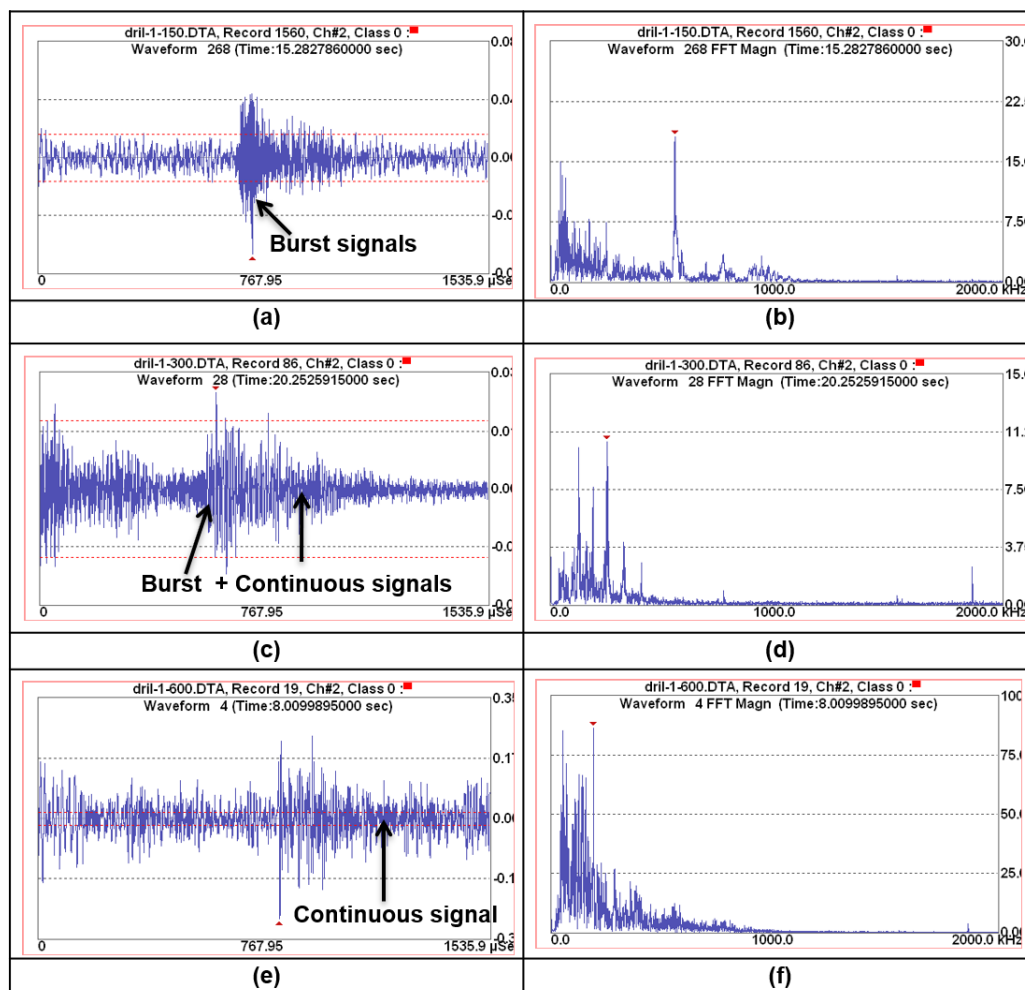


Figure 5. 5 AE parameters with speed for different speeds (a, c, e) AE waveforms vs time and (b, d, f) FFT magnitude vs predominant frequency.

The range of dominant frequency for 300 rpm speed is 52 to 270 kHz and for 600 rpm speed is 47 to 275 kHz. The lower dominant frequency observed in higher cutting speeds is due to the formation of build-up-edge (BUE) on flank face leading to the increase in rubbing/friction

between the tool and workpiece which generates continuous type of AE signals. It is observed that the dominant frequency is very low for the feed rates of 0.2, 0.35 and 0.4 mm/rev at 300 rpm cutting speed (Figure 5.6). It could be possibly due to the presence of porosity in the workpiece which leads to the lack of AE signal generation in the particular drill.

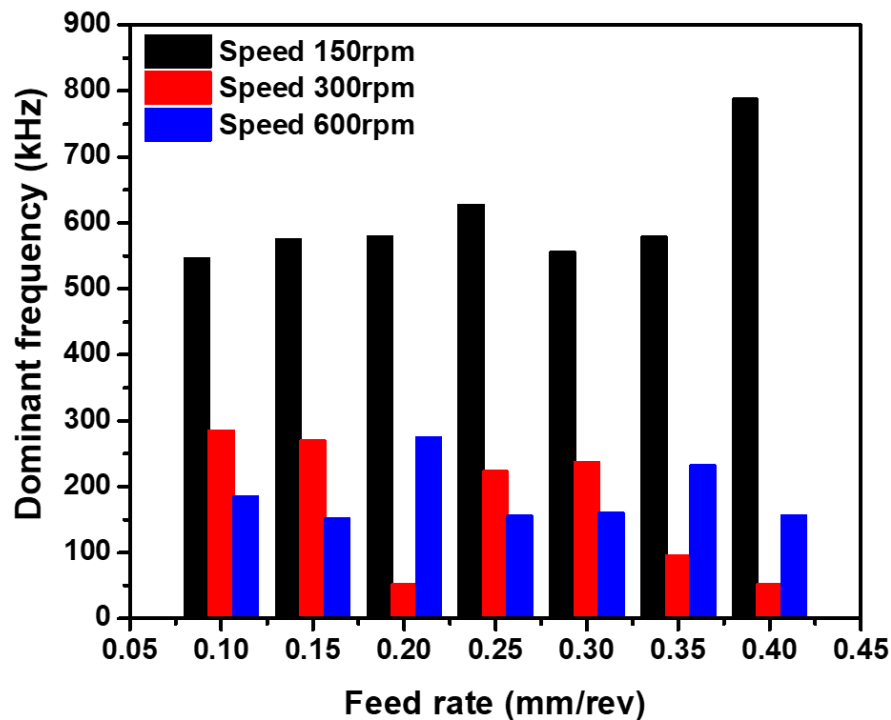


Figure 5. 6 Variation of predominant frequency with feed rate at different speeds.

5.2.3 Time-frequency domain analysis

A large number of waveforms are recorded due to low speed, and feed rates are used in the drilling of Al-5%SiC-5%B₄C composites. For wavelet packet transform analysis, the waveform was selected from the maximum predominant frequency (782 kHz) existing drilled hole (speed of 150 rpm and a feed rate of 0.4 mm/rev). The obtained waveform contains scattered frequency components, as shown in Fig 5.7. WPT is applied to understand the AE source mechanism present the AE signal. The entropy criteria and db-20 mother wavelet were utilized for WPT analysis. The decomposition frequency (1 MHz) was selected based on the

predominant frequency (782 kHz) existing in the signal. The number of levels was set to four ($j=4$), and thus, the number of decomposed components will be sixteen ($i=2^4$) with a frequency interval of 62.5 kHz. The wavelet packet analysis of AE signals for Al-5%SiC composite conducted in chapter 4 was done for the signals generated in stage II, i.e., cutting zone, also similar procedure followed for HMMC. The decomposed frequency components and their associated damage mechanism are tabled in Table. 5.2. From the Table, it is understood that the low-frequency band (D_1 : 0-62.5 kHz) components for 33.12% present in the signals due to environmental noise+friction. The second dominant frequency component D_2 : 62.5-125 kHz is related to matrix cracking with 34.86% of wavelet energy. The third component D_4 : 125-187.5 kHz with 30.28% of wavelet energy is corresponds to plastic deformation. The wavelet energy ratio distinct the predominant AE sources involved in the drilling of HMMC.

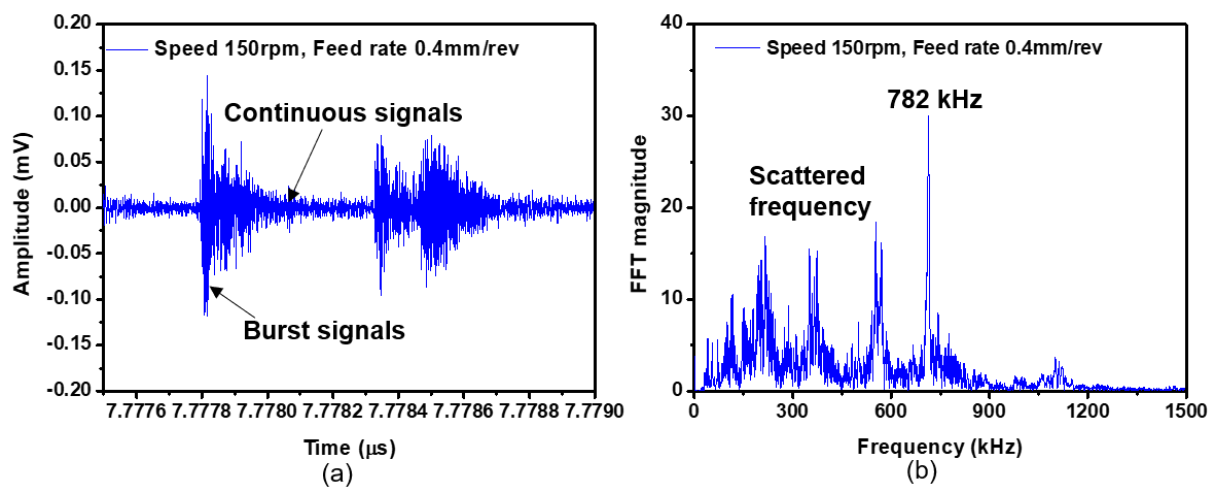


Figure 5. 7 AE signal at 150 rpm speed and 0.4 mm/rev feed rate (a) AE waveform (b) FFT spectrum.

Table 5. 2 Wavelet energy and frequency components of decomposed signals.

Analysis features	WPT decomposed components							
	D ₁	D ₂	D ₃	D ₄	D ₅	D ₆	D ₇	D ₈
Frequency range (kHz)	0-62.5	62.5-125	125-187.5	187.5-250	250-312.5	312.5-375	375-437.5	437.5-500
Energy percentage for AE waveform	33.12	34.86	1.27	30.28	0.01	0.08	0.26	0.07

5.2.4 AE signals and tool wear

Different types of damage were observed in the cutting tool such as tool edge fracture, tool chip out and grooves on chisel edge etc. A vertical microscope was used to measure the HSS tool damage area (i.e., tool wear) and the amount of wear was quantified after each 7 drill holes (i.e., 7 feed rates) for each speed. The measured tool wear and AE parameters (average AE Energy and average AE_{RMS}) are plotted as a function of cutting speed as shown in Figs. 5.8 (a) and 5.8 (b). The observed tool wear after drilling at 7 feed rates and at 150 rpm speed is $49 \mu m^2$. The high tool wear value can be attributed to initial sharp cutting edges of the flank face which cause very rapid damage (at the beginning of the drilling process). For 300 rpm speed, the amount of tool wear is decreased to $38 \mu m^2$ and this is due to the formation of build-up edge on the flank face after 14 drill holes. Whereas, for 600 rpm cutting speed the tool wear value is increased to $60 \mu m^2$ after the drilling of 21 holes which is higher than the values obtained at 150 rpm and 300 rpm. Figure 5.8 (b) shows that the tool wear increases nonlinearly with cutting speed whereas the average AE energy and AE_{RMS} increase linearly with speed. The observed tool wear values are smaller in the Al-5%SiC-5%B₄C composites

than the earlier chapters 3 and 4 (Al-5%SiC and Al-5%B₄C composites) because this chapter 5 focuses on the application of AE and IRT techniques for low speeds and feed rates. The low speed and feed rates produce less wear than the higher speed.

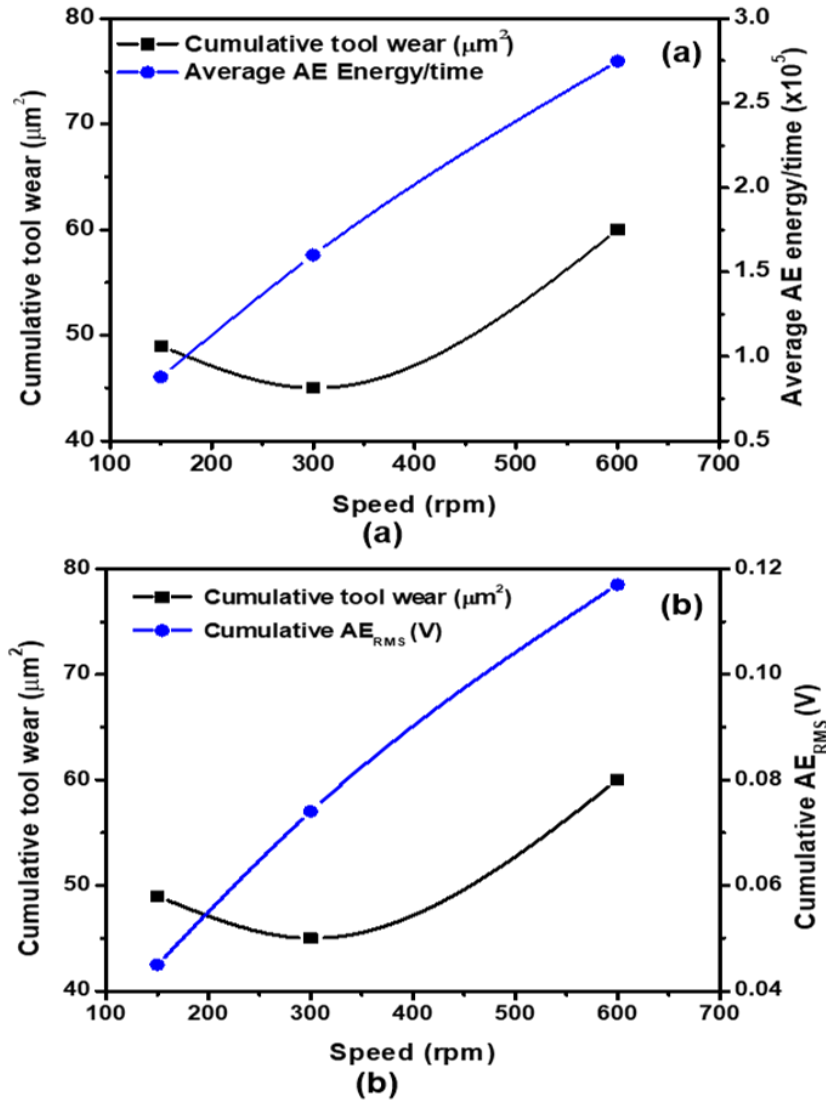


Figure 5. 8 Variation of (a) cumulative tool wear and average AE energy with spindle speed and (b) cumulative tool wear and cumulative AERMS with spindle speed.

5.3 Temperature analysis during drilling of Al-5%SiC-5%B₄C composite

5.3.1 Heat evolution during drilling of HMMC

The tool temperature was determined from the captured IR images for all the cutting conditions. Figure 5.9 shows the variation of maximum tool temperature in the drill hole as a

function of feed rate for different cutting speeds. It is observed from Fig. 5.9 that the maximum temperature increases with increase in both feed rate and cutting speed. The generation of heat is more pronounced with the increase in speed as compared to the feed rate. The maximum temperature is 52.9 °C at 600 rpm speed and 0.4 mm/rev feed rate which is due to high kinetic frictional contact between the tool and workpiece, and discontinuous primary plastic deformation in the workpiece during drilling. The temperature rise in the workpiece affects the chip formation and surface roughness of the drilled specimen.

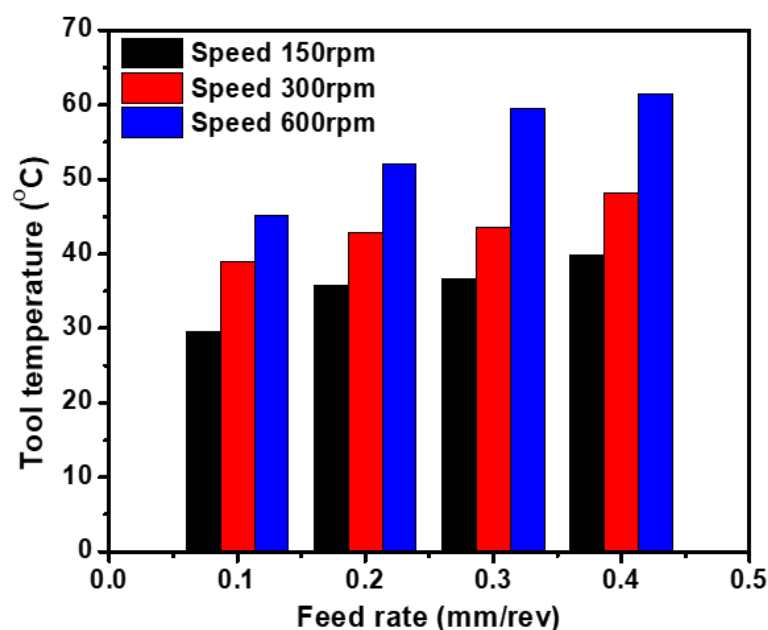


Figure 5. 9 Maximum tool temperature rise with feed rate at different speeds.

5.3.2 Types of chips formation and heat evolution with feed rate

The generation of heat during drilling affects the chip formation mechanism. As already illustrated in the previous chapters, chip formation during drilling is a shear process involving plastic deformation of the workpiece material within the shear zone. Hence, the types of chip formed is not only related to the shear zone temperature, but is also influenced by material properties. The temperature rise in the cutting zone produces different types of chips, such as broken chips, coma chips, helical, conical and saw tooth chips.

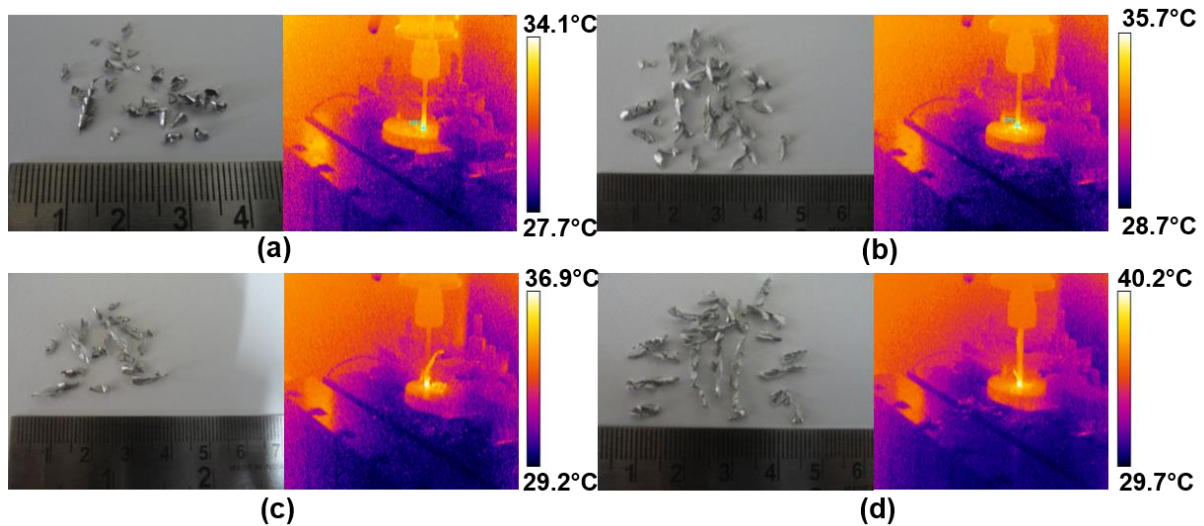


Figure 5. 10 Formation of different types of chips at 150 rpm speed and different feed rates (0.10, 0.20, 0.30 and 0.40 mm/rev) along with IR images.

Different types of chips formed at 150 rpm speed and different feed rates (0.1 to 0.4 mm/rev) along with IR images are shown in Figs. 5.10 (a) to (d). It is observed that with an increase in feed rate, length of chip increases and this is associated with the increase in temperature as revealed by IR thermography images. The broken, conical and helical chips are formed (Fig. 5.10 (a)) at 0.1 mm/rev feed rate because of low strain rate and brittle failure at a lower speed (150 rpm). Figures 5.10 (b) and (c) show the formation of continuous chips at 0.2 and 0.3 mm/rev feed rates and this is due to the increase in strain rate and temperature associated with plastic deformation. The saw-tooth profile kind of chip was noticed at the feed rate of 0.4 mm/rev as shown in Fig. 5.10 (d).

5.4 Detection of tool damage

Figures 5.11 (a) - 5.11 (d) show the optical micrographs of tool damage for different feed rates at various speeds. Figure 5.11 (a) reveals tool chip out and tool edge fracture after 7 drilling tests at 150 rpm speed and different feed rates. This is due to sharp edges of the cutting tool that blunts rapidly at the beginning of cutting. It can be observed from the optical images that the amount of wear increases from the center of the drill bit to the tool corner and

this is due to the increase in peripheral speed of the drill bit during drilling. The fracture occurred on the cutting edge of the tool which is subjected to the highest horizontal and vertical force during drilling. Figures 5.11 (b), (c) and (d) show minimum tool wear due to the deposition of matrix particle on the cutting tool. The different types of tool wear were observed in the earlier chapters 3 and 4 also, but in this chapter, the edge fracture with tool crack observed at 150 rpm speed due to sharp edges of the tool encounter the hard-ceramic reinforcements in the composite may influence tool fracture. Moreover, the large amount of aluminium chip was deposited on the cutting surface due to low speed.

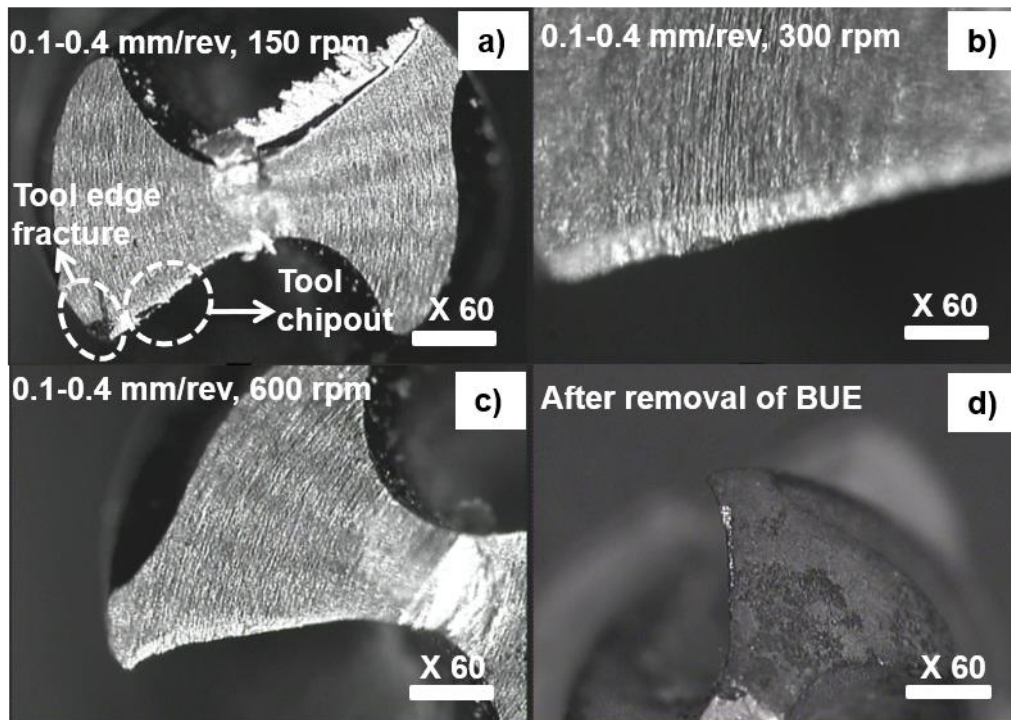


Figure 5. 11 Optical micrograph of tool wear for different feed rates at different speeds: (a) tool fracture, (b) adhesion wear, (c) grooves on chisel edge, and (d) flank wear.

Figures 5.12 (a) and 5.12 (b) show SEM images of the cutting tool. Figure 5.12 (a) shows the image after completion of all the drilling tests whereas Fig. 5.12 (b) shows BUE formation on flank face. The images clearly show that adhesion wear appears on the flank face. The

adherent layer continuously increases with increase in the number of holes and this leads to the accumulation of large amount of the aluminium particles on the cutting edge which influences surface finish of the workpiece and tool life.

The curved surface (due to deformation) and grooves are present on the chisel edge of the cutting tool and is shown in Figs. 5.12 (c) and (d). This is due to high rate of the occurrence of shear/friction between the tool and workpiece at higher cutting speed and feed rate.

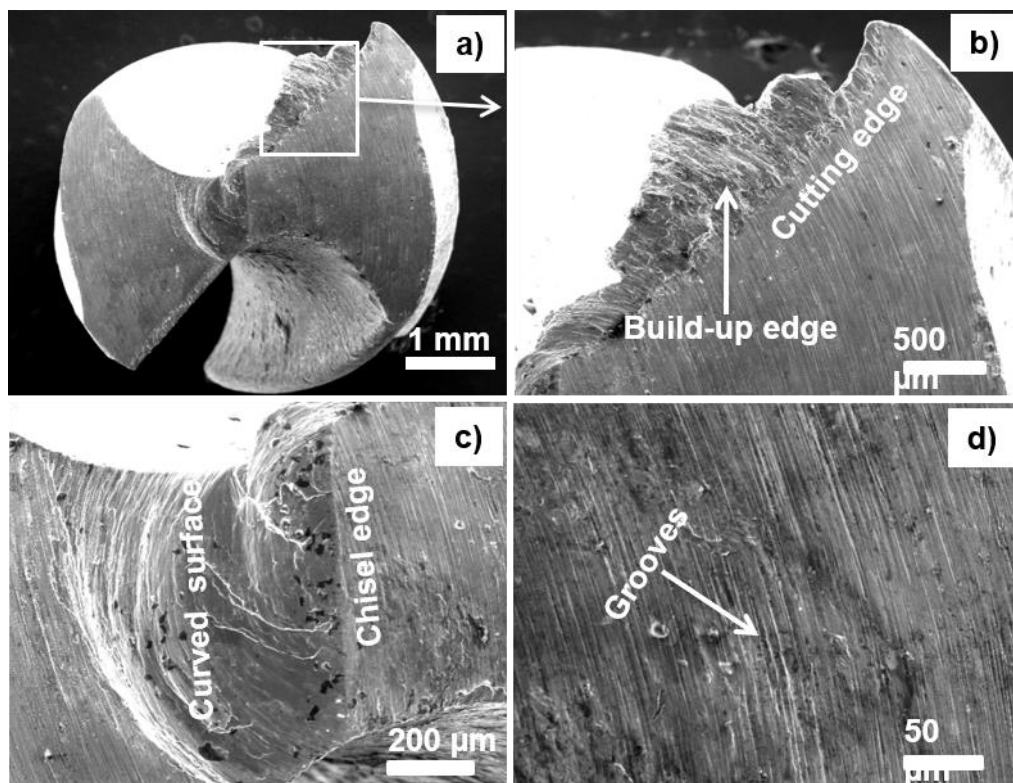


Figure 5. 12 SEM images of the cutting tool (a) after completion of all the drilling tests, (b) build-up-edge formation on flank space, (c) cursed surface in chisel edge and (d) grooves on chisel edge.

The energy dispersive X-ray spectroscopy (EDX) analysis of the cutting tool was also carried out after all the drilling tests. The Figures 5.13 (a)-(b) shows the results of EDX analysis. The EDX result reveals the deposition of aluminum matrix particle on the cutting tool which becomes aluminum oxide (Al_2O_3) due to the generation of heat at the tool and workpiece

interface during drilling. As can be seen from the EDX spectrum (Fig. 5.13 (b)), Carbon (C), Oxygen (O), Silicon (Si) and Iron (Fe) are also present in the cutting tool.

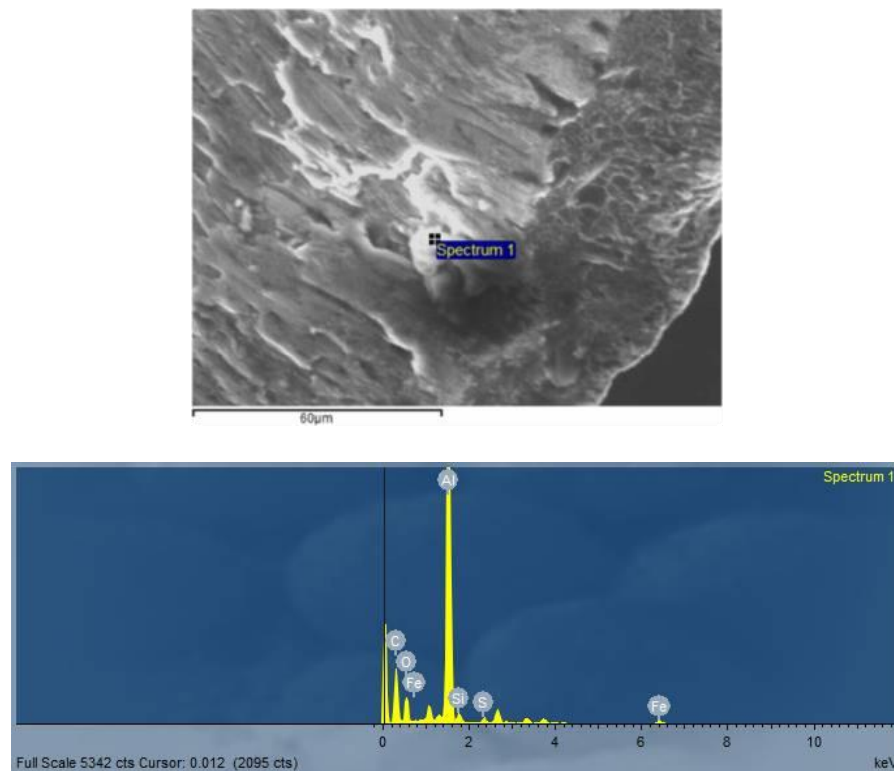


Figure 5. 13 EDX spectrum of cutting tool after all the drilling test (a) adhesion of Al particle on flank face (b) EDX spectrum of Al particle.

5.5 Characterization of drilled surface

The drilled specimen was separated into two equal parts after all the tests and then the surfaces were examined by using SEM. The specimen was subjected to drilling tests at the feed rates of 0.1, 0.2, 0.3, and 0.4 mm/rev for 150 rpm speed. Figures 5.14 (a) and 5.14 (b) clearly show the broken chip which is trapped between the tool and the workpiece for 0.1 mm/rev feed rate at 150 rpm speed. The BUE formed on the cutting tool leads to scratches and wear debris in the drilled hole (at feed rate 0.2 mm/rev) as shown in Figs. 5.14 (c) and (d). Figures 5.14 (e) and 5.14 (f) show the occurrence of plastic flow on the drilled surface due to deformation. The crushed particles on the drilled surface are observed at 0.4 mm/rev feed rate

due to higher contact pressure and shear deformation in the drill as shown in Figs 5.14 (g) and (h).

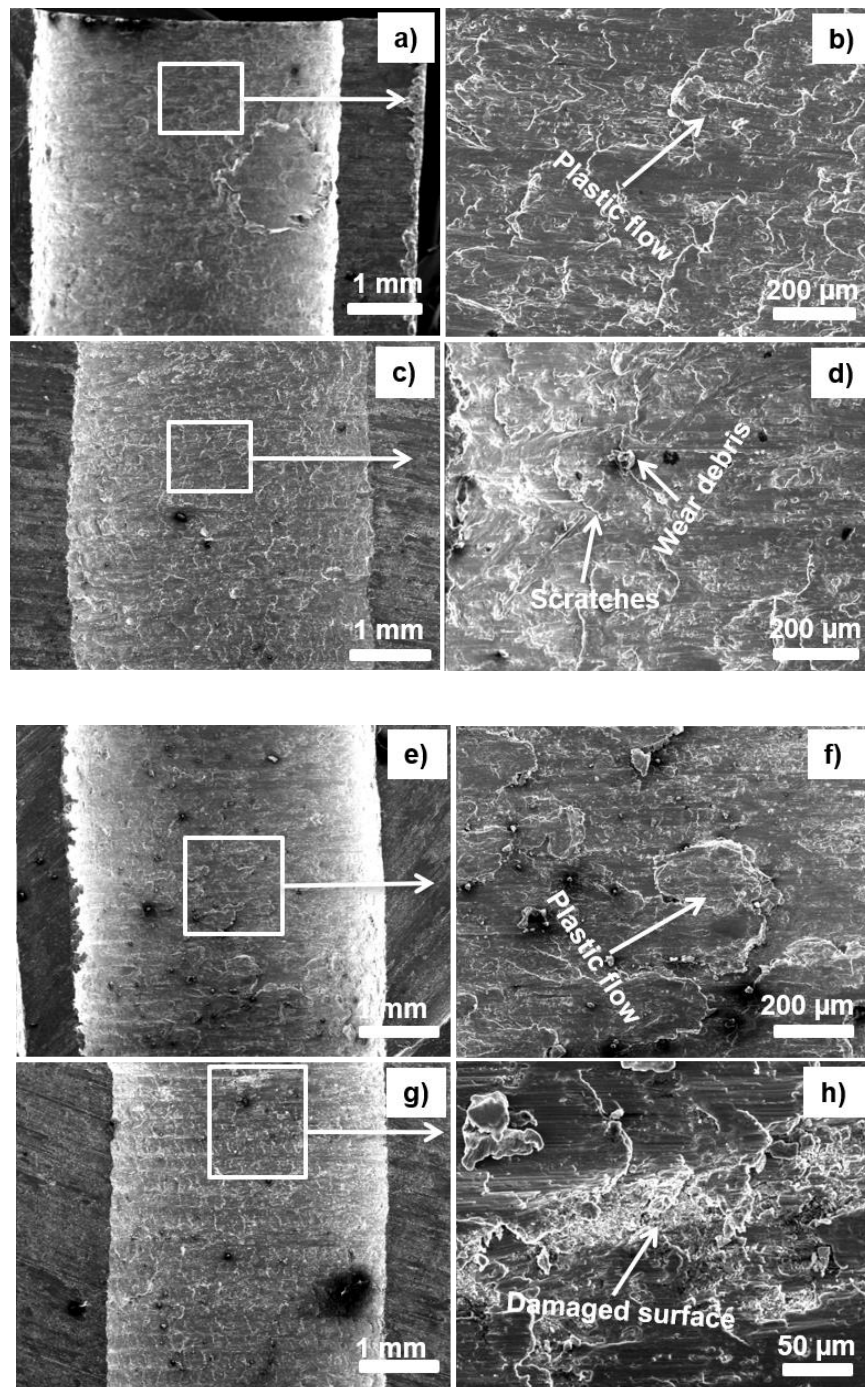

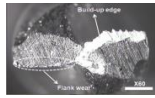
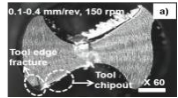
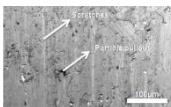
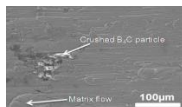
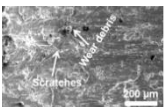


Figure 5. 14 SEM images of workpiece surface for drilling at different feed rates (0.10, 0.20, 0.30, and 0.4 mm/rev) at constant speed 150 rpm: (a and b) plastic flow, (c and d) wear debris (e and f) plastic flow, and (g and h) crushed particles.

5.6 Comparison AE signal characteristics, tool temperature rise and tool wear for all three MMCs.

The analyzed AE signal features, tool temperature rise, tool and workpiece damages are compared for all three MMCs as shown in the Table 5.3. The optical microscope and SEM characterization confirm the various damages feature presence in the cutting tool and workpiece are also compared.

Table 5. 3 Comparison of AE signal, temperature rise and tool wear characteristics during drilling of MMCs.

Techniques	Effective parameters	Al-5%SiC composite	Al-5%B ₄ C composite	Al-5%SiC-5%B ₄ C composite
AE	AE count and energy	Decrease	Decrease	Decrease
	AE _{RMS}	Increase	Increase	Increase
	Predominant frequency	510 kHz	550 kHz	782 kHz
	Dominant components and energy percentage	D ₁ , D ₂ and D ₄	D ₂ , D ₃ and D ₄	D ₁ , D ₂ and D ₄
IRT	Tool temperature	Linearly increase	Linearly increase	Linearly increase
VMM	Quantification of tool wear	Edge wear and chisel edge damage 	Flank wear and Build-up-edge 	Tool edge fracture tool chipping 
SEM	Types of workpiece damages	Particle pullout and scratches 	Crushed particles and matrix flow 	Wear debris and scratches 

The AE time domain parameters such as counts, energy and AE_{RMS} are correlated with cutting conditions (speed and feed rate) for all three MMCs. The AE counts and energy decreases with an increase in feed rate at a different speed. The reason may be due to the decrease in time of contact between the tool and workpiece. AE_{RMS} increases with an increase in tool wear at spindle speed for all the MMCs due to increase in friction and strain rate. The predominant frequency (510, 550 and 782 kHz) of MMCs show increasing trend the reason may be due to an increase in the hardness of the composites. WPT decompose the AE signals into several components and is converted into the FFT spectrum. Further, the wavelet energy percentage (EPC) for each decomposed component is determined. The frequency band of the decomposed components, EPC value and their associated damage mechanisms are identified. The D_1 : 49.49%, D_2 : 43.02%, and D_4 : 7.33% are the major energy components and their associated damage features such as friction, matrix cracking and plastic deformation in the drilling of Al-5%SiC composite. The decomposed components D_2 : 32.66% (friction), D_3 : 30.91% (matrix cracking), D_4 : 19.48% (plastic deformation) and D_7 : 4.40% (tool and particle fracture) are the major sources of AE signals in the drilling of Al-5%B₄C composite while D_1 : 33.12% friction, D_2 : 34.86% matrix cracking, D_4 : 30.28% plastic deformation and is the significant sources in the drilling of Al-5%SiC-5%B₄C composite. The energy percentage of D_7 : 0.004% component is almost zero in the Al-5%SiC-5%B₄C composite while Al-5%B₄C composite is D_7 : 4.40%, the reason may be due to formation of build-up-edge leads to lower tool wear values. Tool temperature linearly increases with an increase in the speed and feed rate for all three MMCs. From the WPT results, it is understood that three damage mechanisms dominant sources (friction, matrix cracking and plastic deformation) for AE signals generation in the drilling of MMCs. Different types of tool and workpiece damages are characterized using an optical microscope and SEM for all three MMCs.

5.7 Summary

The present study shows that acoustic emission and infrared thermography techniques are efficient to capture significant issues i.e., tool wear, chip formation and damages during drilling of Al-5%SiC-5%B₄C hybrid metal matrix composite. Major conclusions are as follows:

- ❖ AE signals generated during drilling can be classified into three stages namely tool entry, cutting zone and tool exit. The constant magnitude of AE counts upto 22 sec represents the tool entry stage due to shear deformation and chip breaking. The dense AE count emitted in the cutting zone is due to continuous crack propagation and chip breaking. In the tool exit stage, AE count decreases and the source of AE is only friction.
- ❖ Stage I of drilling is represented by very low count and low amplitude (45 dB - 60 dB) signals. Stage II corresponds to high count and high peak amplitude (> 80 dB) signals. Stage III is represented by reduced count and low amplitude signals.
- ❖ Cumulative AE count and cumulative AE energy decrease with increase in feed rate due to decrease in the time of contact between the tool and workpiece. The AE parameters (AE_{RMS} and AE energy) increase linearly and tool wear increases non-linearly with speed.
- ❖ Time-frequency component analysis distinguishes the AE source mechanisms involved in the drilling of HMMC. The wavelet energy percentage of D₁ (33.12%), D₂ (34.86%) and D₄ (30.28%) components carry the majority of wavelet energy percentage and corresponding damage mechanisms are noise + friction, matrix cracking and plastic deformation.

- ❖ The workpiece temperature (27.7 °C to 52.9 °C) increases with an increase in speed and feed rate. The rise in temperature is attributed to the discontinuous plastic deformation and kinetic frictional contact between the tool and workpiece during drilling.
- ❖ The optical and SEM examinations confirm tool damage (tool edge fracture, tool chipping) and formation of BUE on the cutting edge.
- ❖ The obtained results of AE, IRT, optical and SEM for all three MMCs are tabulated and the overall outcomes of each techniques are compared with the MMCs.

CHAPTER – 6

DISCUSSION, CONCLUSIONS, SCIENTIFIC CONTRIBUTIONS AND FUTURE DIRECTIONS

6.1 Discussion

- The time-domain parameters, i.e., AE counts and amplitude has successfully distinguished the drilling process into three stages such as tool entry, cutting zone and tool exit for all the MMCs. AE_{RMS} non-linearly increases with spindle speed at feed rate due to increased strain rate. The results are concomitant with earlier reported work.
- The peak frequency shift increases with an increase in speed at different point angle tool for the drilling of Al-5%SiC composite due to effect of different point angle tools. However, the peak frequency shift for Al-5%B₄C and Al-5%SiC-5%B₄C decreases with an increase in speed due to an increase in friction between the tool and workpiece.
- Time-frequency domain analysis was carried to understand the predominant frequency component existent time. The normalized amplitude, frequency and time plot has been carried out to understand the predominant frequency components at different drilling time.
- The wavelet packet transform (WPT) approach has been proposed to differentiate the damage mechanisms involved in the drilling process by decomposing the AE signals into approximate and detail components. Also, the energy percentage of decomposed components and the range of frequency band represents various damage mechanisms present in the drilling process. The application of WPT for AE signals analysis during the drilling of MMCs is performed for the first time.

- Heat evolution during the drilling of MMCs has been studied, and different stages of the drilling process are differentiated with the temperature profile. The measured tool temperature increases with an increase in speed due to an increase in kinetic friction contact between the tool and workpiece.
- The SEM micrographs confirm the different forms of tool wear such as abrasive wear, adhesive wear, tool chipping and BUE formation in the cutting edges. The SEM image confirms the presence of scratches, particle pullout, plastic flow and cracks on the drilled surface. Further, SEM has been utilized to investigate the different types of chip formation mechanisms and their characteristics (cracks, folding, shear band and flanks) in the composite chips.

6.2 Conclusions

The significant conclusions drawn from the thesis are as follows:

- ✓ The AE time-domain parameters differentiate the drilling process into three stages. The AE parameters are correlated with the cutting conditions.
- ✓ The FFT has been implemented on the AE signals to determine the fundamental frequency components present in the AE signals and the variation of predominant frequency components with cutting conditions.
- ✓ The continuous wavelet transform (CWT) has employed to find the predominant frequency component and frequency distribution existent time in the AE signals. Also, the wavelet coefficient has been extracted from the CWT spectrum and correlated with the tool wear for Al-5%SiC and Al-5%B₄C composites.
- ✓ The various damage mechanisms involved in the drilling of MMCs have been characterized using the WPT approach.
- ✓ The temperature profile reveals three stages of the drilling process and its inherent heat evolution during the drilling operations. The maximum tool temperature rise (103 °C) is

observed for 1500 rpm speed in case of Al-5%B₄C composite. The obtained tool and workpiece temperature increase with an increase in speed due to an increase in plastic deformation, and kinetic frictional contact between the tool and workpiece.

- ✓ The heat distribution in the workpiece has been studied using COMSOL model, and the experimental value has been correlated with simulated temperature in the drilling of Al-5%SiC and Al-5%B₄C composites.
- ✓ The most influential factor for tool temperature and surface roughness has been determined using the ANOVA model for the drilling of Al-5%SiC composite. The results show that the drill bit point angle 90° and cutting speed are the more significant factors for tool temperature, whereas feed rate and point angle are the most influential factors for surface roughness.
- ✓ The amount of tool wear has been quantified and compared with AE signal features such as AE count, AERMS, cumulative energy and wavelet coefficient. It is understood that the AERMS and wavelet coefficient sensitive factors for the tool wear during drilling of MMCs.
- ✓ The different forms of tool wear and workpiece damage has been confirmed by SEM micrographs.

6.3 Scientific contributions

The major scientific contributions of the dissertation are given as follows:

- ❖ The tool wear mechanism during drilling of Al-5%SiC, Al-5%B₄C, and Al-5%SiC-5%B₄C composites has been identified through better correlation of AERMS, cumulative energy of AE time domain parameters.
- ❖ Implementation of Wavelet packet transform approach on AE signals has achieved better distinguishability between the various damage mechanism such as friction, matrix cracking, plastic deformation, chip breaking, and tool wear in MMCs.

- ❖ The proposed parameter wavelet energy ratio promises better characterization of AE source from various damage mechanisms in MMCs, as first of its kind. The evaluation of the proposed parameter for speed ranges from 600 rpm to 1500 rpm has successfully established a better understanding of the energy distribution of the mechanism and its dominance at each stage of drilling.
- ❖ The signal characterization of the WPT approach is well correlated with the micrographs of tool and workpieces.
- ❖ The identification of the dynamic damage mechanism of the WPT approach in MMCs has promised its sensitivity compared with the well-established measurement on tool temperature through IRT and AE count parameter.

6.4 Future directions

It is well known that systematic experimentation, calibration, modelling, and simulation are the keys factors to the successful development of science and technology. The present thesis has significantly contributed to gaining newer insights into AE source mechanisms and heat evolution during the drilling of MMCs. However, there is still scope for further research work. The possible future directions can be explored as follows:

- The WPT can be extended to investigate the tool wear and damage mechanisms in carbide coated and diamond coated tools using AE and IRT techniques.
- Implementing WPT in ANN approach enhances the prediction rate and provides more insight into the relationship between AE parameters and tool wear during drilling of various hardness MMCs.
- Automated self-learning of processing approach can be extended by the use of machine learning improves the evaluation of the damage mechanism of MMCs.

- Inclusion of shear force and friction force in FEM analysis enhances the accuracy in prediction of tool and workpiece interface temperature.
- Microstructural studies using back scattered electron diffraction (EBSD) and transmission electron microscope (TEM) can be used to study the machining induced adiabatic shear band formation in chips, plastic deformation, and plastic flow in the workpiece and damage in the cutting tool during the drilling of MMCs.

REFERENCES

- [1] P. J. Shull, *Nondestructive Evaluation: Theory, Techniques, and Applications*, CRC Press, 2002.
- [2] R. Baldev, T. Jayakumar and M. Thavasimuthu, *Practical Non-Destructive Testing*, 3rd edition, Alpha Science International Ltd, 2007.
- [3] R. Baldev, C. V. Subramanian and T. Jayakumar, *Non-destructive Testing of Welds*, New Delhi, Woodhead publications, 2000.
- [4] Robert C. Memaster, *Non-destructive testing handbook*, American Society for Nondestructive testing, 1st edition, 1959.
- [5] R. Baldev, T. Jayakumar and B. P. C. Rao, Review of NDT techniques for structural integrity, in Sadhana, New Delhi, In academy of proceedings in engineering sciences, pp. 5-38, 1995.
- [6] D. E. Bray and R. K. Stanley, *Non-destructive Evaluation*, Revised edition, CRC Press, Florida, 1997.
- [7] S. Bagavathiappan, B. B. Lahiri, T. Saravanan, John Philip, T. Jayakumar, Infrared thermography for condition monitoring-A review, *Infrared. Phys. Technol*, vol. 60, pp. 35-55, 2013.
- [8] H. A. Kishawy, H. Hegab, U. Umer, Mohany, Application of acoustic emission in machining process: analysis and critical review, *Int. J. Adv. Manuf. Technol*, vol. 98, pp. 1391-1407, 2018.
- [9] R. Teti, K. Jemielniak, G. O'Donnellc, and D. Dornfeld, Advanced monitoring of machining operations. *CIRP. Ann. manuf. techno*, vol. 59 (2), pp. 717-739, 2010.
- [10] Peter Tavner, Li Ran, Jim Penman, Howard Sedding, *Condition Monitoring of Rotating Electrical Machines*, The Institute of Engineering and Technology, London, United Kingdom, 2008.
- [11] B. K. N. Rao, Condition monitoring and the integrity of industrial systems, A. Davies (Ed.), *Handbook of Condition Monitoring: Techniques and Methodologies*, Chapman & Hall, London, United Kingdom, 1998.
- [12] M. C. Eti, S. O. T. Ogaji, S. D. Probert, Reducing the cost of preventive maintenance (PM) through adopting a proactive reliability-focused culture, *App. Ener*, vol. 83, pp. 1235-1248, 2006.

- [13] P. A. Bragatto, P. Pittiglio, S. Ansaldi, The management of mechanical integrity inspections at small-sized “Seveso” facilities, *Relia. Eng. and Sys. Saft*, vol. 94, 412-417, 2009.
- [14] Charles R. Farrar and Keith Worden, An introduction to structural health monitoring, *Philo. Trans. of the Roy. Soci A*, vol. 365, pp. 303-315, 2006.
- [15] H. K. Tonshoff, and J. P. Wulfsberg, Developments and Trends in Monitoring and Control of Machining Processes, *Annals. of the CIRP*, vol. 37(2), pp. 611-622, 1988.
- [16] R. L. Kegg, Online machine and process diagnostics, *CIRP Ann*, vol. 32, pp. 469-473, 1984.
- [17] Deepam Goyal, B. S. Pabla, Condition based maintenance of machine tools-A review, *CIRP J. of Manuf. Sci. and Techno.*, vol. 10, pp. 24-35, 2015.
- [18] P. M. Lister and G. Barrow, Tool Condition Monitoring Systems, *Proceedings of the Twenty-Sixth International Machine Tool Design and Research Conference*, pp. 271-288, 1986.
- [19] Y. Koren, and A.G. Ulsoy, Adaptive Control in Machining, in the *Metals Handbook: Machining*, J. R. Davis (ed.), Volume 16, 9th Edition, ASM Int., Metals Park, OH, pp. 618-626, 1989.
- [20] E. Dimla and Dimla Snr, Sensor signals for tool-wear monitoring in metal cutting operations-a review of methods, *Int. J. Mach. Tools Manuf.*, vol. 40 (8), pp.1073-1098, 2000.
- [21] Lihui Wang and Robert X. Gao, *Condition Monitoring and Control for Intelligent Manufacturing*, Springer Series in Advanced Manufacturing, ISBN-10: 1846282683, 2006.
- [22] Viktor P. Astakhov, *Drills Science and Technology of Advanced Operations*, Chapter 2, 2014.
- [23] Nitin Ambhore, Dinesh Kamble, Satish Chinchankar, and Vishal Wayal, Tool condition monitoring system-A review, *Mater. Today: Proc.*, vol. 2, pp. 3419-3428, 2015.
- [24] D. E. Dimla Sensor signals for tool-wear monitoring in metal cutting operations-a review of methods, *Int. J. Mach. Tools Manuf.*, vol. 40, pp.1073-1098, 2000.
- [25] G. Byrne, D. Dornfeld, I. Inasaki, G. Ketteler, W. König, R. Teti, Tool condition monitoring (TCM)-the status of research and industrial application, *CIRP Ann ManufTechnol*, vol. 44, pp. 541-567, 1995.

- [26] Y. Zhou, W. Xue, Review of tool condition monitoring methods in milling processes, *Int. J. Adv. Manuf. Technol.*, pp. 1-15, 2018.
- [27] Y. Altintas, In-process detection of tool breakages using time series monitoring of cutting forces, *International Journal of Machine Tools and Manufacture* 28 (2), 157-172, 1988.
- [28] Bernhard Sick, Review: on-line and indirect tool wear monitoring in turning with artificial neural networks: a review of more than a decade of research, *Mechanical Systems and Signal Processing*, vol. 16 (4), 487-546, 2002.
- [29] S. Li, M.A. Elbestawi, Fuzzy clustering for automated tool condition monitoring in machining, *Mechanical Systems and Signal Processing*, vol. 10 (5), 533-550, 1996.
- [30] Huseyin Metin Ertunc, Cuneyt Oysu, Drill wear monitoring using cutting force signals, *Mechatronics*, vol.14, 533-548, 2004.
- [31] T. Mohanraj, S. Shankar, R. Rajasekar, N. R. Sakthivel and A. Pramanik, Tool condition monitoring techniques in milling process - a review, vol. 9 (1), pp.1032-1042, 2020.
- [32] A. V. Atli, O. Urhan, S. Ertürk, M. Sönmez, A computer vision-based fast approach to drilling tool condition monitoring, *Proc. Inst. Mech. Eng. B. J. Eng. Manuf.*, vol.220, pp.1409-1415, 2006.
- [33] R. Lev, A. Villa, O. Quagha, R. Chiaa and G. Rurellt, An expert control system for tool life management in flexible manufacturing cells, *Ann. CIRP*, vol. 34, pp. 87-90, 1985.
- [34] Avinash A. Thakre, V. Aniruddha Lad, and Kiran Mala, Measurements of Tool Wear Parameters Using Machine Vision System, Model, and Simul. in Eng., pp.1-9, 2019.
- [35] G. Xiong, J. Liu, and A. Avila, Cutting tool wear measurement by using active contour model-based image processing, in *Proceedings of 2011 International Conference on Mechatronics and Automation (ICMA)*, pp. 670-675, IEEE, Beijing, China, 2011.
- [36] F. Giusti and M. Santoc, Development of a fibre optic sensor for in process measurement of tool flank wear, *Proc. 20th Int. Machine Tool Design and Research Conf.*, pp.351-360, 1979.
- [37] K. N. Prasad, B. Ramamoorthy, Tool wear evaluation by stereo vision and prediction by artificial neural network, *J. Mater. Process. Technol.*, vol. 112 (1), pp. 43-52, 2001.
- [38] T. M. Hunt, *Handbook of wear debris analysis and particle detection in liquids*, Elsevier, Essex, England, 1993.
- [39] B. J. Roylance and S. Raadnui, The morphological attributes of wear particles-their role in identifying wear mechanisms, *Wear*, vol. 175, vol. 1-2, pp. 115-121, 1994.

- [40] B. H. T. Baharudin, N. Dimou, K. K. B. Hon, Tool Wear Behaviour of Micro-Tools in High Speed CNC Machining. In: Hinduja S. (eds) Proceedings of the 34th International Matador Conference, London, 2004.
- [41] N. H. Cook and K. Submanian, Micro-isotope tool wear sensor, Ann. CIRP, vol. 27, pp. 73-78, 1978.
- [42] B. Ivkovic, Application of thin layer activation to measuring tool wear in metal cutting, Tribol Int., vol. 3-8, 1982.
- [43] K. Vacharanukul, and S. Mekid, In-process dimensional inspection sensors. Measurement, vol. 38, pp. 204-218, 2005.
- [44] J. L. El Gomyel and K. D. Bregger, On-line tool wear sensing for turning operations, Journal of industrial engineering, vol.106, pp. 44-47, 1986.
- [45] S. C. Lin, C. J. Ting, Tool wear monitoring in drilling using force signals. Wear, vol. 180 (1-2) pp. 53-60, 1995.
- [46] M. A. Elbestawi, T. A. Papazafiriou, and R. X. Du, In-process monitoring of tool wear in milling using cutting force signature, Int. J. Mach. Tools Manuf., vol. 31 (1), pp. 55-73, 1991.
- [47] S. K. Choudhury and K. K. Kishore, Tool wear measurement in turning using force ratio, Int. J. Mach. Tools Manuf., vol. 40 (6), pp. 899-909, 2000.
- [48] Ekkard Brinksmeier, Werner Preuss, Oltmann Riemer, Rüdiger Rentsch, Cutting forces, tool wear and surface finish in high speed diamond machining, Prec. Eng., vol. 49, pp. 293-304, 2017.
- [49] J. Tlustý and G. C. Andrews, A critical review of sensors for unmanned machining, Ann. CIRP, vol. 32, pp. 563-572, 1983.
- [50] A. Rehorn, J. Jiang, and P. Orban, State-of-the-art methods and results in tool condition monitoring: a review, Int. J. Adv. Manuf. Technol., vol. 26, pp. 693-710, 2005.
- [51] M. S. H. Bhuiyan and Imtiaz Ahmed Choudhury, Investigation of Tool Wear and Surface Finish by Analyzing Vibration Signals in Turning Assab-705 Steel, J. Mach. Sci. and Tech. an Int. J., vol.19 (2), 2015.
- [52] S. M. Pandit and S. Issov, A data dependent systems strategy of on-line tool wear sensing. J. Engng, Ind., vol. 104, pp. 217-223, 1982.
- [53] D. Dimla Snr, The Correlation of Vibration Signal Features to Cutting Tool Wear in a Metal Turning Operation. Int. J. Adv. Manuf. Technol., vol. 19, pp. 705-713, 2002.

- [54] R. K. Miller, Acoustic Emission Testing, Non-destructive Testing Handbook, 3rd ed. Vol. 6, Columbus, OH: Amer. Society for Non-Destructive Testing, 2006.
- [55] G. A. Washer, Developments for the non-destructive evaluation of highway bridges in the USA, NDT & E Int., vol. 31, pp. 245-249, 1998.
- [56] V. M. Malhotra and N. J Carino, Handbook on non-destructive testing of concrete, CRC Press, LLC, Boca Raton, FL, 2004.
- [57] Thodamra Kandy Haneef, Barid Baran Lahiri, Subramaniam Bagavathiappan, Chandan Kumar Mukhopadhyay, John Philip, Bhagi Purna Chandra Rao and Tamanna Jayakumar, Study of the tensile behavior of AISI type 316 stainless steel using acoustic emission and infrared thermography techniques, J of Mat. Res. and Tech., vol. 4, pp. 241-253, 2015.
- [58] Gongtian Shen, Zhanwen Wu and Junjiao Zhang, Advances in acoustic emission technology, Springer Proceedings in Physics, vol. 179, pp. 257-258, 2015.
- [59] Ozevin, Didem and James Harding, Novel leak localization in pressurized pipeline networks using acoustic emission and geometric connectivity, Int. J. of Pres. Vess. and Pip., vol. 92, pp. 63-69, 2012.
- [60] K. E. Mohamed, Batanouny, Paul H. Zieh, Aaron Larosche, Jesé Mangual, Fabio Matta and Antonio Nanni, Acoustic emission monitoring for assessment of prestressed concrete beams, Const. and Buil. Mat., vol. 58, pp. 46-53, 2014.
- [61] David Crivelli and Stewart Bland, Structural health monitoring via acoustic emission, J. of Rein. Plas., vol. 60, pp. 390-392, 2015.
- [62] Al-Obaidi, S. M. A. Leong, M. S. Hamzah, and A. M. Abdelrhman, A Review of Acoustic Emission Technique for Machinery Condition Monitoring: Defects Detection and Diagnostic. App. Mech. and Mat., vol. 229-231, pp. 1476-1480, 2012.
- [63] Lihui Wang and Robert X. Gao, Condition Monitoring and Control for Intelligent Manufacturing, Springer Series in Advanced Manufacturing, ISSN 1860-5168, 2005.
- [64] Xiaoli Li, A brief review on acoustic emission method for tool wear monitoring during turning. Int. J. Mach. and Tools Manufact., vol. 42, pp. 157-165, 2002
- [65] Mahindra Kaphle, Analysis of acoustic emission data for accurate damage assessment for structural health monitoring applications, Ph.D. Thesis, School of chemistry, Queensland University of Technology, Australia, 2012.
- [66] David Roylance, <http://web.mit.edu/course/3/3.11/www/modules/ss.pdf>, 2001.

- [67] Jianan Hu Alan and C. F. Cocks, A multi-scale self-consistent model describing the lattice deformation in austenitic stainless steels, *Int. J. of Sol. and Str.*, vol. 78-79, pp. 21-37, 2016.
- [68] A. V. Lavrov, and V. L. Shkuratnik, Deformation and fracture-induced acoustic emission in rocks, *Acous. Phys.*, vol. 51, pp. S2-S11, 2005.
- [69] The Collaboration for NDT Education. (n.d.). Theory - AE Sources. Retrieved August 10, 2010, Available from NDT Education Resource Center: 163 http://www.ndt-ed.org/EducationResources/CommunityCollege/OtherMethods/AE/AE_TheorySources.htm
- [70] R.E. Green, Basic wave analysis of acoustic emission. In: Stinchcomb W.W., Duke, J.C., Henneke E.G., Reifsnider K.L. (eds), *Mechanics of Nondestructive Testing*, Springer, Boston, MA. 1980.
- [71] M. Ohtsu, The history and development of acoustic emission in concrete engineering, *Magazine of Concrete Research*, vol. 48, pp. 321-330, 1995.
- [72] M. Mondal and G. B. Kumbhar, Detection, measurement, and classification of partial discharge in a power transformer: methods, trends and future research, *IETE Technical Review*, pp. 483-493, 2017.
- [73] Christian U. Grosse and Masayasu Ohtsu, *Acoustic emission testing*, 1st Edn., Springer Verlag Berlin Heidelberg, le-tex publishing services HG, Leipzig, Germany, 2008.
- [74] P. Mazal and J. Dvoracek, "Application of acoustic emission method in contact damage identification", *Int. J. Mat. and Pro. Tech.*, vol. 41, pp. 140-152, 2011.
- [75] H. A. Kishawy, H. Hegab, U. Umer, Application of acoustic emissions in machining processes: analysis and critical review, *Int. J. Adv. Manuf. Technol.*, vol. 98, pp. 1391-1407, 2018.
- [76] Hossein Heidary, Mehdi Ahmadi, Abdolreza Rahimi and Giangiacomo Minak Wavelet-based acoustic emission characterization of residual strength of drilled composite materials. *J. comp. mater.*, vol.47, pp. 2897-2908, 2012.
- [77] S. Bagavathiappan, B. B. Lahiri, T. Saravanan, John Philip, T. Jayakumar, Infrared thermography for condition monitoring-A review, *Infrared. Phys. Technol.*, vol. 60, pp. 35-55, 2013.
- [78] D. Kim, H. Yun, S. Yang, W. Kim, D. Hong, Fault diagnosis of ball bearing within rotational machines using the infrared thermography method, *J. of Kore. Soc. of Nondestr. Tes.*, vol. 30, pp. 570-575, 2010.

- [79] C.W. Reeves, Thermography Monitoring Handbook, Coxmoor Publishing Company, 1999.
- [80] X. Maldague. Theory and practice of infrared technology for nondestructive testing, John Wiley & Sons, INC, 2001.
- [81] <http://www.photonics.com/EDU/Handbook.aspx?AID=25132>.
- [82] X. Maldague. Nondestructive testing handbook, third edition: Infrared and thermal testing, ASNT, 2001.
- [83] J. Webster, W. P. Ding, R. Lindsay, Raw acoustic emission signal analysis of grinding process, CIRP. Ann. Manuf. Technol., vol. 45, pp. 335-340, 1996.
- [84] I.S. Kang, J.S. Kim, M.C. Kang and K.Y. Lee, Tool condition and machined surface monitoring for micro-lens array fabrication in mechanical machining, J. of Mat. Proc. Techn., vol. 201(1-3), pp. 585-589, 2008.
- [85] Zhirong Liao, Dragos A, Axinte on monitoring chip formation, penetration depth and cutting malfunctions in bone micro-drilling via acoustic emission, J. Mater. Process. Technol, vol. 229, pp. 82-93, 2016.
- [86] E. M. Rubio, R. Teti and I. L. Baciú, Advanced signal processing in acoustic emission monitoring systems for machining technology, Intell. Produ. Mach. and Sys., vol. 12, pp. 1-6, 2006.
- [87] W. Grzesik, and S. Brol, Wavelet and fractal approach to surface roughness characterization after finish turning of different workpiece materials, J. of Mat. Proc. Tech., vol. 209(5), pp. 2522-2531, 2009.
- [88] Erkki Jantunen, A summary of methods applied to tool condition monitoring in drilling. Int. J. Mach. Tools Manufact., vol. 42, pp. 997-1010, 2002.
- [89] Lisheng Zuo, Dunmen Zuo Yongcheng Zhu, and Hongfeng Wang, Acoustic emission analysis for tool wear state during friction stir joining of SiCp/Al composite, Int. J. Adv. Manuf. Technol, vol. 99, pp. 1361-1368, 2018.
- [90] Sunilkumar Kakade, L. Vijayaraghavan, and R. Krishnamurthy In-process tool wear and chip-form monitoring in face milling operation using acoustic emission. J. Mater. Process. Technol., vol. 44, pp. 207-214, 1994.
- [91] M. Prakash, M. Kanthababu, K. P. Rajurkar Investigation on the effects of tool wear on chip formation mechanism and chip morphology using acoustic emission signal in the microend milling of aluminum alloy, Int. J. Adv. Manuf. Technol., vol. 77, pp. 1499-1511, 2014.

- [92] Olufayo O, K. Abou-El-Hossein Tool life estimation based on acoustic emission monitoring in end-milling of H13 mould-steel, *Int. J. Adv. Manuf. Technol.* vol. 98, pp. 1391-1407, 2015.
- [93] C. K. Mukhopadhyay, T. Jayakumar, Baldev Raj, S. Venugopal, Statistical analysis of acoustic emission signals generated during turning of a metal matrix composite, *J. of Braz. Soc. of Mech. Sci. and Eng.*, vol. 34, pp. 145-154, 2012.
- [94] Navid Zarif Karimi, Giangiacomo Minak, Parnian Kianfar, Analysis of damage mechanisms in drilling of composite materials by acoustic emission, *Comp. Struc.*, vol. 131, pp. 107-114, 2015.
- [95] M. Karakus, S. Perez, Acoustic emission analysis for rock-bit interactions in impregnated diamond core drilling, *Inter. J. of Rock. Mech and Min. Sci.*, vol. 68, pp. 36-43, 2014.
- [96] S. R. Ravishankar and C. R. L. Murthy, Characteristics of AE signals obtained during drilling composite laminates, *NDT&E International*, vol. 33, pp. 341-348, 2000.
- [97] I. M. De Rose, C. Sasntulli, F. Sarasini, M. Valente, Effect of loading-unloading cycles on impact damaged jute/glass hybrid laminates, *poly. compos.*, vol. 30, pp. 1879-1887, 2009.
- [98] M. Ramulu, P. N. Rao, H. Kao, Drilling of (Al₂O₃) p/6061 metal matrix composites, *J. Mater. Process. Technol.*, vol. 124, pp. 244-254, 2002.
- [99] S. Hemant, Patne, Ankit Kumar, Shyamprasad Karagadde, S. Suhas, Joshi, Modeling of temperature distribution in drilling of titanium, *Int. J. Mech. Sci.*, vol. 133, pp. 598-610, 2017.
- [100] A. A. O. Tay, A review of methods of calculating machining temperature, *J. of Mat. Proc. Tech.*, vol. 36 (3), pp. 225-257, 1993.
- [101] S. Mekid, spatial thermal mapping using thermal infrared camera and wireless sensors for error compensation via open architecture controllers, *Proc. Inst. Mech. Eng. I.*, vol. 224 (7), pp. 789-798, 2010.
- [102] Balla Srinivasa Prasad, K, Aruna Prabha, P. V. S. Ganesh Kumar, Condition monitoring of turning process using infrared thermography technique- an experimental approach. *Infra. Phys. Techno*, vol. 81, pp. 137-147, 2017.
- [103] M. Saez-de-Buruaga, D. Spler, P. X. Aristimuno, J. A. Esnaola, P. J. Arrazola, Determining tool/chip temperatures from thermography measurements in metal cutting, *Appl. Therm. Eng.*, vol. 145, pp. 305-314, 2018.

- [104] L. Sorrentino, S. Turchetta, C. Bellini, In-process monitoring of cutting temperature during the drilling of FRP laminate, *Compos. Struct.*, vol.168, pp. 549-561, 2017.
- [105] Khaled Giasin, Sabino Ayvar-Soberanis, Evaluation of workpiece temperature during drilling of glare fiber metal laminates using infrared techniques: effect of cutting parameters, fiber orientation and spray mist application, *J. of. Mat.*, vol. 9, pp. 622 2016.
- [106] Lincoln Cardoso Brandao, Reginaldo Teixeira Coelho, Carlos Henrique Lauro, Contribution to dynamic characteristics of the cutting temperature in the drilling process considering one dimension heat flow, *Appl. Therm. Eng.*, vol. 31 (17-18), pp. 3806-3813, 2011.
- [107] G. Venkatesh, D. Chakradhar, Influence of thermally assisted machining parameters on the machinability of Inconel 718 superalloy, *Silicon*. Vol. 9(6), pp. 867-877, 2017.
- [108] Ramazan Çakıroğlu and Adem Acir, Optimization of cutting parameters on drill bit temperature in drilling by Taguchi method, *Measurement*, vol. 46 (9), pp. 3525-3531, 2013.
- [109] Eyup Bagci, Babur Ozcelik, Analysis of temperature changes on the twist drill under different drilling conditions based on Taguchi method during dry drilling of Al7075-T651, *Int. J. Adv. Manuf. Technol.* vol. 29, pp.629-636, 2006.
- [110] A. Taskensen, K. Kutukde, Analysis and optimization of drilling parameters for tool wear and hole dimensional accuracy in B₄C reinforced Al-alloy, *Trans. Nonferrous. Met. Soc. China.*, vol. 23, pp. 2524-2536, 2013.
- [111] Takeshi Yashiro, Takayuki Ogawa, Hiroyuki Sasahara, Temperature measurement of the cutting tool and machined surface layer in the milling of CFRP, *Int. J. Mach. Tool. Manufact.*, vol. 70, pp. 63-69, 2013.
- [112] Ranga Komanduri, and Zhen Bing Hou, Thermal modeling of the metal cutting process - Part III: temperature rise distribution due to the combined effects of shear plane heat source and the tool-chip interface frictional heat source, *Int. J. of Mech. Sci.*, vol.43 (1), pp. 89-107, 2001.
- [113] P. J. Arrazola, I. Arriola, M. A. Davies, A. L. Cooke, B. S. Duttererc, The effect of machinability on thermal fields in orthogonal cutting of AISI 4140 steel, *CIRP. Annals*, vol. 57, pp. 65-68, 2008.
- [114] Narendra Panwar, Amit Chauhan, Fabrication methods of particulate reinforced Aluminium metal matrix composite-A review, *Mat. Today: Proce.*, vol. 5 (2), pp. 5933-5939, 2018.

- [115] A. O. Inegbenebor, C. A. Bolu, P. O. Babalola, A. I. Inegbenebor, O. S. I, Fayomi, Aluminum Silicon Carbide Particulate Metal Matrix Composite Development Via Stir Casting Processing. *Silicon*, vol.10 (2), pp. 343-347, 2016.
- [116] N.N. Hsu and F.R. Breckenridge, "Characterization and calibration of acoustic emission sensors", *Materials Evaluation*, vol. 39, pp. 60-68, 1981.
- [117] Alexandre L. quadro and J. R.T. Branco, Analysis of the acoustic emission during drilling test, *Surf. & Coat. technol*, vol.94, 691-695, 1997.
- [118] Y. Dong and F. Ansari, Non-destructive testing and evaluation (NDT/NDE) of civil structures rehabilitated using fiber reinforced polymer (FRP) composites, *Service Life Estimation and Extension of Civil Engineering Structures*, vol. 7, pp.193-222, 2011.
- [119] R. Shivi Introduction to applied statistical signal analysis 3rd ed., san Diego Academic Press, 2007.
- [120] Benkedjouh, T., Zerhouni, N. & Rechak, S. Tool wear condition monitoring based on continuous wavelet transform and blind source separation. *Int J Adv Manuf Technol*, vol.97, pp. 3311-3323, 2018.
- [121] A. Marec, J. H. Thomas, El Guerjouma, Damage characterization of polymer –based composite materials: multivariable analysis and wavelet transform for clustering acoustic emission data, *Mech. Syst. Signal. Process.*, vol. 22, pp.1441-1464, 2008.
- [122] K. P. Soman, K. I. Ramachandran, Insight into wavelets from theory to practice, 2nd edition, Prentice-Hall of India Pvt. Limited, 2005.
- [123] J. Paulo Davim and Francisco Mata, Optimisation of surface roughness on turning fibre-reinforced plastics (FRPs) with diamond cutting tools, *Int. J. Adv. Manuf. Technol*, vol. 26, pp.319–323, 2005.
- [124] D. P. Sain J and Y. J. Park, A quantitative model of acoustic emissions in orthogonal cutting operations. *J. Mat. Proces & Technol*, vol. 58, pp. 343-350, 1996.
- [125] Claudiu Bisu, Mehdi Cherif , and Jean-Yves Knevez, Dynamic analysis of the forced vibration drilling process, *Procedia CIRP*, vol. 67, pp. 290-295, 2018.
- [126] T.I. El wardany, D. Gao, and A. Elbestawi, Tool condition monitoring in drilling using vibration signature analysis, vol. 30 (6), pp. 687-711, 1996.
- [127] Bing Wang and Zhanqiang Liu, Acoustic emission signal analysis during chip formation process high machining of 7050-T7451 aluminum alloy and Inconel 718 super alloy, *J. of Manuf. Process*, Vol. 27, 114-125, 2017.

- [128] M. S. H. Bhuiyan, I. A. Choudhury, M. Dahari, Y. Nukman, A. Z. Dawal, Application of acoustic emission sensor to investigate the frequency of tool wear and plastic deformation in tool conditioning monitoring, *Measurement*, vol. 92, pp. 208-217, 2016.
- [129] Mridusmita Roy Choudhury, Maddula Shanmuka Srinivas, Kishore Debnathe, Experimental investigation on drilling lignocellulosic fiber reinforced composite laminates, *J. Manuf. Pros.*, vol. 34, pp. 51-61, 2018.
- [130] B. Ozcelik, E. Bagci, Experimental and numerical studies on the determination of twist drill temperature in dry drilling - A new approach, *Mat. & Des*, vol. 27(10), pp. 920-927, 2006.
- [131] L. Sorrentino, C. Bellini, Validation of a Methodology for Cure Process Optimization of Thick Composite Laminates, *Poly-Plast. Technol. and Eng.*, vol. 54, pp. 1803-1811, 2015.
- [132] Sener Karabulut, Ugur Gokmen, Henifi Cinici, Study on the mechanical and drilling properties of AA7039 composites reinforced with $Al_2O_3/B_4C/SiC$ particles, *Compo. Part. B. Eng.*, vol. 93, pp. 43-55, 2016.
- [133] Q. Yanming, Z. Zehua, Tool wear and its mechanism for cutting SiC particle-reinforced aluminium matrix composites, *J. Mat. Proces. Technol*, vol. 100, pp. 194-199, 2000.
- [134] E. Kilickap, O. Cakir, M. Aksoy, A. Inan Study of tool wear and surface roughness in machining of homogenized SiC -p reinforced aluminum metal matrix composite, *J. Mater. Proc. Technol*, vol. 164, pp. 862-867, 2005.
- [135] Redouane Zitoune, Vijayan Krishnaraj, Belkacem Sofiane Almagbouacif, Francis Collombet, Michal Sima, Alain Jolin, Influence of machining parameters and new nano-coated tool on drilling performance of CFRP/Aluminum sandwich. *Composites: Part B*, vol. 43, pp. 1480-1488, 2012.
- [136] Sarbjit Singh, Effect of modified drill point geometry on drilling quality characteristics of metal matrix composite (MMCs), *Int. J. Mech. Sci*, vol. 30 (6), pp. 2691-2698, 2016.